Measuring the Weak Charge of the Proton and the Hadronic Parity Violation of the $N \to \Delta$ Transition

John D. Leacock II

Dissertation submitted to the Faculty of the
Virginia Polytechnic Institute and State University
in partial fulfillment of the requirements for the degree of

Doctor of Philosophy
in
Physics

Mark L. Pitt, Chair
Patrick Huber
Giti A. Khodaparast
Jonathan M. Link

16 October 2012
Blacksburg, Virginia

Keywords: Qweak, parity violation, weak charge of the proton, Standard Model test

Measuring the Weak Charge of the Proton and the Hadronic Parity Violation of the $N \to \Delta$ Transition

John D. Leacock II

(ABSTRACT)

Qweak will determine the weak charge of the proton, Q_W^p, via an asymmetry measurement of parity-violating elastic electron-proton scattering at low four momentum transfer to a precision of 4%. Q_W^p has a firm Standard Model prediction and is related to the weak mixing angle, $\sin^2\theta_W$, a well-defined Standard Model parameter. Qweak will probe a subset of new physics to the TeV mass scale and test the Standard Model.

The details of how this measurement was performed and the analysis of the 25% elastic dataset will be presented in this thesis. Also, an analysis of an auxiliary measurement of the parity-violating asymmetry in the $N \to \Delta$ transition is presented. It is used as a systematic inelastic background correction in the elastic analysis and to extract information about the hadronic parity violation through the low energy constant, d_Δ.

The elastic asymmetry at $Q^2 = 0.0252 \pm 0.0007$ GeV^2 was measured to be $A_{ep} = -265 \pm 40 \pm 22 \pm 68$ ppb (stat., sys., and blinding). Extrapolated to $Q^2 = 0$, the value of the proton's weak charge was measured to be $Q_W^p = 0.077 \pm 0.019$ (stat. and sys.)± 0.026 (blinding). This is within 1 σ of the Standard Model prediction of $Q_W^p = 0.0705 \pm 0.0008$.

The $N \to \Delta$ inelastic asymmetry at $Q^2 = 0.02078 \pm 0.0005$ GeV^2 and $W = 1205$ MeV was measured to be $A_{inel} = -3.03 \pm 0.65 \pm 0.73 \pm 0.07$ ppm (stat., sys., and blinding). This result constrains the low energy constant to be $d_\Delta = 5.8 \pm 22 g_\pi$, and, if the result of the G0 experiment is included, $d_\Delta = 5.8 \pm 17 g_\pi$. This result rules out suggested large values of d_Δ motivated by radiative hyperon decays.

The elastic measurement is the first direct measurement of the weak charge of the proton while the inelastic measurement is only the second measurement of the neutral current excitation of the Δ resonance. It is currently the best constraint for the low energy constant, d_Δ.

This work was funded by the NSF, the DOE, and Virginia Tech.

Acknowledgments

I would like to thank my advisor, Mark Pitt. I will continue to try to emulate his approachability and sharp insight throughout my career. He has a great ability to refocus straying discussions and see the core of an issue. I admire Mark's adherence to a higher level of scientific integrity through honesty and hard work. Hopefully, some of these traits have rubbed off on me.

I would like to thank my family for always being there when I need them. Mom, for always believing in me. Dad, for knowing when I needed a sympathetic ear or a motivating talk. Daniel, for hanging out and helping me forget the stress of work. I enjoy those moments more than you'll know. Alyssa, for opening her heart and home.

I would like to give a big thank you to all the Qweakers, especially, Dave Mack, my unofficial advisor on all things. Roger, for, among other things, staying late into the night helping me solve the lumi noise issue. Shelley, for sound career advice and being there to pass shifts quickly and painlessly. Mark Dalton, for sound scientific advice and blowing off steam with frisbee, cards, soccer, or a night out.

I would like to thank the other 25 percenters. Katherine, for being a great officemate and friend. John Leckey, for lightening the load on the other students by taking tons of shifts.

I would like to thank Rakitha and Buddhini, for helping me through my bumbling attempts at coding in C++ and for having an answer to every beamline or analysis question I had. Paul King, for knowing everything about Qweak and patiently and usually comically explaining it to me. Juliette, for blazing a trail to graduation and making me realize it really will happen. Scott, for letting me spend time with his family, Dana, Luke, and Chloe. To the Hokies that have taken over my role on Qweak, Wade Duvall and Anna Lee, stay the course.

I would like to thank the faculty and staff at VT. Chris Thomas, for never being too busy to help. Betty Wilkins, for helping me figure out my frequent travels without losing her patience. Tina Lawrence, for always being ready with a friendly smile and conversation.

Finally, I would like to thank the VT physics shop crew, Scott, John, and Ron, for helping with the construction of the luminosity monitors.

Contents

Abstract **ii**

Acknowledgments **iii**

Contents **iv**

List of Figures **ix**

List of Tables **xvi**

1 Introduction **1**

1.1 Physics Motivation 4

2 Theory **6**

2.1 Introduction 6

2.1.1 Electroweak Interaction and Parity Violation 7

2.1.2 The Δ Resonance 8

2.1.3 Cross Sections and Form Factors 10

2.2 Elastic Parity-Violating Asymmetry 14

2.3 Inelastic Parity-Violating Asymmetry 19

2.3.1 Radiative Hyperon Decay 26

3 Qweak Experimental Apparatus **31**

3.1 Introduction 31

3.2 Beamline 35

3.2.1 Accelerator 35

3.2.2 Beam Monitoring 39

3.3 Main Detectors 41

3.4 Qweak Spectrometer 42

3.4.1 Collimators and Shield Wall 43

3.4.2 Toroidal Magnet 43

3.4.3 Tracking Detectors 45

3.5 Scanner 51

3.6 Polarimetry 53

3.6.1 Møller Polarimeter 53

3.6.2 Compton Polarimeter 54

3.7 Target System 56

3.7.1 LH_2 Target 57

3.7.2 Solid Targets 60

3.8 Data Acquisition 62

4 Luminosity Monitors **63**

4.1 Introduction 63

4.2 Design 64

4.3 Simulation 77

4.4 Testing 85

4.4.1 Event Mode 85

4.4.2 Integration Mode 88

4.5 Prototype Luminosity Monitor and Target Density Fluctuation Frequency Dependence Study 91

4.5.1 Introduction 91

4.5.2 Experimental Method 92

4.5.3 Results 100

4.5.4 Conclusion 103

4.6 Performance 104

5 Elastic Electron-Proton Analysis **112**

5.1 Q^2 113

5.1.1 Beam Energy 114

5.1.2 Scattered Beam Angle 115

5.1.3 Reconstructed Q^2 for the 25% Dataset 116

5.2 Polarization 117

5.2.1 Møller Polarimeter 117

5.3 Parity-Violating Asymmetry 118

5.3.1 Regression 121

5.3.2 Transverse Asymmetry 124

5.3.3 Aluminum Background 125

5.3.4 Inelastic Background 127

5.3.5 Beamline Background 130

5.4 Elastic Electron-Proton Asymmetry 132

5.4.1 Cut Dependence 135

5.5 Corrections 138

5.6 Uncertainties 139

6 Inelastic Electron-Proton Analysis 142

6.1 Initial Inelastic Dataset 143

6.2 Second Inelastic Dataset 146

6.2.1 (IN+OUT)/2≠0 Hunt 147

6.2.2 Helicity Correlated Pedestal Difference Study 157

6.3 Third Inelastic Dataset 162

6.3.1 Q^2 164

6.3.2 Polarization 165

6.3.3 Backgrounds 166

6.4 Inelastic Electron-Proton Asymmetry 171

6.4.1 Cut Dependence 172

6.5 Corrections 174

6.6 Uncertainties 175

7 Results **182**

7.1 Extraction of d_Δ 182

7.2 Extraction of Q_W^p 184

7.2.1 γZ Radiative Correction 187

7.3 Comments on Main Detector Weighting 188

A Notes from Pedestal Difference Analysis **190**

Bibliography **192**

List of Figures

1.1 Running of $\sin^2\theta_W$ 2

2.1 Proton cross section data versus invariant mass 10

2.2 Feynman diagrams of the relevant tree level physics of Qweak 12

2.3 World data on parity-violating electron scattering at low Q^2 and forward scattering angles 16

2.4 Isoscalar and isovector combinations of C_{1u} and C_{1d} 18

2.5 Feynman diagram of the inelastic reaction for Qweak 19

2.6 Dominant interactions producing the Δ 24

2.7 Feynman diagram for the Siegert interaction term 25

2.8 A_{inel} components $\Delta^{\pi}_{(1)}$, $\Delta^{\pi}_{(2)}$, and $\Delta^{\pi}_{(3)}$ for low Q^2 26

2.9 Radiative hyperon decay of a Σ^+ into a γ and a proton 27

2.10 Radiative hyperon decay of a Σ^+ into a γ and a proton with an intermediate $1/2^-$ state 27

3.1 Schematic sketch of the essentials of the Qweak apparatus 33

3.2 Schematic of the accelerator at Jefferson Lab 35

3.3 Injector gun at Jefferson Lab 37

3.4 SRF cavities at Jefferson Lab 38

3.5 Beam Position Monitor and Beam Charge Monitor 40

3.6 Main detectors as installed in Hall C 41

3.7 Qweak schematic and as installed apparatus 42

3.8 Qweak coordinate system 44

3.9 Gas Electron Multiplier schematic 46

3.10 Horizontal Drift Chambers 49

3.11 HDC line segment projection onto primary collimator 49

3.12 Simulated scanner rate map 52

3.13 Experimental scanner rate map 52

3.14 Møller polarimeter schematic 54

3.15 Compton polarimeter schematic 55

3.16 Qweak target schematic 57

3.17 Raster pattern on face of target 59

3.18 Target density contribution 60

3.19 Solid target assembly 61

4.1 Downstream luminosity monitor quartz CAD drawings 65

4.2 Downstream luminosity monitors installed at Jefferson Lab 65

4.3 Upstream luminosity monitor quartz CAD drawings 66

4.4 Upstream luminosity monitors installed at Jefferson Lab 67

4.5 Unity gain base wiring diagram for the R375 68

4.6 Signal chain for the luminosity monitors 69

4.7 Preamplifier design used with the downstream luminosity monitors and main detectors 70

4.8 ADCs used with the luminosity monitors, main detectors, and beam monitoring devices 71

4.9 Comparison of different MIRO material light guides 73

4.10 Light yield in simulation with and without beveled edge quartz 74

4.11 Quartz and UVT lucite light transmission as a function of wavelength 75

4.12 Quantum efficiency of the R375 PMT 76

4.13 Luminosity monitor rates versus scattering angle 77

4.14 Multiple scattering versus scattering angle 78

4.15 Weighted cross section and asymmetry versus scattering angle 79

4.16 Energy and angle sensitivity versus scattering angle 80

4.17 Position sensitivity versus scattering angle 80

4.18 Initial Geant4 simulation of a downstream luminosity monitor 83

4.19 Downstream luminosity monitor light yields on the test bench at VT 86

4.20 Downstream luminosity monitor light yields at Jefferson Lab 87

4.21 Setup schematic of linearity test 88

4.22 Differential nonlinearity of an R375 PMT 89

4.23 QTOR electron beam steering observed by the downstream luminosity monitors 90

4.24 Linephase correlation with LUMI 1 signal 94

4.25 Linephase correlation with LUMI 1 signal after linephase correction was applied 94

4.26 Linephase correlation with LUMI 6 signal 95

4.27 Fit of the asymmetry width on the carbon target 97

4.28 Asymmetry width on the carbon target 99

4.29 Asymmetry width on the LH_2 target 99

4.30 Extracted boiling widths as a function of beam current for the 30 Hz data-taking rate 100

4.31 Boiling width dependence on data-taking rate 101

4.32 Fractional increase of asymmetry width above counting with constant boiling term 102

4.33 Fractional increase of asymmetry width above counting with observed frequency to boiling relation 103

4.34 Effect of turbo pump vibration on luminosity monitor signals 106

4.35 Raster modulation of BCM, MD, and downstream luminosity monitor signals 107

4.36 Downstream luminosity monitor 1 asymmetry width before regression 108

4.37 Downstream luminosity monitor 1 asymmetry width after regression 109

4.38 Intrinsic BPM resolution calculated from residuals 109

4.39 Upstream luminosity monitor asymmetry widths (in ppm) 110

4.40 *pmtltg* background detector asymmetry widths (in ppm) 110

5.1 Scattering angle of electrons 115

5.2 Reconstructed Q^2 for the 25% dataset 116

5.3 Polarimetry data for the 25% dataset 117

5.4 Main detector sensitivity cancellation for the Qweak experiment 120

5.5 Preliminary results of transverse asymmetry measurement 124

5.6 Aluminum dilution measurements at different hydrogen gas pressures 126

5.7 Aluminum asymmetry 127

5.8 Inelastic dilution 128

5.9 Inelastic asymmetry 129

5.10 Beamline dilution for production running with QTOR at 8921 A 131

5.11 Beamline asymmetries for Run I 132

5.12 25% dataset measured asymmetry 133

5.13 Cut dependence of 25% dataset HWP IN 136

5.14 Cut dependence of 25% dataset HWP OUT 136

6.1 Initial inelastic dataset quality 145

6.2 Second inelastic dataset quality 147

6.3 Second inelastic dataset sensitivities before regression 148

6.4 Second inelastic dataset sensitivities after regression 149

6.5 Individual bar measured asymmetry agreement before regression 149

6.6 Individual bar measured asymmetry agreement after regression 150

6.7 Nonlinearities of the second dataset 151

6.8 Measured charge asymmetry pattern dependence in second dataset slug IN,R 152

6.9 Measured main detector asymmetry pattern dependence in second dataset slug IN,R 153

6.10 Measured battery asymmetry pattern dependence in second dataset slug IN,R 154

6.11 Measured battery asymmetry correlation with charge asymmetry 154

6.12 Background detectors for the first and second datasets 155

6.13 Background detector *pmtled* in second dataset slug IN,R 156

6.14 Statistical distribution of mean divided by sigma of all channels 160

6.15 BCM pedestal differences in μV from pedestal runs in April 2011 160

6.16 Main detector pedestal differences in μV from pedestal runs in April 2011 . . 161

6.17 Pedestal value distribution of the unweighted average of all main detector bars 161

6.18 Third inelastic dataset quality 163

6.19 Simulated Q^2 distribution for the inelastic measurement in GeV 164

6.20 Simulated missing mass, W, distribution at the inelastic QTOR setting in MeV 165

6.21 Polarization for the final inelastic measurement 166

6.22 Inelastic aluminum dilution 167

6.23 Inelastic aluminum asymmetry 168

6.24 Inelastic beamline dilution 169

6.25 Inelastic beamline asymmetry 169

6.26 Cut dependence of inelastic dataset HWP IN 173

6.27 Cut dependence of inelastic dataset HWP OUT 174

6.28 Simulation of contributions to signal versus QTOR 177

6.29 Comparison of data and simulation rate shapes versus QTOR 178

6.30 Comparison of data and simulation rate shapes versus QTOR log scale . . . 178

6.31 Residuals from a comparison of data and simulation rates versus QTOR . . . 179

7.1 Inelastic asymmetry for different d_Δ values as a function of Q^2 for this analysis and the G0 data point 183

7.2 World data on parity-violating electron scattering at low Q^2 and forward scattering angles including the 25% data point from this analysis 185

7.3 Constraints on the weak vector couplings C_{1u} and C_{1d} including 25% Qweak measurement 186

7.4 Theoretical prediction of γZ box contribution to Qweak 188

List of Tables

2.1 Electric and weak charges of fermions 8

2.2 Nucleons and Δ resonances and their associated properties 9

3.1 Qweak experimental parameters 34

4.1 Manufacturer's specifications for MIRO reflectivity 72

4.2 Estimated rate comparison of three locations for the downstream luminosity monitors 81

4.3 Devices used in June 2008 beam test 92

4.4 Targets used in June 2008 beam test 92

4.5 Width contribution of noise sources 97

4.6 Comparison of extracted and fit values 98

5.1 Contributions to the uncertainty of the Møller polarization in the 25% dataset 118

5.2 Regression schemes 122

5.3 Measured asymmetries using different regression schemes for 25% dataset in ppm 134

5.4 Good regression schemes and the mean for 25% dataset in ppm 135

5.5 Regression schemes with 5 σ cuts on each beam parameter mean for 25% dataset in ppm 137

5.6 Good regression schemes with 5 σ cuts on each beam parameter mean for 25% dataset in ppm 137

5.7 Contributions to the measured asymmetry 138

5.8 Contributions to the uncertainty of A_{ep} 140

6.1 The inelastic datasets 143

6.2 The initial inelastic dataset helicity correlated beam parameters 144

6.3 The second inelastic dataset helicity correlated beam parameters 146

6.4 The third inelastic dataset helicity correlated beam parameters 163

6.5 Measured polarization for the final inelastic dataset 166

6.6 Measured asymmetry at QTOR 6700 A 172

6.7 Contributions to the measured asymmetry. 175

6.8 Uncertainties of the extracted inelastic asymmetry. 176

Chapter 1

Introduction

This thesis will describe two measurements; elastic electron-proton scattering to determine the weak charge of the proton and inelastic electron-proton scattering to constrain the low energy constant, d_Δ. These measurements can be more simply described as electron-proton scattering at two different kinematics using the Qweak apparatus.

Both measurements form asymmetries, which are used to isolate the interference of the electromagnetic and weak interactions. Electromagnetic interactions conserve parity while weak interactions do not. By forming an asymmetry, the magnitude of the parity violation of the weak interaction can be determined.

Qweak is a low energy search for physics beyond the Standard Model. A precise measurement of the weak charge of the proton, Q_W^p, is made by measuring the parity-violating asymmetry in elastic electron-proton scattering of longitudinally polarized electrons at a four momentum (Q^2) transfer of 0.025 GeV^2.

The Qweak apparatus consisted of a $\sim$35 cm long liquid hydrogen target, a magnetic spectrometer, and fused silica detectors. The experiment was slated for 2200 hours of 180 μA

current at 85% longitudinal polarization at Thomas Jefferson National Accelerator Facility in Newport News, Virginia. This experiment was possible by building on the techniques developed for the Prescott experiment at SLAC [32, 33] and the high quality polarized electron beam available at Jefferson Lab.

The weak charge of the proton is a fundamental property that has never been directly measured. The Qweak collaboration plans to measure Q_W^p to a precision of 4%, which will be a 0.3% measurement of $\sin^2\theta_W$. This allows the "running of $\sin^2\theta_W$" to be tested to 10 σ. Figure 1.1 shows the running of the weak mixing angle.

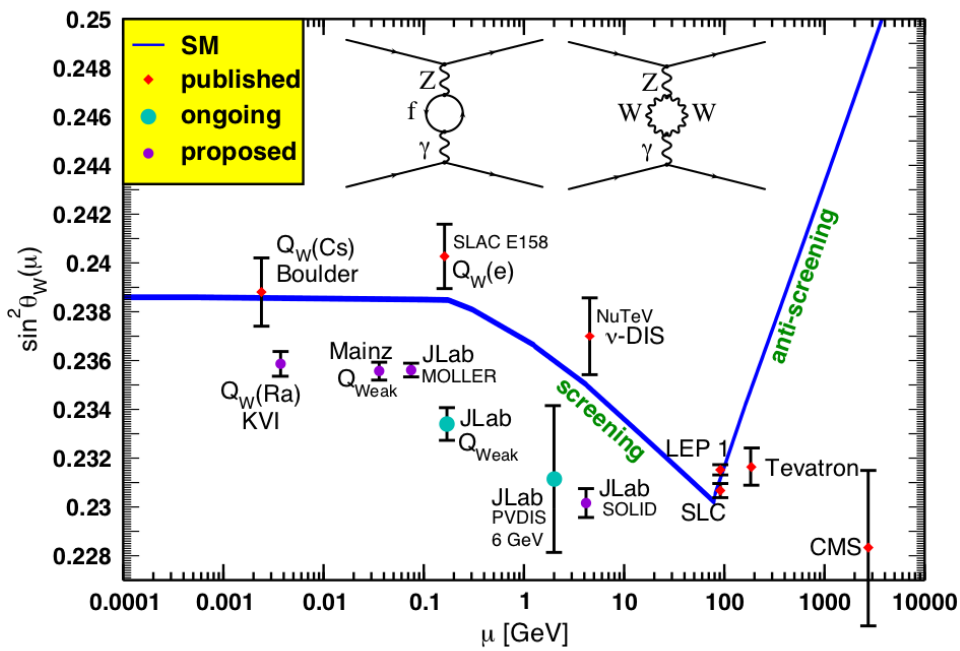

Figure 1.1: *Running of the weak mixing angle,* $\sin^2\theta_W$*, as a function of four momentum transfer. The blue line is the Standard Model prediction. The points from LEP 1, SLC, Tevatron, and CMS points are separated for clarity but are all at the mass of the Z and contribute to the precise determination of* $\sin^2\theta_W$ *at the Z pole.*

The weak charge of the proton is simply $Q_W^p = 1 - 4\sin^2\theta_W$ at tree level. The weak mixing

angle, $\sin^2\theta_W$, represents the mixing of the two neutral currents in the Standard Model. It arises from the unification of the electromagnetic and weak interactions in the electroweak model.

The matrix,

$$\begin{pmatrix} |\gamma\rangle \\ |Z^0\rangle \end{pmatrix} = \begin{pmatrix} \cos\theta_W & \sin\theta_W \\ -\sin\theta_W & \cos\theta_W \end{pmatrix} \begin{pmatrix} |B^0\rangle \\ |W^0\rangle \end{pmatrix}$$

shows how the neutral bosons observed experimentally, γ and Z^0, are a mixture of the W^0 and the B^0.

Beam time allotted for Qweak was also used for an inelastic scattering experiment. This measurement is of the asymmetry arising from the excitation of the proton to a Δ, its first excited state. The goal was to measure the inelastic asymmetry to 25%. This precision would sufficiently constrain the inelastic background for the Qweak experiment and better constrain the low energy constant, d_Δ, which arises from the parity-violating hadronic weak interaction.

The inelastic asymmetry is dominated by the axial transition form factor at tree level but recent theoretical predictions [51] allow a radiative correction characterized by the low energy constant, d_Δ, to dominate at very low four momentum transfer. The axial transition form factor, $G^A_{N\Delta}$, is related to how the spin of the valence quarks of the proton are redistributed during excitation. The d_Δ parameter is driven by the hadronic weak interaction, which represents the weak interaction among quarks.

A similar measurement of the inelastic asymmetry took place during the G0 experiment at Jefferson Lab [9]. G0 used parity-violating electron scattering to probe the strange quark contribution to the electromagnetic form factors. Ancillary measurements took place during data-taking including pion photoproduction on the Δ resonance. G0 was able to put the

first constraints on the low energy constant, d_Δ, which characterizes an interesting radiative correction of the N$\rightarrow$ Δ asymmetry [5].

1.1 Physics Motivation

The Standard Model of the electroweak interaction has been tested from a few eV in atomic parity violation (APV) to several hundred GeV at LEP.

The Standard Model prediction of the weak charge of the proton ($Q_W^p = 1 - 4\sin^2\theta_W$) is fortuitously suppressed because the value of $\sin^2\theta_W$ is numerically close to 1/4. Because of this suppression, new physics effects will be fractionally larger and require less stringent experimental precision to observe. For example, to probe the same energy scales as APV Qweak can be an order of magnitude less precise. This is primarily due to the lack of suppression of the weak charge in neutrons. Atomic parity violation measurements require elements with neutrons and are limited by atomic structure calculations.

The dominant many-body effects that enter the measurement of the asymmetry of hydrogen at low Q^2 are nucleon form factors. Jefferson Lab and Mainz have completed a program of elastic parity violation measurements that have measured the form factors relevant to Qweak. These form factors have been measured with enough precision to be an acceptable source of uncertainty.

$Q_W(N, Z)$ measurements, such as APV, are sensitive to a nearly isoscalar combination of possible new semi-leptonic interactions involving up quarks and down quarks. Q_W^p is twice as sensitive to new up quark interactions as it is to down quark physics.

The Qweak measurement is complementary to the SLAC E158 experiment. E158 is an electron-electron scattering parity violation experiment with a similar Q^2 as Qweak. E158

probes the purely leptonic sector of new physics while Qweak probes the semi-leptonic sector.

Some new physics scenarios, such as B-L violating super symmetry, favor the semi-leptonic interactions while others are present in both semi-leptonic and pure leptonic experiments.

Some of the new physics possibilities probed by the Qweak experiment include heavy neutral gauge boson (e.g. Z'), B-L violating SUSY, and leptoquarks [12]. If observed, leptoquarks will be fractionally charged mediating particles that change an electron to an up quark, for example. The combination of the APV, the purely leptonic, and the semi-leptonic measurements will help disentangle the possible new physics contributions.

The inelastic asymmetry measurement is sensitive to the axial transition form factor of the proton during excitation to the Δ, $G^A_{N\Delta}$, at tree level. This reaction is induced by a parity-violating Z boson exchange that aligns the spins of the valence quarks in the proton.

A radiative correction involved in the inelastic asymmetry, called the Siegert term, which is characterized by d_Δ, has the interesting property that does not require it to be zero at Q^2=0. A natural scale for the d_Δ parameter is $g_\pi=3\cdot10^{-8}$, which is the hadronic parity-violating coupling constant for charged current interactions. Given a nonzero contribution at Q^2=0, this term could dominate the measured inelastic asymmetry at low Q^2.

The Siegert term arises from a γ coupling to a quark-quark weak interaction within the nucleon. The same dynamic that drives this interaction also drives the larger than expected symmetry breaking effects observed in weak radiative hyperon decay. A model that accounts for this large asymmetry breaking also predicts values for d_Δ that are significantly larger than the natural scale [51].

Qweak has measured this asymmetry at Q^2=0.021 GeV^2 and the results of this study will be presented in this thesis.

Chapter 2

Theory

2.1 Introduction

Electron scattering has been successfully used to measure properties of particles and nuclei. It is used as a probe of more complex particles because the electron has no internal structure and the electron's interactions with matter are well-understood.

The measurements reported in this thesis take advantage of years of previous work in electron scattering and parity violation measurements. The Prescott experiment at SLAC in 1978 [32, 33], the scattering of polarized electrons off of protons, developed many techniques that make a precise measurement like Qweak possible.

Qweak is the measurement of 1.16 GeV longitudinally polarized electrons elastically scattered off of protons in a liquid hydrogen target at a laboratory scattering angle of 8°. The four momentum transfer is relatively small ($Q^2 = 0.025$ GeV^2) to reduce the hadronic corrections needed to extract the final value for this measurement.

2.1.1 Electroweak Interaction and Parity Violation

The electromagnetic and weak interactions are a manifestation of the electroweak interaction. The unified electroweak interaction undergoes spontaneous symmetry breaking at about the mass of the mediating particles for the weak interaction. The weak interaction is mediated by the Z boson ($M_Z = 91.2$ GeV) in the neutral current and the $W^{\pm}$ ($M_W = 80.4$ GeV) in the charged current reaction. The two mediating particles are related through the weak mixing angle, θ_W, where $M_W^2 = M_Z^2 \cos^2 \theta_W$ [46].

The weak interaction is similar to a short range electromagnetic interaction except weak interactions violate parity. Parity is a transformation of spatial coordinates such that all coordinates are reversed. This is analogous to an image of a object as reflected by a mirror.

Parity was assumed to be conserved until Lee and Yang proposed it was violated in 1956 [22]. In 1957 the hypothesis was confirmed by Wu's measurement of the angular distribution of beta decay of ^{60}Co in a strong magnetic field at very low temperatures [47]. The magnetic field and low temperature was used to align the spins of the ^{60}Co. If parity was conserved in weak interactions, in this case beta decay, the angular distribution of beta particles from the decay of the ^{60}Co would not depend on the direction of the magnetic field. The observed distribution maximally broke parity symmetry. The detected beta particles had momentum antiparallel to the ^{60}Co spin direction.

In the case of electron-proton scattering the interaction is either electromagnetic or weak in nature and is mediated by a photon or a Z boson, respectively. Interactions can be described by the vertices created by the mediating particle. These vertices are in turn described by operators. A vector (V) operator changes sign under spatial inversion and an axial-vector (A) operator does not. To describe parity violation, a (V-A) combination of vector and axial-vector operators is needed.

Fermion		Q	c_V	c_A
leptons	ν_e, ν_μ, ν_τ	0	1	-1
	e, μ, τ	-1	$-1+4\sin^2\theta_W$	1
quarks	u, c, t	$\frac{2}{3}$	$1-\frac{8}{3}\sin^2\theta_W$	1
	d, s, b	$-\frac{1}{3}$	$-1+\frac{4}{3}\sin^2\theta_W$	1

Table 2.1: Electric and weak charges of fermions. c_V and c_A are the vector and axial-vector couplings for the weak interaction.

Table 2.1 shows each fermion's electric, weak vector, and axial-vector charges. Q_W^p can be calculated by adding the vector couplings of its quark components. At tree level, the value of the weak charge of the proton is $1-4\sin^2\theta_W$.

When the spin of an electron is antiparallel (parallel) to the momentum of the electron it is called left-handed (right-handed). The weak interaction prefers left-handed particles. Because the asymmetry is due to the interference between the electromagnetic and weak interactions the detected scattered electron asymmetry is small enough, on the order of 10^{-6}, that precise measurements are difficult.

2.1.2 The Δ Resonance

The Δ is the first resonance of the nucleon in which the total spin of the nucleon is J=3/2 and the mass is 1232 MeV. The proton's total spin, J=1/2, is calculated by the sum of the spins of its constituent quarks. Two of the valence quarks have parallel spins and the third is antiparallel. Because quarks are fermions with spin 1/2, the total spin of a proton is then 1/2. The Δ is any combination of three up and/or down quarks with spins that are all parallel. A list of allowed Δ states and their properties is given in Table 2.2.

Particle	Charge	Quarks	Spin	Isopin	I_3
proton	+1	uud	$\uparrow\uparrow\downarrow$	$\frac{1}{2}$	$+\frac{1}{2}$
neutron	0	udd	$\uparrow\downarrow\downarrow$	$\frac{1}{2}$	$-\frac{1}{2}$
Δ^{++}	+2	uuu	$\uparrow\uparrow\uparrow$	$\frac{3}{2}$	$+\frac{3}{2}$
Δ^{+}	+1	uud	$\uparrow\uparrow\uparrow$	$\frac{3}{2}$	$+\frac{1}{2}$
Δ^{0}	0	udd	$\uparrow\uparrow\uparrow$	$\frac{3}{2}$	$-\frac{1}{2}$
Δ^{-}	-1	ddd	$\uparrow\uparrow\uparrow$	$\frac{3}{2}$	$-\frac{3}{2}$

Table 2.2: Nucleons and Δ resonances and their associated properties. Note the Δ^{++} and the Δ^{-} require the nucleon to undergo a spin flip and a quark flavor change given the initial state was a nucleon. The Δ^{+} and the Δ^{0} can be created from the proton and nucleon, respectively, with solely a quark spin flip.

A Δ can be created in a number of ways. A photon could interact with a nucleon and flip the spin of one of the quarks to make them all parallel. A Z boson can create a Δ in the same way. These reactions can only create a Δ^{+} or a Δ^{0} if the target particle is a proton or neutron, respectively. However, if a nucleon is struck by a charged current weakly interacting particle, such as a neutrino, a quark can change flavor (from up to down or down to up) and flip spin. This reaction can create the Δ^{++} and the Δ^{-}. For the purposes of this thesis and Qweak, only the Δ^{+} is considered. A plot showing the first few resonances of the proton is shown in Figure 2.1. The relatively broad peak at $\sim$1.2 GeV is the Δ resonance discussed in this thesis. The width is related to the lifetime of the resonance by Equation 2.1. The dominant decay mode for all Δ states is via the strong force into a nucleon and a pion.

$$\Gamma = \frac{\hbar}{\tau} \tag{2.1}$$

The width of the Δ resonance is 118 MeV. Using Equation 2.1 one finds the lifetime of the Δ to be $5.58{\cdot}10^{-24}$ s. Relatively short lifetimes are due to decays via the strong force. If a particle can only decay via the weak force the lifetime is longer, e.g. the muon has a lifetime of $2.2{\cdot}10^{-6}$ s and the free neutron has a lifetime of 880 s [6].

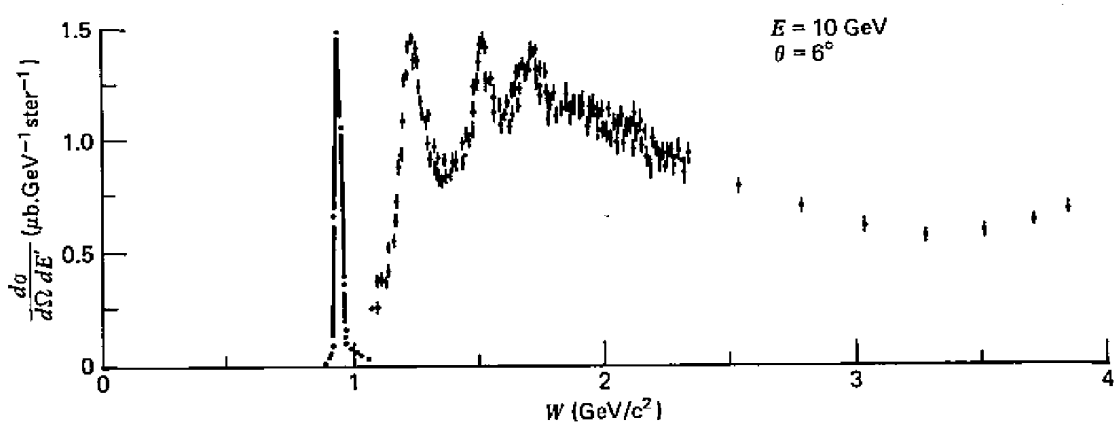

Figure 2.1: Cross section data with proton and delta resonances as a function of the invariant mass. This image is from Halzen Martin *Quarks and Leptons* [15].

An electron-proton interaction that induces a quark spin flip will reveal information about how the quark spin is redistributed during the transition. This information is contained in the axial transition form factor, $G^A_{N\Delta}$.

2.1.3 Cross Sections and Form Factors

The form of the cross section for unpolarized electrons elastically scattered off of a nucleon is given by,

$$\frac{d\sigma}{d\Omega} = \left(\frac{d\sigma}{d\Omega}\right)_{Mott} |F(Q^2)|^2 \ . \tag{2.2}$$

$F(Q^2)$ is the form factor term that contains information about the internal structure of the proton and,

$$\left(\frac{d\sigma}{d\Omega}\right)_{Mott} = \frac{\alpha^2\hbar^2c^2\cos^2\theta/2}{4E^2\sin^2\theta/2}\ , \tag{2.3}$$

where E is the beam energy and θ is the electron scattering angle, is the Mott cross section which describes electromagnetic scattering off of a point-like target ignoring target recoil. For single photon exchange (tree level electromagnetic) interactions the form factor term is,

$$|F(Q^2)|^2 = \frac{E'}{E}\left[\frac{G_E^2 + \tau G_M^2}{1+\tau} + 2\tau G_M^2 \tan^2\theta/2\right], \tag{2.4}$$

where $\tau = Q^2/4M_p^2$, $E'/E = 1/(1 + 2E/M_p \sin^2\theta/2)$, θ is the laboratory scattering angle of the electron, and Q^2 is the four momentum transfer of the interaction. However, this is a simplistic model that does not fully explain the scattering seen in the Qweak experiment. The next section will expand the cross section to include tree level neutral weak interactions then to include higher order interactions.

In nuclear physics tree level represents the simplest interactions available due to fundamental forces. For electromagnetism it is the exchange of a single photon and for weak interactions it is the exchange of a single Z or W. The framework for the cross section of an interaction is typically introduced using tree level physics with the higher-order terms added in later. This author will follow this approach in the following derivation.

At tree level the electron-proton interaction is due to an exchange of a photon or a Z boson in the electromagnetic or neutral weak interaction, respectively. The Feynman diagrams for each interaction are shown in Figure 2.2.

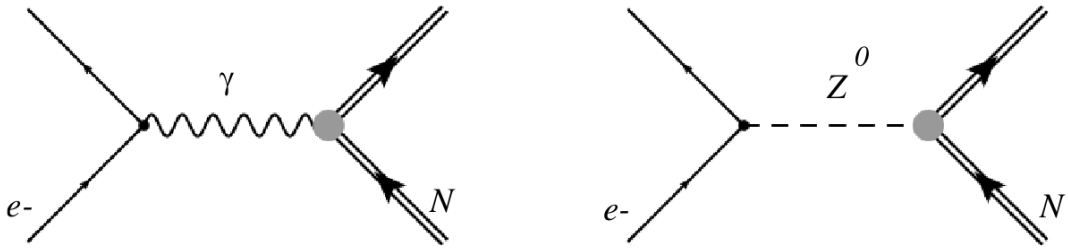

Figure 2.2: Feynman diagrams of the relevant tree level physics of Qweak. The γ is the force carrier for electromagnetism and Z^0 (shortened to Z in this thesis) is the force carrier for the neutral weak interaction. N is a generic label for a nucleon (proton or neutron).

At each vertex there is an associated current that depends on the type of interaction, interacting particle, and the mediating particle. For the electron these currents are given by,

$$J^{\mu}_{e,\gamma} = -e\bar{u}_e\gamma^{\mu}u_e \ , \tag{2.5}$$

$$J^{\mu}_{e,Z} = \bar{u}_e\gamma^{\mu}(g^e_V - g^e_A\gamma^5)u_e \ , \tag{2.6}$$

where $J^{\mu}_{e,\gamma}$ is the electromagnetic current, $J^{\mu}_{e,Z}$ is the neutral weak current, γ^{μ} and γ^5 are Dirac matrices representing vector and axial-vector interactions, respectively, and g^e_V and g^e_A are the vector and axial-vector couplings of the electron, respectively.

Notice the structure of the neutral weak current. The vector axial-vector combination (V-A) is necessary for parity violation to occur. The currents describing the proton form are not as simple. The internal structure of the proton must be taken into account by structure

functions.

$$\langle N|J^{\mu}_{p,\gamma}|N\rangle = \bar{\psi}_N \left[F_1^{\gamma}(Q^2)\gamma^{\mu} + F_2^{\gamma}(Q^2)\frac{i\sigma^{\mu\nu}q_{\nu}}{2M_N} \right] \psi_N \ , \tag{2.7}$$

$$\langle N|J^{\mu}_{p,Z}|N\rangle = \bar{\psi}_N \left[F_1^{Z}(Q^2)\gamma^{\mu} + F_2^{Z}(Q^2)\frac{i\sigma^{\mu\nu}q_{\nu}}{2M_N} + G_A^{Z}(Q^2)\gamma^{\mu}\gamma^5 \right] \psi_N \ , \tag{2.8}$$

where $J^{\mu}_{p,\gamma}$ and $J^{\mu}_{p,Z}$ are the electromagnetic and neutral weak currents for the proton, respectively, and the structure functions F_i, are typically written as a function of the Sach's form factors,

$$G_E(Q^2) = F_1(Q^2) - \tau F_2(Q^2) \ , \tag{2.9}$$

$$G_M(Q^2) = F_1(Q^2) + F_2(Q^2) \ . \tag{2.10}$$

The electromagnetic form factors for the proton arising from photon exchange, $G_E^{p,\gamma}$ and $G_M^{p,\gamma}$, have been well-studied using unpolarized electron scattering. The form factor $G_E^{p,\gamma}(Q^2)$ describes the distribution of the electric charge within the proton and Q^2 is the four momentum transferred from the incident particle to the target particle. A momentum transfer of near-zero would mean the incident particle interacted with the target particle as a whole and is therefore relatively insensitive to the internal structure of the target particle. The proton's electric form factor at a $Q^2 = 0$, $G_E^{p,\gamma}(0)$, is simply the electric charge of the proton. Similarly, $G_M^{p,\gamma}(0)$ is the proton's magnetic moment.

The neutral weak form factors have not been as extensively studied. $G_E^{p,Z}(Q^2)$ and $G_M^{p,Z}(Q^2)$ represent the weak neutral current electric and magnetic form factors for the proton. Using isospin symmetry and ignoring form factor contributions from quarks more massive than the

strange, one can write the proton's form factors as,

$$G_{E,M}^{p,\gamma} = \frac{2}{3}G_{E,M}^{u} - \frac{1}{3}(G_{E,M}^{d} + G_{E,M}^{s}) \ , \tag{2.11}$$

$$G_{E,M}^{p,Z} = \frac{2}{3}\left(1 - \frac{8}{3}\sin^2\theta_W\right)G_{E,M}^{u} + \frac{1}{3}\left(-1 + \frac{4}{3}\sin^2\theta_W\right)(G_{E,M}^{d} + G_{E,M}^{s}) \ , \tag{2.12}$$

$$G_A^Z = -G_A^u + G_A^d + G_A^s \ . \tag{2.13}$$

The u, d, and s superscripts denote the up, down, and strange quarks. The contribution of the axial form factor to the Qweak experiment is kinematically suppressed. The $Q^2 = 0$ limit of the neutral weak electric form factor is simply the weak charge of the proton, $G_E^{p,Z}(Q^2 = 0) = Q_W^p$. This is analogous to the $Q^2 = 0$ limit of the electric form factor of the proton being simply the electric charge of the proton.

A scientifically rich history of the study of the strange quark content of the quark sea has been carried out. It is outside the scope of this thesis but the contribution of the strange form factor, $G_{E,M}^s$, to the Qweak measurement has been shown to be small. More information can be found in the HAPPEX-III paper [4].

2.2 Elastic Parity-Violating Asymmetry

The tree level matrix elements for computing the cross section for Qweak are,

$$\sigma_{R,L} = |\mathcal{M}_{tot}|^2 = |\mathcal{M}_\gamma|^2 + |\mathcal{M}_Z|^2 = \mathcal{M}_\gamma^2 + \mathcal{M}_Z^2 + 2\Re(\mathcal{M}_\gamma^*\mathcal{M}_Z) \ , \tag{2.14}$$

where R (L) represents the right-handed (left-handed) helicity of the incident electron, $\mathcal{M}_Z$ is the matrix element for neutral current weak interactions, $\mathcal{M}_\gamma$ is the matrix element for electromagnetic interactions, and the interference term $2\Re(\mathcal{M}_\gamma^*\mathcal{M}_Z)$ carries the sign of the

helicity of the electron. The relevant quantity for studying parity violation, the parity-violating asymmetry is defined as,

$$A = \frac{\sigma_R - \sigma_L}{\sigma_R + \sigma_L} \ . \tag{2.15}$$

A right-handed electron's spin is parallel to its momentum while left-handed electron's spin is antiparallel to its momentum. Forming an asymmetry cancels the dominant $\mathcal{M}_\gamma^2$ and leaves a simple ratio of electromagnetic to weak matrix elements,

$$A \sim \frac{2\mathcal{M}_Z}{\mathcal{M}_\gamma} \ . \tag{2.16}$$

The interference between the two interactions magnifies the weak term and for our kinematics results in an asymmetry on the order of $\sim 10^{-6}$ assuming Standard Model couplings.

One can also write the asymmetry in terms of the form factors,

$$A = -\frac{G_F Q^2}{4\pi\alpha\sqrt{2}} \left[\frac{\epsilon G_E^\gamma G_E^Z + \tau G_M^\gamma G_M^Z - (1 - 4\sin^2\theta_W)\epsilon' G_M^\gamma G_A^e}{\epsilon (G_E^\gamma)^2 + \tau (G_M^\gamma)^2} \right] \ , \tag{2.17}$$

where,

$$\tau = \frac{Q^2}{4M_p^2} \ , \quad \epsilon = [1 + 2(1+\tau)\tan^2\theta/2]^{-1} \ , \quad \epsilon' = \sqrt{\tau(1+\tau)(1-\epsilon^2)} \ . \tag{2.18}$$

For Qweak, the asymmetry expression can be simplified because Q^2 is small and the scattering angle is very forward. This drives $\tau \sim 0$ and $\epsilon \sim 1$ and results in Equation 2.19,

$$A = -\frac{G_F Q^2}{4\pi\alpha\sqrt{2}} (Q_W^p + Q^2 B(Q^2)) \ , \tag{2.19}$$

where Q_W^p is the weak charge of the proton and the form factors are now contained in the $B(Q^2)$ term. The form factor term represents a significant portion, ∼30%, of the expected

asymmetry for Qweak. However, the correction is well-constrained by previous experiments as shown in Figure 2.3.

A summary of the world data on parity-violating electron scattering is presented in Figure 2.3. The asymmetry has been normalized to give the value of weak charge of the proton at $Q^2 = 0$. The dotted line represents the shift in Q_W^p if nucleon anapole form factors are included.

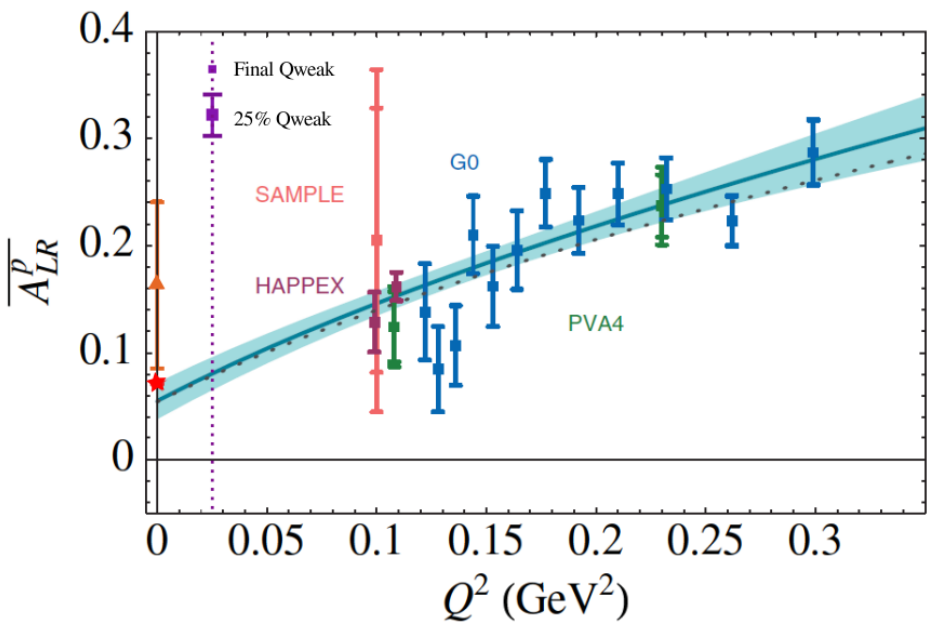

Figure 2.3: *World data on parity-violating electron scattering at low Q^2 and forward scattering angles. The light blue band is the fit value of Q_W^p with 1 σ confidence. The red star at $Q^2 = 0$ is the Standard Model value for the weak charge of the proton. The orange point, also at $Q^2 = 0$ is the PDG value of the weak charge of the proton and does not include parity-violating electron scattering. Both the nominal 25% measurement error bar and the final Qweak error are shown at an arbitrary y-axis value to highlight the impact of the Qweak measurement [50].*

Qweak is sensitive to new V-A couplings and the weak vector quark coupling combination, $2C_{1u} + C_{1d}$, where u and d represent the up and down quark composition of the proton. This is a model independent way to represent results from low energy experiments that are sensitive to the parity-violating electron-quark interaction.

The effective parity-violating low energy Lagrangian that governs electron-quark interactions is,

$$\mathcal{L}_{eq}^{PV} = -\frac{G_F}{\sqrt{2}} \sum_i [C_{1i}\bar{e}\gamma_\mu\gamma_5 e\bar{q}\gamma^\mu q + C_{2i}\bar{e}\gamma_\mu e\bar{q}\gamma^\mu\gamma^5 q] \ , \tag{2.20}$$

where i represents the quark flavors and C_{1i} and C_{2i} describe the weak vector and weak axial-vector quark couplings, respectively.

At tree level the values of the coupling constants are,

$$C_{1u} = -\frac{1}{2} + \frac{4}{3}\sin^2\theta_W \ , \tag{2.21}$$

$$C_{1d} = \frac{1}{2} - \frac{2}{3}\sin^2\theta_W \ , \tag{2.22}$$

$$C_{2u} = -\frac{1}{2} + 2\sin^2\theta_W \ , \tag{2.23}$$

$$C_{2d} = \frac{1}{2} - 2\sin^2\theta_W \ , \tag{2.24}$$

and the C_{2u} and C_{2d} are highly suppressed because $\sin^2\theta_W$ is numerically close to 1/4.

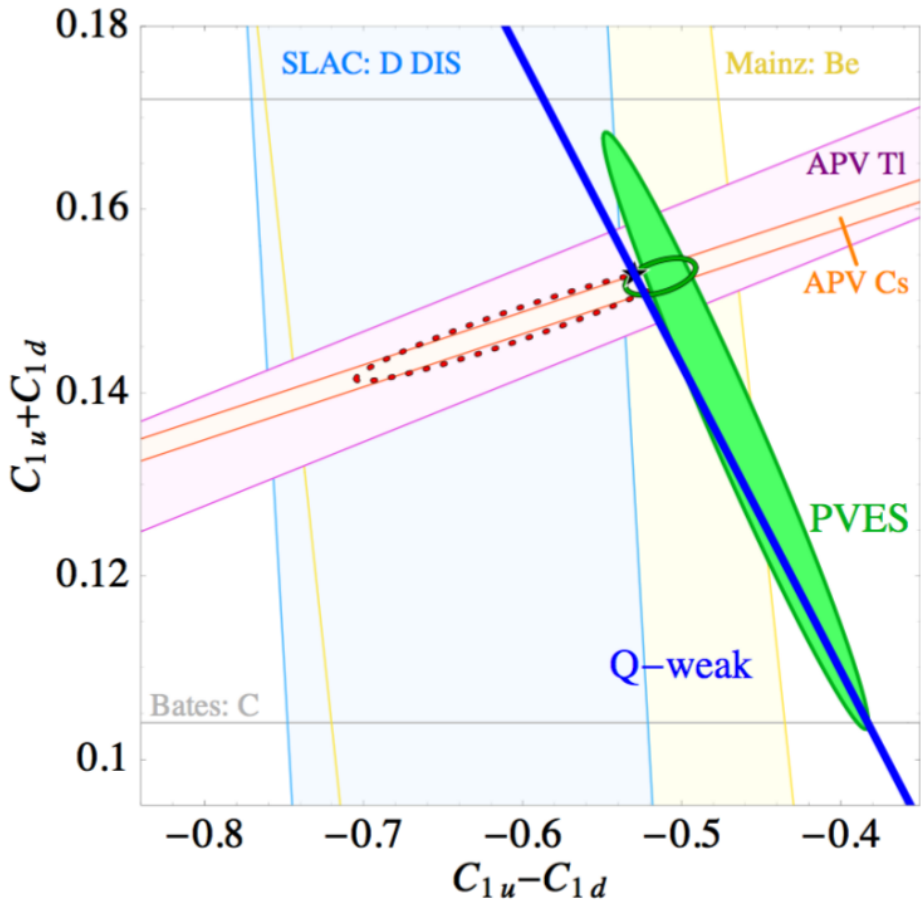

Figure 2.4: *Isoscalar and isovector combinations of C_{1u} and C_{1d}. The Y axis is isoscalar and the X axis is isovector. The isoscalar quantity is largely constrained by atomic parity violation on cesium and thallium, the green solid ellipse represents parity-violating electron scattering's contribution to constraining the isovector quantity, the blue line is the predicted constraint given the final uncertainty of Qweak, and the open green ellipse is the current best constraint from world data updated from [50].*

The world data on the isoscalar and isovector combinations of C_{1u} and C_{1d} are shown in Figure 2.4. One can clearly see the impact on the isovector coupling combination $C_{1u} - C_{1d}$ Qweak will have.

2.3 Inelastic Parity-Violating Asymmetry

In addition to measuring the elastic asymmetry for Qweak, dedicated time is allotted to measure the inelastic asymmetry. Inelastic events make it into the acceptance during normal production running and, because we integrate the detector signals, there is no way to separate the inelastic signal from the elastic signal. The inelastic asymmetry is expected to be a factor of 10 larger than the elastic asymmetry so knowing how many inelastic events are present is critical for correcting for the inelastic contribution.

The inelastic contribution in the Qweak acceptance is dominated by the production of the Δ resonance. The Feynman diagram for the inelastic interaction for Qweak is given in Figure 2.5. The incident electron (e) interacts with the proton (p) and loses energy (e'). The lost energy is transferred to the proton, which is excited to its first resonance (Δ^+) then decays to a neutral pion (π^0) and a proton (p).

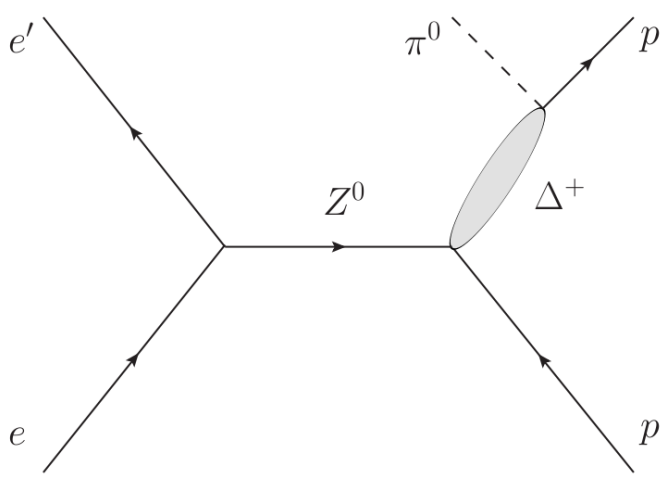

Figure 2.5: *Feynman diagram of the inelastic reaction for Qweak.*

The neutral weak current for the $\vec{e} + p \rightarrow e + \Delta^+$ interaction is,

$$J_\mu^Z = \frac{e}{2\sin\theta_W \cos\theta_W}[(1 - 2\sin^2\theta_W)V_\mu^3 + A_\mu^3] \ . \tag{2.25}$$

The factors preceeding the $V_\mu^3 + A_\mu^3$ are the Standard Model couplings for the vector and axial-vector. The transition is solely isovector because the change in isospin, ΔI, is 1. This is a consequence of the transition from the proton with $I = 1/2$ to the Δ with $I = 3/2$.

The neutral current form factors of this transition are not well-known. However, the conserved vector current hypothesis (CVC) states that the neutral current vector form factors can be obtained from the electromagnetic vector current form factors. The axial-vector neutral current form factors can be obtained from the axial-vector charged current form factors, which have been measured in the charged reactions mediated by the W, such as $\nu_\mu + p \rightarrow \mu^- + \Delta^{++}$.

The inelastic asymmetry has many contributions and grouping them leads to a simpler model as in [26],

$$A_{inel} = -\frac{G_F Q^2}{4\pi\alpha\sqrt{2}}[\Delta_{(1)}^\pi + \Delta_{(2)}^\pi + \Delta_{(3)}^\pi] \ , \tag{2.26}$$

where $\Delta_{(1)}^\pi$ contains the resonant terms, which are all isovector, $\Delta_{(2)}^\pi$ contains the nonresonant terms including both isovector and isoscalar, and $\Delta_{(3)}^\pi$ contains all axial-vector reactions at the hadron vertex. The nonresonant Standard Model term includes any reaction that creates a pion in the final state but does not create a Δ.

$\Delta_{(1)}^\pi$ is the resonant vector hadron term. It includes the axial-vector coupling of the electron to the Z and the isovector hadron coupling to the vector Z. $\Delta_{(1)}^\pi$ is independent of hadronic structure and is solely due to the Standard Model coupling. The Standard Model value is $\Delta_{(1)}^\pi = 2(1 - 2\sin^2\theta_W)$. The nonresonant vector term, $\Delta_{(2)}^\pi$, for the hadronic vertex includes isovector and isoscalar terms. Its contribution to the asymmetry is small at the Qweak

kinematics.

$\Delta^{\pi}_{(3)}$ contains the axial hadron term, which includes both the resonant and nonresonant terms. It will not be separated further because a more detailed understanding of its isospin structure is needed. A model for the inelastic asymmetry given in Equation 2.26 was formulated by the authors of [17]. They found that the $\Delta^{\pi}_{(3)}$ nonresonant and the nonresonant-resonant interference terms were of opposite sign. This makes the overall effect of the nonresonant terms negligible.

If we only consider the resonant terms the form of $\Delta^{\pi}_{(3)}$ is

$$\Delta^{\pi}_{(3)} \approx 2(1 - 4\sin^2\theta_W)F(Q^2) \ , \tag{2.27}$$

where $F(Q^2)$ contains the axial and electromagnetic form factors and can be written,

$$F(Q^2) = \frac{E + E'}{M} H^{\gamma}(Q^2) G^A_{N\Delta}(Q^2) \ , \tag{2.28}$$

where $H^{\gamma}(Q^2)$ is the electromagnetic form factor and $G^A_{N\Delta}(Q^2)$ is the axial transition form factor. More information on the derivation of the form factors is given in Carissa Capuano's thesis [9, pages 41-44]. The resulting axial transition form factor and thus a model for the inelastic asymmetry using fits done by Schreiner and von Hippel [38], Adler's dipole parameterization [1, 2], and Nath's coefficients [28], is given in Equation 2.29,

$$G^A_{N\Delta} = g_3 C^A_3 + g_4 C^A_4 + g_5 C^A_5 \ , \tag{2.29}$$

where,

$$g_3 = \frac{M}{2M'}[(M+M')(M-M') - 2(M-M')^2 - Q^2] \ , \tag{2.30}$$

$$g_4 = \frac{1}{2}[(M+M')(M-M') + Q^2] \ , \tag{2.31}$$

$$g_5 = -M^2 \ , \tag{2.32}$$

and,

$$C_3^A(0) = 0 \ , \tag{2.33}$$

$$C_4^A(0) = -0.35 \ , \tag{2.34}$$

$$C_5^A(0) = 1.20 \ . \tag{2.35}$$

So far, only the tree level interactions of the inelastic asymmetry have been discussed. If one includes the radiative corrections or higher-order terms things become more interesting. Putting constraints on one of these radiative corrections at low Q^2 is the focus of the inelastic asymmetry described in this thesis and this author is assuming all of the tree level formalism is correct.

The radiative effects can be divided into three categories. The first is purely electromagnetic caused by a single photon loop. The remaining terms are weak interactions involving either one or multiple quarks. The authors of [53, 51] found that including these radiative terms meant that the asymmetry would not necessarily be zero at $Q^2 = 0$. This effect is due to the mass difference between the initial and final state of the nucleon, which is mediated by a dipole coupling at the $\gamma N \Delta$ vertex. In effect, two quarks interact weakly within the nucleon and a γ couples to that interaction. Because the $A(Q^2 = 0) \neq 0$ requires a mass difference between the initial and final states it is absent in elastic scattering.

The authors of [53, 51] show that the following interactions dominate the final value of $\Delta^{\pi}_{(3)}$,

$$\Delta^{\pi}_{(3,total)} = \Delta^{\pi}_{(3,SM)} + \Delta^{\pi}_{(3,Siegert)} + \Delta^{\pi}_{(3,anapole)} + \Delta^{\pi}_{(3,d-wave)} \ , \tag{2.36}$$

where $\Delta^{\pi}_{(3,SM)}$ is the resonant Standard Model term, $\Delta^{\pi}_{(3,Siegert)}$ and $\Delta^{\pi}_{(3,anapole)}$ both arise from interactions coupling to the $\gamma N\Delta$ vertex and follow the electric multipole transition formulated by Siegert [40], and $\Delta^{\pi}_{(3,d-wave)}$ arises from the parity-violating d-wave $\pi N\Delta$ contribution.

The $\Delta^{\pi}_{(3,Siegert)}$ term is distinguished from the $\Delta^{\pi}_{(3,anapole)}$ term because it causes the $A(Q^2 = 0) \neq 0$ behavior by being Q^2 independent. Also, $\Delta^{\pi}_{(3,Siegert)}$ is only present in inelastic scattering because it is proportional to a product of a mass difference term $(E_f - E_i)$ and the electric dipole matrix element. At the kinematics of our inelastic asymmetry measurement we are particularly sensitive to the Siegert term, which does not necessarily vanish at $Q^2 = 0$, so we focus on it further.

The asymmetry due to the Siegert term is given by,

$$A(Q^2 = 0) \approx -\frac{2d_{\Delta}}{C_3^{\gamma}} \frac{M}{\Lambda_{\chi}} + ... \ , \tag{2.37}$$

where C_3^{γ} contains information about the electromagnetic form factor and was found to be 1.85 [28], M is the mass of the proton, and Λ_{χ} is the mass scale of chiral symmetry breaking or about 1 GeV. The effective weak Lagrangian determined from an effective field theory provides d_{Δ} as a new low energy constant characterizing the parity-violating $\gamma N\Delta$ coupling.

The axial part of the inelastic asymmetry can be rewritten in terms of Standard Model couplings and radiative corrections,

$$\Delta^{\pi}_{(3,total)} = 2(1 - 4\sin^2\theta_W)(1 + R_A^{\Delta})F(Q^2) \ , \tag{2.38}$$

where R_A^Δ contains the radiative factors, $\Delta^\pi_{(3,Siegert)}$, $\Delta^\pi_{(3,anapole)}$, and $\Delta^\pi_{(3,d-wave)}$, and is zero at tree level, and $F(Q^2)$ contains the axial transition form factor. Radiative corrections are generally assumed to be small so a measurement where they dominate is rare.

Figure 2.6 shows the dominant interactions that create a Δ. The first two diagrams are simply the tree level γ and Z induced Δ. The third diagram represents the Siegert and anapole terms and the fourth is the γZ box term.

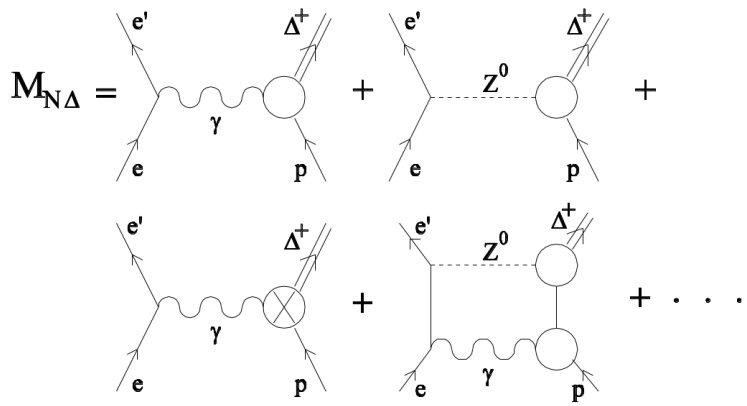

Figure 2.6: *Dominant interactions producing the* Δ.

$\Delta^\pi_{(3)}$ is proportional to the axial transition form factor and the dominant radiative corrections as given in Equation 2.39,

$$\Delta^\pi_{(3)} \propto (1 + R_A^\Delta) G^A_{N\Delta} \ , \tag{2.39}$$

where $R_A^\Delta = R_A^{ewk} + R_A^{Siegert} + R_A^{Anapole} + R_A^{Box} + ...$ [51]. The anapole term shares a Feynman diagram with the Siegert term but is zero at $Q^2 = 0$.

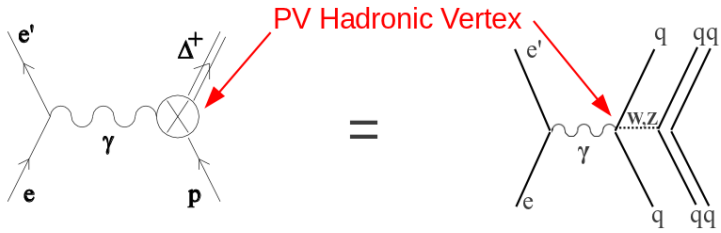

Figure 2.7: *Feynman diagram for the Siegert interaction term.*

Figure 2.7 shows the Feynman diagrams for the Siegert term. The parity-violating vertex is highlighted in the figure. The γ couples to a quark-quark weak interaction within the nucleon, which violates parity.

The theory predicts the contributions to the total asymmetry as shown in Figure 2.8. The range of d_Δ assumptions shown in this plot is motivated by the mode discussed in the next section. The Qweak inelastic measurement will be made at $Q^2 \sim 0.02$ GeV^2 so it is possible the d_Δ parameter can dominate the measurement.

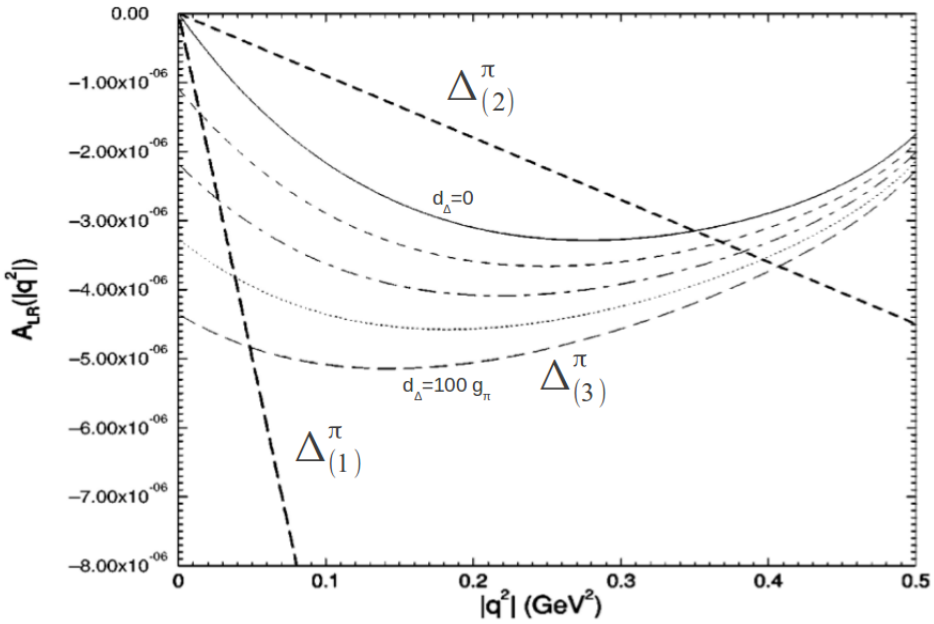

Figure 2.8: *A_{inel} components $\Delta^{\pi}_{(1)}$, $\Delta^{\pi}_{(2)}$, and $\Delta^{\pi}_{(3)}$ for low Q^2. This image has been adapted from [51].*

Of the components of A_{inel} the only free parameter is the Siegert term and large deviations from $d_{\Delta} = 0$ can be observed in this measurement. For the purposes of the analysis in this thesis, we are following the formalism given in [51] and we are assuming that the only free parameter is the low energy constant d_{Δ}, which parameterizes the Siegert term.

2.3.1 Radiative Hyperon Decay

There is a long standing issue with radiative hyperon decay that constraining the d_{Δ} may help resolve. In SU(3) symmetry the up, down, and strange quark masses are assumed to be equal and the expected magnitude for SU(3) symmetry breaking is related to the difference of the mass of the strange and up or down quarks and is approximately 15%. Equation 2.40

shows the approximation,

$$\frac{m_s - m_u}{\Lambda_\chi} \approx 15\% \ , \tag{2.40}$$

where m_s is the mass of the strange quark, m_u is the mass of the up or down quark, and Λ_χ is the mass scale for SU(3) symmetry and is $\sim$1 GeV.

However, in radiative hyperon decay, such as $\Sigma^+ \rightarrow \gamma p$ where $\Delta S = 1$, the measured asymmetry was a factor of five larger than the expected SU(3) symmetry breaking. This experiment was carried out by detecting the angular distribution of the decay products of a polarized Σ^+. Figure 2.9 shows this decay.

Figure 2.9: *Radiative hyperon decay of a Σ^+ into a γ and a proton. This reaction has a nonzero change of strangeness ($\Delta S = 1$).*

If one includes an intermediate $1/2^-$ state resonances which couple to the hyperon and the daughter nucleon the measured asymmetry agrees better with theory [8]. Figure 2.10 illustrate the addition to the decay diagram.

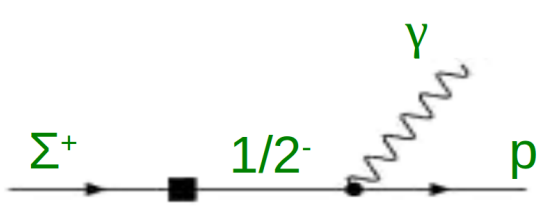

Figure 2.10: *Radiative hyperon decay of a Σ^+ into a γ and a proton with an intermediate $1/2^-$ state. This reaction has a nonzero change of strangeness ($\Delta S = 1$).*

We now describe how d_Δ is estimated with the aid of the above model. As discussed earlier, the low energy constant d_Δ comes from hadronic parity violation at the $\gamma N\Delta$ vertex (Figure 2.7). For many years, the standard treatment of hadronic parity violation used a meson exchange formalism with parity-violating couplings [10]. More recently, an effective field theory treatment has been adopted. This is the framework adopted by the authors of [51] where they introduce an effective chiral Lagrangian,

$$\mathcal{L}^{Siegert} = i\frac{ed_\Delta}{\Lambda_\chi}\bar{\Delta}^+_\mu\gamma_\lambda PF^{\mu\lambda} + H.c. \ , \tag{2.41}$$

to describe the Siegert term, where P is the proton field, $F_{\mu\nu}$ is the photonic field-strength tensor, d_Δ is the low energy constant, Λ_χ is the mass scale, and e is the electron charge. Here d_Δ is a low energy constant which can be used to parameterize this measurement and represents physics that corresponds to the non-perturbative regime of QCD. The amplitude corresponding to this is,

$$iM^{PV}_{Siegert} = -i\frac{(4\pi\alpha)d_\Delta}{Q^2\Lambda_\chi}\bar{e}\gamma_\mu e\bar{\Delta}_\nu[(M - M_\Delta)g^{\mu\nu} - q^\nu\gamma^\mu]N \ , \tag{2.42}$$

where, up to numerical factors,

$$\frac{d_\Delta}{\Lambda_\chi} \propto -\frac{\sqrt{2}}{3}\omega\langle f|\int d^3x x Y_{1\lambda}(\Omega)\hat{\rho}(x)|i\rangle \ , \tag{2.43}$$

which represents a parity-violating E1 (electric dipole) transition. This term is Q^2 independent and one can see explicitly that it vanishes in the elastic case since it is proportional to $\omega = E_f - E_i$, but it contributes to the parity-violating $N \to \Delta$ asymmetry.

To make the connection to the radiative hyperon decay, we introduce its amplitude as de-

termined by [8],

$$M(\Sigma^+ \to p\gamma) = \bar{u}_p(p')\frac{i}{2(M_{\Sigma^+} + M)}\sigma_{\mu\nu}F^{\mu\nu}(A_{p\Sigma^+} + \gamma_5 B_{p\Sigma^+})u_{\Sigma^+}(p) \ , \tag{2.44}$$

where $F^{\mu\nu}$ is the electromagnetic strength tensor, $A_{p\Sigma^+}$ is the parity conserving M1 amplitude, and $B_{p\Sigma^+}$ is the parity-violating E1 amplitude. This latter amplitude is proportional to d_Δ, just as it is in the amplitude for the Siegert contribution given in Equation 2.42. The asymmetry parameter in polarized $\Sigma^+ \to p\gamma$ decay is related to the decay amplitudes via,

$$\alpha_\gamma = \frac{2\Re\{A_{p\Sigma^+}B^*_{p\Sigma^+}\}}{|A_{p\Sigma^+}|^2 + |B_{p\Sigma^+}|^2} \ , \tag{2.45}$$

which, as noted above, is experimentally observed to be five times larger than simple SU(3) symmetry breaking expectations.

Given the success described above of including intermediate state resonances (referred to as "baryon resonance saturation") to predict values of $B_{p\Sigma^+}$ that enhance predicted hyperon radiative decay asymmetry, the authors of [51] applied the same model to estimates of d_Δ for the $\Delta S = 0$ channel relevant to the $N \to \Delta$ transition. Their prediction was limited by the fact that there is no experimental information on the relevant $\Delta S = 0$ amplitudes, so their estimate was based on $(1/2^- \to 1/2^+)$ $\Delta S = 1$ amplitudes. When they make this estimate and then assume the $\Delta S = 0$ amplitudes have the same strength, they get what they refer to as the "best" value of $d_\Delta = 25g_\pi$.

This is a large enhancement over the naive dimensional analysis estimate in [52] [25] of $d_\Delta \sim g_\pi$ (where $g_\pi = G_F F_\pi^2/2\sqrt{2}$), which is the scale of the charged current weak hadronic interaction. They further argue that an additional enhancement may be expected because the up and down quark charged current component of hadronic parity violation in the $\Delta S = 0$ regime is larger than the $\Delta S = 1$ regime by $V_{ud}/V_{us} \sim 4.5$. This leads them to quote

a reasonable range of 0-100g_π that accomodates the larger values implied by the possible $\Delta S = 0$ enhancement over $\Delta S = 1$.

Summarizing, the baryon resonance saturation model estimates of [51] lead to a predicted best value of $d_\Delta = 25 g_\pi$ with a reasonable range of 0-100g_π. The work reported in this thesis provides the most precise constraint on this parameter to date.

Chapter 3

Qweak Experimental Apparatus

3.1 Introduction

Experiment E08-016, "The Qweak Experiment: A Search for New Physics at the TeV Scale via a Measurement of the Proton's Weak Charge", took place in experimental Hall C of Jefferson Lab in Newport News, Virginia [34, 35, 36]. The experiment is split into two running periods, Run I and Run II, because of a scheduled six month 12 GeV upgrade in the middle of Qweak data-taking. First commissioning beam was delivered to Hall C in July 2010 and commissioning took place through the Fall of 2010. Run I took place between January and May of 2011 and Run II started November 2011 and ended in May of 2012.

The goal of Qweak is to measure the asymmetry between the number of detected electrons elastically scattered from protons at different helicity states at low momentum transfer. According to the Standard Model, this asymmetry is expected to be -230 parts per billion or $-2.3 \cdot 10^{-7}$ and the Qweak collaboration has a statistical goal for a measurement of this asymmetry of $\sim$2%, or $\sim$4 ppb.

To reach this uncertainty goal in a reasonable amount of time, the Qweak experiment predominantly integrated the electron signals instead of detecting individual electrons. Assuming only statistical contributions to the uncertainty, perfect running conditions, a combined rate of 5.8 GHz for integration mode, and a 100 kHz rate for event mode, it would take 125 days for integration mode to reach the uncertainty goal and 20 years to reach the same goal in event mode.

Event mode refers to the detection of individual electrons and was employed periodically throughout the experiment. This mode was required to measure the four momentum transfer among other uses. More information is given in Section 3.4.3.

As can be seen in Figure 3.1 the Qweak apparatus is simply polarized electrons scattered off a liquid hydrogen target and focused onto quartz detectors. Table 3.1 gives the experimental parameters for Qweak. Details about each subsystem will be presented in this chapter.

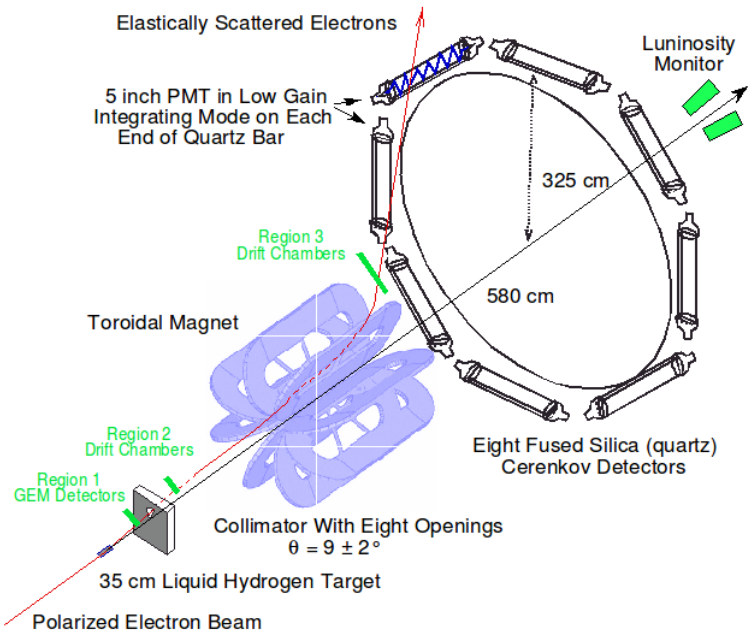

Figure 3.1: *Schematic sketch of the essentials of the Qweak apparatus. Polarized electrons enter from the lower left, scatter from the target, are collimated, pass through the bending magnet, and are detected by a ring of quartz bars.*

Table 3.1: Qweak experimental parameters

Parameter	Value
Incident beam energy	1.16 GeV
Beam current	180 μA
Beam polarization	89%
LH_2 target power	2.5 kW
Central scattering angle	$9 \pm 2^\circ$
Phi acceptance	50% of 2π
Average Q^2	0.025 GeV^2
Acceptance averaged asymmetry	-230 ppb
Integrated rate per detector	730 MHz
Total integrated rate	5.8 GHz

Because the measured asymmetry is such a small number, $\sim 10^{17}$ electrons must be detected to reach the statistical goal of Qweak. This requirement dictates that Qweak have a highly polarized, high current source of electrons, a high power, stable liquid hydrogen target, and a large detector acceptance for a high rate of detected electrons. These requirements promote statistical precision but systematic measurements and noise reduction are necessary to achieve the desired final precision. Each part of the apparatus plays a crucial role in the Qweak experiment.

3.2 Beamline

3.2.1 Accelerator

The Continuous Electron Beam Accelerator Facility (CEBAF) of Jefferson Lab delivers a continuous beam of polarized electrons to three experimental halls simultaneously [23]. Using superconducting radiofrequency (SRF), CEBAF is capable of accelerating electrons up to 6 GeV. A schematic of the accelerator is given in Figure 3.2.

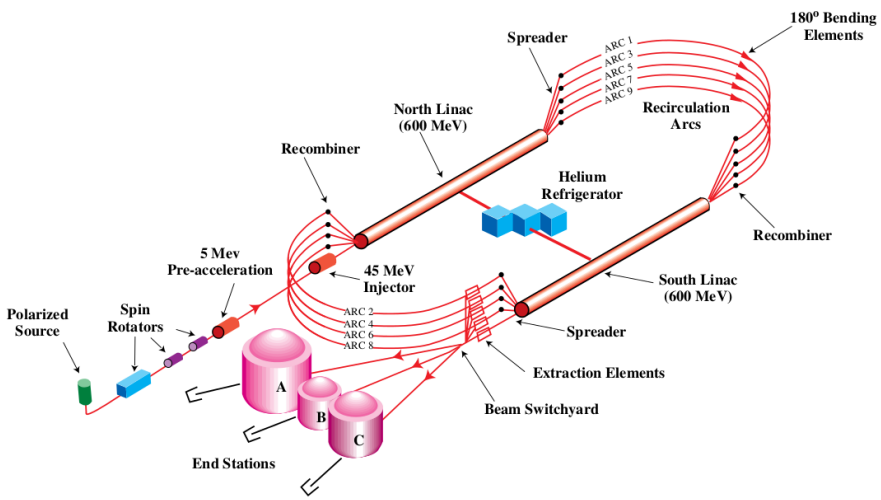

Figure 3.2: *Schematic of the accelerator at Jefferson Lab.*

The source of the electrons is a strained gallium arsenide (GaAs) photocathode capable of emitting 0.3 mA. Circularly polarized laser light strikes the photocathode and electrons are emitted via the photoelectric effect. The resulting longitudinal polarization is routinely greater than 85% [29, 31].

Each Hall has a dedicated laser that emits 1560 nm light into a frequency doubling nonlinear crystal. This light is passed through polarizers to insure total linear polarization. Each Hall's

laser is pulsed 120° out of phase for simultaneous beam delivery into the three experimental halls. The injector used during the Qweak experiment is shown in Figure 3.3.

The electron beam polarization is changed in a quartet pattern of either $+--+$ or $-++-$. The quartet is divided into macropulses (MPS) which last 1.04 milliseconds. A total quartet is 4.16 milliseconds. The fast polarization change is done by the Pockels cell and a slow polarization flip is done by the half-wave plate every 8 hours and by a double Wien filter every few weeks.

An insertable half-wave plate (HWP) can be introduced into the laser light while the light is still linearly polarized to reverse the polarization. This is used to monitor systematic effects in the creation of the beam that can alter the measured asymmetry in the experimental hall. The primary purpose of the HWP is to reverse the electron beam helicity without changing the electronic helicity signal. This isolates false asymmetry effects that change sign with the electronic helicity signal but do not change with the true electron beam helicity.

A Pockels cell converts the linearly polarized laser light into circularly polarized light via electro-optically induced birefringence. The magnitude of the conversion is proportional to the applied electric field of the cell and by reversing the sign of the voltage applied (± 4 kV) right- and left-handed circularly polarized light is produced.

The double Wien filter used during the Qweak experiment can rotate the polarization of electrons to fine tune, and/or completely flip, the longitudinal polarization of the electron beam delivered to the experimental hall. This is done without changing the position or direction of the electrons as they pass through the filter [14].

A single Wien system is limited to fine adjustments of the polarization. In a double Wien system the first Wien rotates the polarization by 90° and the second Wien can rotate it another 90°. This provides another slow helicity flip, which is used to cancel systematic false

asymmetries.

This filter can also be used to produce transversely polarized electrons. These electrons are polarized perpendicular to the direction of their momentum. The collaboration used transversely polarized electrons to check the symmetry of the main detector bars. More detail is given in Section 5.3.2.

The quantum efficiency (QE) of the photocathode is measured daily and the laser spot is moved to a different place on the photocathode when the QE is measured to be less than 0.3%. The QE of the photocathode is adversely affected by ions within the gun striking the sensitive photocathode surface.

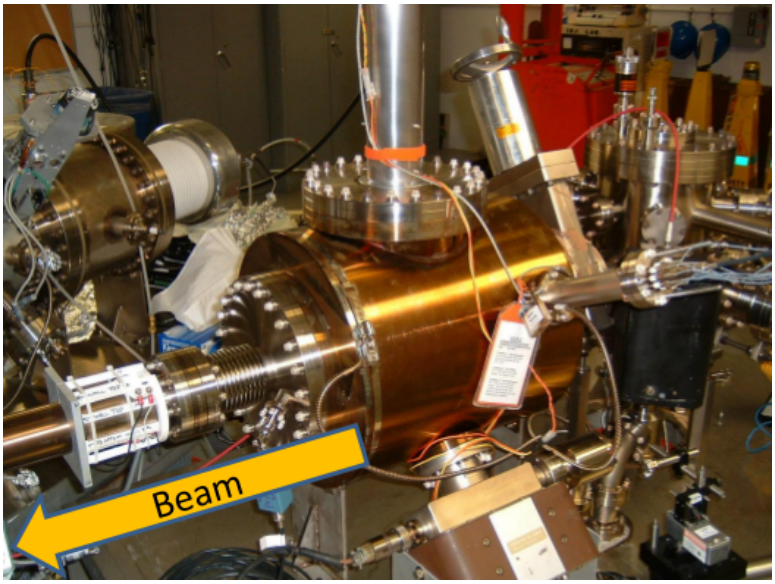

Figure 3.3: *Inverted injector gun at Jefferson Lab. Electrons are produced here then injected into the accelerator.*

The beam then travels to a chopping aperture which contains a separate slit for each experimental hall. The size of these slits and the laser intensity controls the amount of current delivered to the Hall. A rotating electric field sweeps the beam over the slits with a frequency

of 1497 MHz. The beam is accelerated to 45 MeV by SRF cavities and is injected into the North Linac for further acceleration.

In the North Linac the beam travels through twenty cryomodules each containing eight superconducting niobium cavities. Two cavities being tested are pictured in Figure 3.4. The cavities are cooled by 2 K helium coolant from the Central Helium Liquefier (CHL). The CHL also supplies the cooling power to the Qweak target.

Figure 3.4: *Superconducting radiofrequency cavities being worked on at Jefferson Lab.*

As the electrons enter the East Arc they have a nominal energy of 645 MeV, 45 from the injector and 600 from the North Linac. Then, they enter the South Linac for another nominal 600 MeV acceleration. The acceleration in each Linac can be fine-tuned to meet the experimental needs of the Halls.

After the South Linac the electrons have completed "one pass" and can be delivered to the experimental halls via the Beam Switch Yard (BSY) or they can enter the West Arc for another pass around the accelerator. Each pass adds a nominal 1200 MeV to the electron

energy. Three different electron energies can be accelerated in the linacs simultaneously by separating them by frequency. However, when traveling through an arc different energies require different magnetic field strength to bend the proper amount. Higher energy electrons require a higher magnetic field to bend the same amount as lower energy electrons.

At the entrance to both arcs the electron beam is separated by energy and sent through one of five arc pathways each tuned to bend a different "pass" of electron energy. After the arc and before the linac the different energy beams are then recombined for simultaneous acceleration.

Once the beam reaches the correct beam energy the BSY separates the 1497 MHz stream of electrons into 499 MHz "beam buckets" for delivery into the Halls.

3.2.2 Beam Monitoring

Beam properties can cause false asymmetries in the measured experimental asymmetry. These effects are controlled by constantly monitoring the beam properties while taking production data. In addition to continuous monitoring more invasive measurements of the beam properties are done periodically. One of the ways a false asymmetry can be introduced into the Qweak measurement is if a beam property is correlated with the measured asymmetry and that property has a mean that is nonzero. A false asymmetry of this type can be described by,

$$A_{false} = \sum \frac{1}{2Y}\frac{\partial Y}{\partial P_i}\Delta P_i = \sum \frac{\partial A}{\partial P_i}\Delta P_i \ , \tag{3.1}$$

where Y is the detector yield, P_i represents a parameter of the beam, and A is the measured asymmetry. $\frac{\partial Y}{\partial P_i}$ represents a detector's yield sensitivity to a beam parameter. The value $\frac{\partial A}{\partial P_i}$ is the detector's sensitivity to that beam parameter and ΔP_i is the helicity correlated mean of the beam parameter defined as $P_+ - P_-$.

The beam is continually characterized by Beam Position Monitors (BPM) Figure 3.5(a) and Beam Charge Monitors (BCM) Figure 3.5(b). A BPM is made of four antennas parallel to the beam direction and rotated 45° from the horizontal and vertical planes in the Hall. The beam frequency of 1497 MHz and 499 MHz are harmonics of the BPM antenna electromagnetic response and the magnitude of the signal in each antenna is proportional to the distance between the beam and the antenna. Using the signal magnitude in each antenna one can determine the position of the beam.

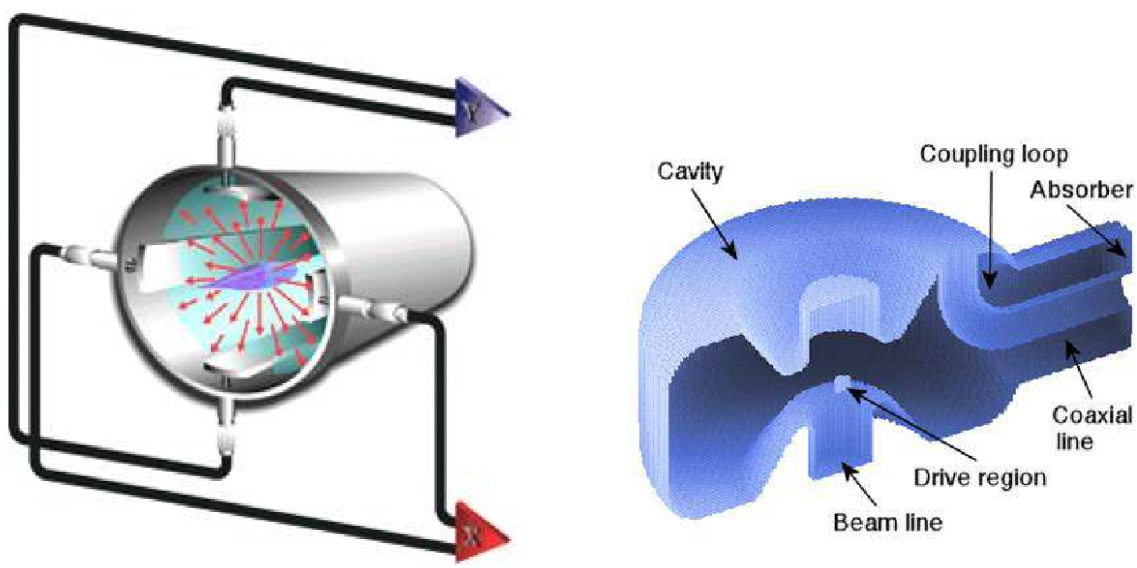

(a) Beam Position Monitor (b) Beam Charge Monitor

Figure 3.5: *Devices used for continuously monitoring beam properties. A BPM reports the position of the beam and a BCM reports the intensity of the beam.*

The BCMs are doughnut shaped cavities that resonate when beam passes through the center. The magnitude of the resonance is proportional to the charge within the cavity. The BCMs are good measures of the relative charge but need to be calibrated using the UNSER monitor to provide an absolute measurement. The UNSER monitor uses electromagnetic induction in a paramagnetic current transformer to determine the charge.

3.3 Main Detectors

The Qweak spectrometer focuses the scattered electrons of interest from the target onto each of the eight main detectors. They are made of Spectrosil 2000, a fused silica, with dimensions 200x18x1.25 cm. Each main detector bar is two pieces of fused silica, each 100 cm long, glued together using UV transparent adhesive (SES-406). Light guides are glued to the edges of the active area to accomodate the 5 in Electron Tubes 9312WKB photomultiplier tube (PMT), which is sensitive to light with wavelengths as small as 185 nm. Scattered electrons are incident on the main detector bars at 22° from normal.

Fused silica was chosen as the radiator because it is radiation hard and does not scintillate. The detectors are azimuthally symmetric and placed in light tight boxes ∼330 cm from the beam center. Relativistic electrons entering the quartz produce Cerenkov light, which reaches a PMT on each end of the bar.

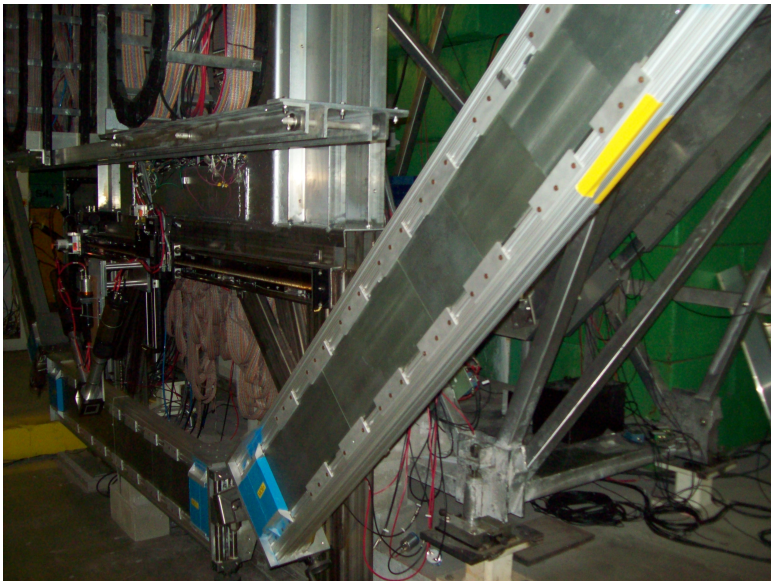

Figure 3.6: *Main detectors as installed in Hall C.*

The main detector bars are preradiated with 2 cm of lead to reduce the signal of soft back-

grounds. The preradiator also increases the signal of the desired 1 GeV electrons by a factor of 8 through electromagnetic showering. However, the preradiator causes an additional spread in the number of photons collected per event. This extra noise corresponds to a 10% decrease in detector resolution.

The main detectors require low noise electronics in integrating mode. Custom 18-bit analog to digital converters (ADCs) and current to voltage preamplifiers developed at TRIUMF were used in the electronics chain to reduce electronic noise.

Much more detail on the main detectors can be found in Peiqing Wang's dissertation [45].

3.4 Qweak Spectrometer

The Qweak spectrometer is made of three lead-antimony acceptance defining collimators, a toroidal focusing magnet, a shielding wall, and drift chambers. The spectrometer is used to periodically determine the momentum transfer distribution of the accepted electrons. Design and installation of the Qweak apparatus are shown in Figures 3.7(a) and 3.7(b).

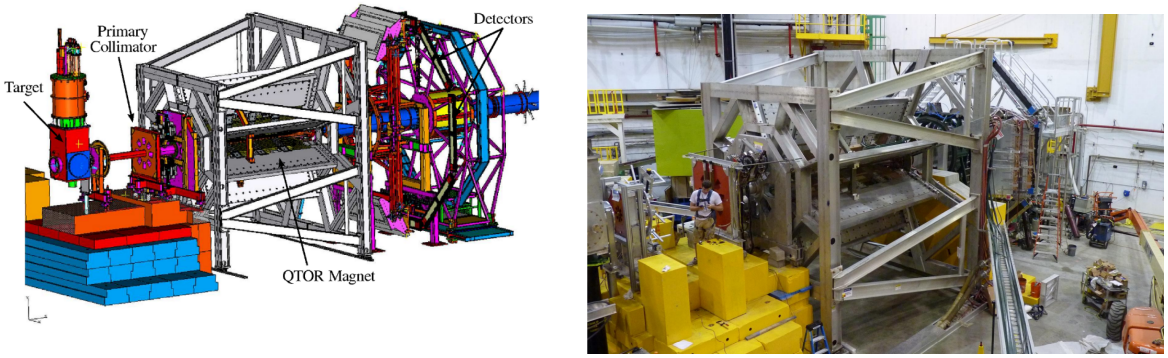

(a) Schematic of the Qweak apparatus

(b) Qweak apparatus, as installed (without shielding)

Figure 3.7: *The Qweak apparatus as designed and as installed in Hall C at Jefferson Lab.*

3.4.1 Collimators and Shield Wall

The first collimator is just downstream of the target. It limits the acceptance to be slightly larger than the second collimator. A water-cooled tungsten collimator with an inner radius of ∼7 mm was placed inside the first collimator and is used to reduce the number of electrons that can interact with the beamline aluminum. The second, or primary, collimator defines the acceptance of the experiment to be $\sim 9\pm2^\circ$ laboratory scattering angle. The third collimator is just before the toroidal magnet and further cleans up the electron flux before reaching the magnetic field region. After the magnet there is a 1 m thick barite ($BaSO_4$)-loaded concrete wall that makes up one side of the detector shield hut. The design and composition of the collimators and shield wall were motivated by simulations done by Katherine Myers and Juliette Mammei [27, 24].

The detector shield hut is big enough to house the main detectors and the vertical drift chambers. Other than the entrance holes in the shield wall and multiple turn entrance corridors, the detector shield hut is hermetically sealed from the experimental hall. This suppresses backgrounds like the estimated 200 MHz Bremsstrahlung photons in air [45].

3.4.2 Toroidal Magnet

The toroidal magnet is after the third collimator and before the shield wall. It is the large gray structure in the middle of Figure 3.7(a). The magnet requires a 10 kA power supply at 130 V and has a field integral of 0.67 T·m along the central trajectory of the elastically scattered electrons. The purpose of the magnet is to focus the elastic electrons, which are of interest to the Qweak experiment, onto the main detector bars and bend the lower energy particles away from the main detector bars. There is no line of sight to the main detectors from the target so most neutral particles are absorbed by a collimator or the shield wall.

The Qweak coordinate system including the toroidal magnet coils is shown in Figure 3.8.

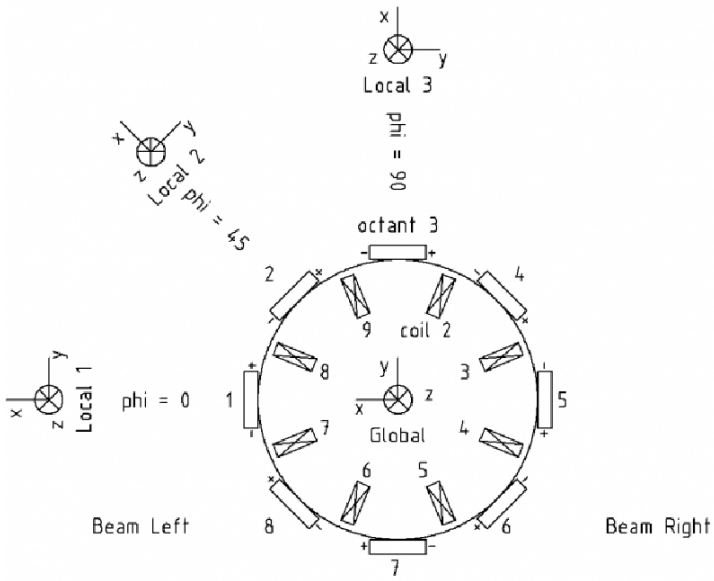

Figure 3.8: *Qweak coordinate system looking downstream.*

The toroidal magnet has eight-fold symmetry and is made of water-cooled iron-free copper. The dimensions of the racetrack design are 2.2 m long in each straightaway and the turns have an inner radius of 0.235 m and an outer radius of 0.75 m.

The scattered electrons that reach the main detectors create an image that is 10 cm tall, 2 m, and "moustache" shaped.

The electron energy changed from Run I to Run II, which required a change of magnetic field strength. For the electron energy of 1.160 GeV for Run I the nominal toroidal current was 8920 A. For the lower energy of 1.157 GeV of Run II the nominal toroidal current was 8900 A.

More information on the spectrometer, particularly the magnetic field mapping, can be found in Peiqing's Master's Thesis [44].

3.4.3 Tracking Detectors

The asymmetry of the elastically scattered electrons is approximately proportional to the four momentum transfer, Q^2, as shown in Equation 3.2. A tracking system for Qweak is necessary to measure Q^2 to 0.5%, and it is used to determine the origin of some backgrounds.

$$A = \frac{-G_F}{4\pi\alpha\sqrt{2}}[Q^2 Q_W^p + Q^4 B(Q^2)] \tag{3.2}$$

Solely from knowing the geometry of the tracking system, Q^2 can be determined to 1%. However, to reach the final goal of a 4% uncertainty on Q_W^p a full tracking system was needed. The main detector light yield varies over the length of the quartz bar. This effect needs to be accounted for and cannot be measured while in integration mode. To measure this effect one needs to map the light yield over the quartz bar at a relatively low current (∼1 nA) to record the position/angle and light yield of individual electrons.

Only two opposing octants are instrumented with tracking detectors at one time. Rotation mechanisms were designed so that there would be full coverage of all octants and redundant coverage of one pair of octants.

3.4.3.1 GEMs

Gas electron multipliers (GEMs) were supposed to be used just downstream of the first collimator. This area was estimated to receive the second highest dose of radiation, after the beam dump. GEMs were chosen because they are radiation hard and can handle a high rate of incident electrons.

The Qweak GEMs were designed to have a position resolution of 100 μm and would provide the tracking system with a "point of entry". The detector consists of three copper coated

kapton sheets separated by 1 mm. Each kapton sheet is covered with 50 μm through holes separated by 100 μm. The detector is flushed with 70% argon 30% carbon dioxide mix. The argon facilitates ionization and the greenhouse gas, carbon dioxide, absorbs the X-rays emitted after ionization. The X-rays can mimic electron signals and smear the resolution of the cascade in position and time.

A potential difference is maintained between the copper on the two sides of the kapton. This creates a 40 kV/cm electric field in the region of the through holes. This high electric field accelerates liberated electrons and creates a cascade which is then collected by copper strips. Each kapton layer provides $\sim 10^4$ signal multiplication of the incident scattered electron. Figure 3.9 provides a schematic for signal amplification.

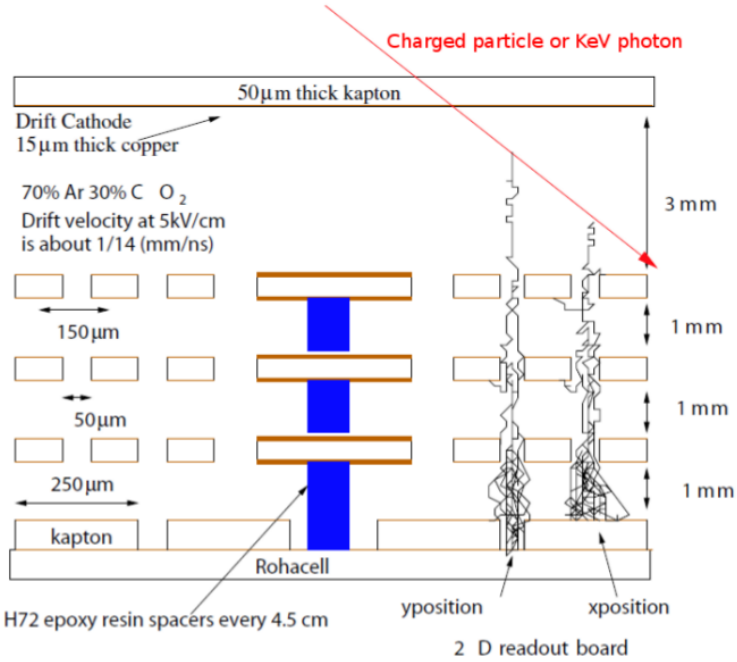

Figure 3.9: *Gas Electron Multiplier schematic.*

The flux on a GEM during a tracking run was estimated to be 1000 Hz/mm^2 and with an active area of 300 cm^2 the rates were expected to fall within the operational limits of GEMs

used in previous experiments. Unfortunately, the GEMs were nonfunctioning at the start of the experiment. Due to the high radiation in the GEM installation area little work could be done to repair the detectors.

3.4.3.2 Horizontal Drift Chambers

The horizontal drift chambers (HDC) are positioned downstream of the primary collimator. The purpose of the HDCs is to provide the Qweak tracking system with the angle and position of the electron before it is bent by the toroidal magnet. The HDCs were designed to have an angular resolution of $\sim$0.6 mrad and a position resolution of $\sim$200 μm. Five HDCs were fabricated at Virginia Tech with the intention of using four of them during Qweak and having a spare.

The resolution is a function of the sense wire spacing, the left-right ambiguity, and the drift-time spectra. The drift-time spectra is used to calculate how far from the sense wire the particle traveled. The drift time to distance conversion is a well-defined function.

The rotation mechanism supports four HDCs and is human-powered even though each detector is about 25 kg. This is possible because the load is balanced with two detectors on each side, or arm, of the rotator. The HDCs are before the magnet so they must be able to withstand the huge rate of Møller electrons.

The HDCs are flushed with a 65% argon 35% ethane mix which is bubbled through isopropyl alcohol. The argon is stable and ionizes easily, ethane is the X-ray absorbing greenhouse gas, and the alcohol bubbling has been shown to increase the life of drift chambers at Jefferson Lab.

Each HDC has an active area of about 70 cm in the radial direction by 50 cm in the azimuthal direction. They consist of six planes labeled x, u, v, x', u', v'. Each plane has a pattern of

sense wires and field wires running parallel to each other and transverse the direction of the beam. Each wire plane is sandwiched between aluminized mylar ground planes.

A cell in an HDC is defined by a sense wire at the center and parallel field wires on either side sandwiched between two aluminized mylar ground planes. The field wires and the aluminized mylar cathode are grounded and the sense wires are held at 2150 V.

Many chambers of this type offset similar planes by half of a cell so one can determine which side of the sense wire the electron traversed. For the HDCs, offsetting planes was not done because the incident angle of the electrons of interest was large enough, 7°, that offsets were unnecessary.

The x and x' plane wires point radially, the u and u' wires are angled by 53.231°, and the v and v' wires are angled by -53.231°. Each chamber has 192 sense wires.

The estimated rate on the HDCs was 2.6 MHz/nA. A rate of less than 1 MHz is required for good efficiency. The leakage current was driven by the radiation from the target and tungsten collimator. For good efficiency and detector longevity the residual radiation in the Hall needed to decay for approximately eight hours.

Two chambers, separated by ∼40 cm along the direction of the beam, were placed on each side of the rotator. The electrons of interest traveled through one set of two detectors before reaching the toroidal magnet. The HDCs as installed are shown in Figure 3.10.

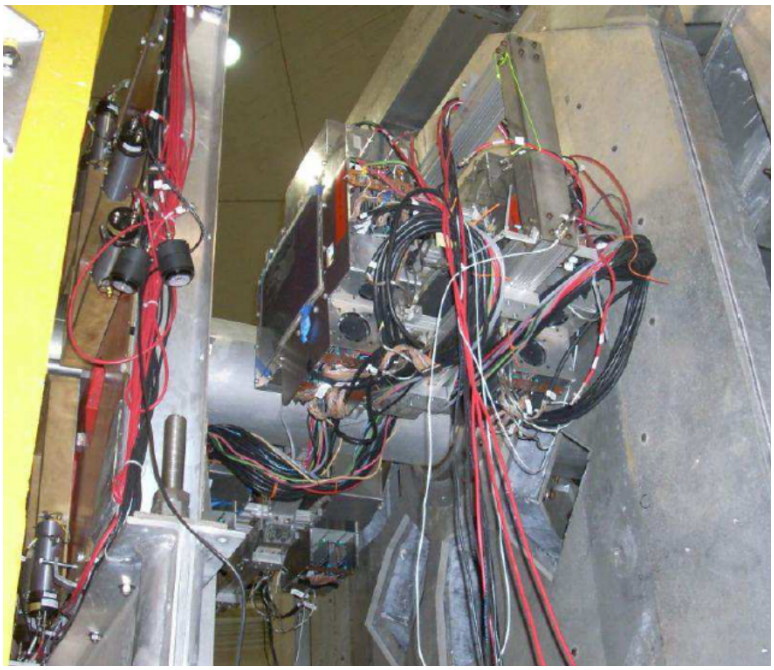

Figure 3.10: *Horizontal Drift Chambers as installed in Hall C.*

A projection of line segments extracted from data onto the primary collimator is shown in Figure 3.11.

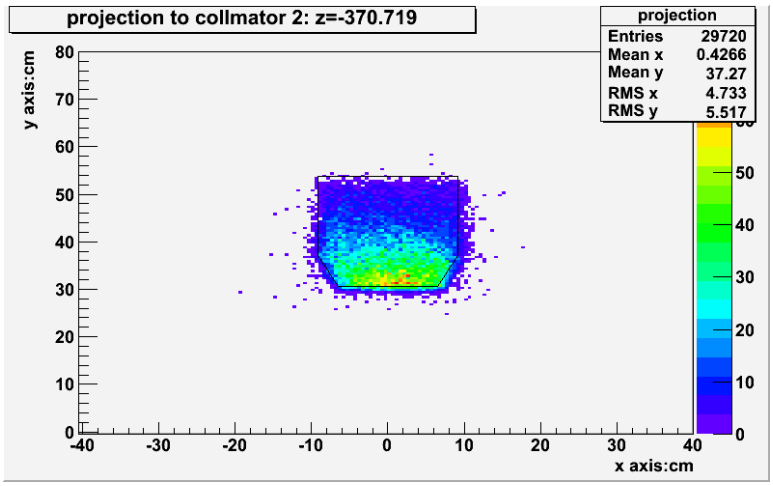

Figure 3.11: *HDC line segment projection onto primary collimator.*

One can clearly see the shape of the hole in the primary collimator. This was one of the many checks to insure the detectors and track reconstruction software were working properly.

3.4.3.3 Vertical Drift Chambers

The vertical drift chambers were constructed by collaborators at William and Mary and are located directly upstream of the main detectors. Each detector has an active area of 53.3x204.5 cm and contains 558 sense wires. There are two planes of wires per detector u and v.

Like the HDCs, the drift-time spectra is used to increase the resolution of the detectors. This resolution was $\sim$100 μm and provided a line segment of the scattered electron's trajectory after being bent by the magnet.

The VDCs are angled at 45° to the incoming electron so they will travel through more active area within the detectors and trigger more sense wires. These detectors are used to determine the trajectory of the electrons after they are focused by the magnetic field generated by the toroidal magnet.

Due to the high number of channels needed for data acquisition (4 detectors x 558 wires per detector = 2232), multiplexing electronics were used. This reduced the number of channels by a factor of nine.

The detectors are parked in octants 1 and 5, beam left and beam right, respectively. The VDCs on beam left are known as package 2 and the VDCs on the right are package 1.

The rotation mechanism is computer controlled and can rotate $\pm 90°$, which covered all octants. The VDCs were moved out of the electron acceptance envelope during integration mode when the rate was too high for event mode data-taking. Octants 1 and 5 can be redundantly covered with both sets of VDCs to control for systematic differences between

the detectors.

More information on the VDCs can be found in John Leckey's dissertation [21].

3.4.3.4 Trigger Scintillator

Qweak uses two scintillators, George and Martha, as timing triggers during event mode data-taking. Martha is attached to VDC package 1 and George is attached to VDC package 2. They are just upstream of the main detectors and are only used during low current (50 pA to 100 nA) running.

Saint Gobain manufactured the scintillator material, BC-408, which is sensitive to all types of radiation. However, a Constant Fraction Discriminator (CFD) was used for triggering because typical discriminator timing depends on the pulse height. Since the height of the pulses is expected to vary over the length of the scintillator, CFDs were used to eliminate the "time walk".

More information about the Trigger Scintillators can be found in Katherine Myers's dissertation [27].

3.5 Scanner

Some comparison between integration mode and event mode is needed because there is no guarantee that the scattered electron beam will have the same qualities at the integration mode current of 180 μA and the event mode current of 100 pA.

To make a comparison between the two currents (spanning seven orders of magnitude) a rate scanning system was designed. The active area of the scanner is made of two 1x1x1 cm

pieces of quartz each viewed by a single PMT via an air core light guide. A coincidence between the two PMTs is required before the event is recorded to reduce the number of random and low energy triggers.

The scanner was installed on a movable frame in octant seven (beam bottom). The movable frame can position the scanner on all points of the quartz bar. With this positioning system a rate map can be obtained at both event mode and integration mode currents. A detailed comparison is currently underway. However, qualitatively the simulation and experimental rate maps agree as seen in Figures 3.12 and 3.13.

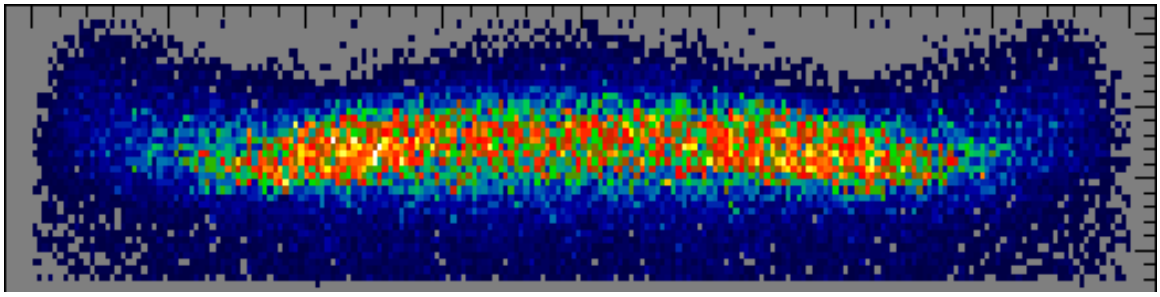

Figure 3.12: Simulated scanner rate map.

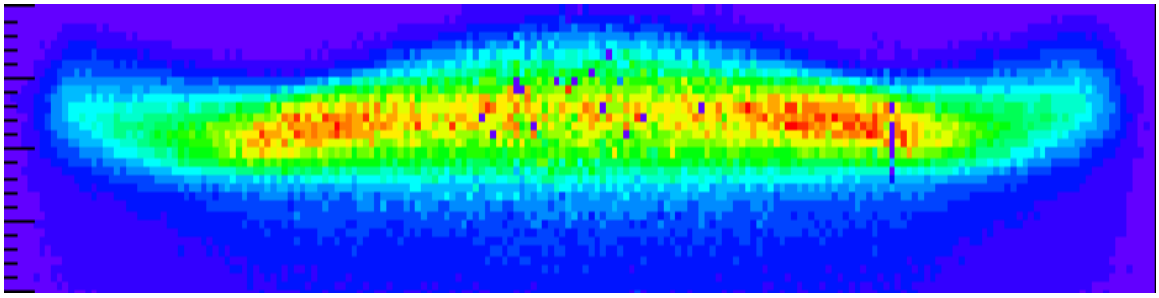

Figure 3.13: Experimental scanner rate map.

3.6 Polarimetry

Knowing the beam polarization is essential to extracting the value of Q_W^p. Polarimetry has the largest error allotment (1%) of the systematic corrections. In order to make this measurement two polarimeters are used. The Møller Polarimeter is invasive but well tested and the Compton Polarimeter is noninvasive but relatively new to Hall C.

3.6.1 Møller Polarimeter

The Hall C Møller Polarimeter detects electron-electron interactions in a thin iron target. The iron target's electrons are longitudinally polarized by a 4 T magnetic field generated by superconducting magnets. The incoming electron is longitudinally polarized and supplied by the injector in the same method as the electrons for the Qweak experiment.

An asymmetry between left- and right-handed electrons is formed, and because the interaction is well understood, the polarization of the incident electron beam is extracted. This polarimeter is limited to ~ 1 μA of incident electron beam current. Qweak cannot take production data while making a Møller polarization measurement.

The cross section for the Møller interaction is described by the following equation,

$$\frac{d\sigma}{d\Omega} = \frac{d\sigma_o}{d\Omega}[1 + P_t^{\parallel} P_b^{\parallel} A_{zz}(\theta)] \ , \tag{3.3}$$

where $\frac{d\sigma_o}{d\Omega}$ is the cross section neglecting polarization and $P_t^{\parallel}$ and $P_b^{\parallel}$ are the target and beam longitudinal polarizations. $A_{zz}(\theta)$ is the analyzing power as a function of the center-of-mass scattering angle and is given by

$$A_{zz}(\theta) = -\sin^2\theta \frac{8 - \sin^2\theta}{(4 - \sin^2\theta)^2} \ . \tag{3.4}$$

The Møller polarization measurement is done at least twice a week but more frequently if the beam polarization has likely changed due to changes in the injector.

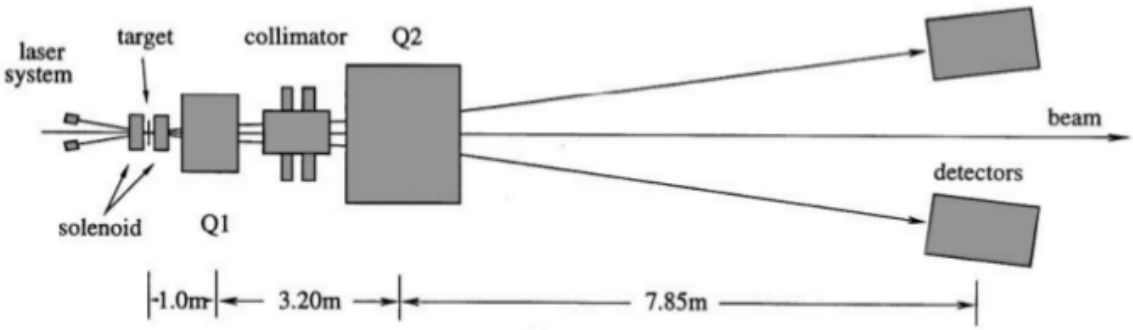

Figure 3.14: *Møller polarimeter schematic. Q1 and Q2 are magnets used to focus scattered electrons with the proper kinematics into the detectors.*

The measurement is made with the half-wave plate inserted and the half-wave plate removed from the injector laser. This is to confirm the half-wave plate only affects the sign of the polarization and not the magnitude.

3.6.2 Compton Polarimeter

The Compton Polarimeter is noninvasive so the Qweak experiment can take production data while a Compton polarization measurement is taking place. The Compton Polarimeter was installed and commissioned at the same time as the Qweak experiment and used the Møller Polarimeter as a benchmark.

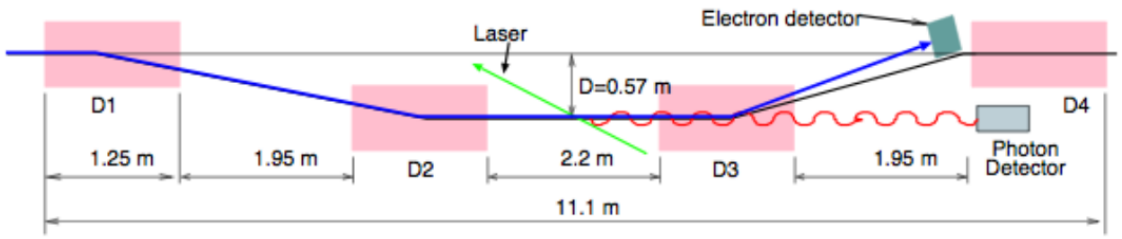

Figure 3.15: *Compton polarimeter schematic. Dipole magnets (D1-4) direct the beam into a chicane where the laser intersects the beam. The electrons that interact have lower energy so they bend into the electron detector.*

The Compton Polarimeter operates by Compton scattering photons off the incident electrons within the electron beam then measuring the electrons and photons that interact. This system provides two measurements of the polarization of the beam by measuring the asymmetry between the left- and right-handed electrons interacting with circularly polarized light. This interaction is described by,

$$P_e = \frac{A_m}{P_\gamma A_z} \ , \tag{3.5}$$

where P_e is the polarization of the electron beam, A_m is the asymmetry measured between the left- and right-handed incident electrons, P_γ is the circular polarization of the laser, and A_z is the analyzing power.

Four dipole magnets (D1-4) bend the beam into the chicane where it interacts with a 532 nm 10 W laser. The electrons that interact with the laser light lose a small amount of energy. This causes them to be bent more than the primary electron beam by the third dipole magnet so they become separated from the primary beam and strike the electron detector. The photons are almost exclusively backscattered, have energies of 10-50 MeV, and strike the photon detector as shown in Figure 3.15.

The photon detector was first made of a CsI crystal but phosphorescence diluted the desired

signal and made a polarization extraction too complex. From February 25, 2011 to April 18, 2011 a germanium silicon oxide (GSO) crystal was borrowed from Hall A. This crystal did not suffer from phosphorescence and made a proper measurement of the asymmetry. However, it needed to be returned to Hall A and a lead-tungstate ($PbWO_4$) detector was installed, and used successfully, for the rest of the experiment.

The scattered electrons are detected by 96 diamond strips on four planes. The position is determined using the 200 μm pitch of the planes and coincidences between diamond strips on separate planes. For the Qweak beam energy of 1.16 GeV and the magnetic field produced by dipole D3, the Compton edge is 23 mm from the center of the beam.

The laser is injected into a Fabry-Pérot cavity to induce a standing wave. The cavity is adjusted so the density of photons is at a maximum where the electron-photon interaction takes place.

A detailed article describing a similar Compton polarimeter constructed for Hall A was published in a technical report at Jefferson Lab [19].

3.7 Target System

The Qweak target system consists of a main liquid hydrogen cell used for production data-taking and a matrix of solid targets used for background measurements and ancillary tests thermally coupled to the bottom. A schematic of the Qweak target is shown in Figure 3.16. The solid target device is not shown in the figure but is placed on the bottom of the hydrogen cell between the "J" pipes. The solid target apparatus is shown in Figure 3.19.

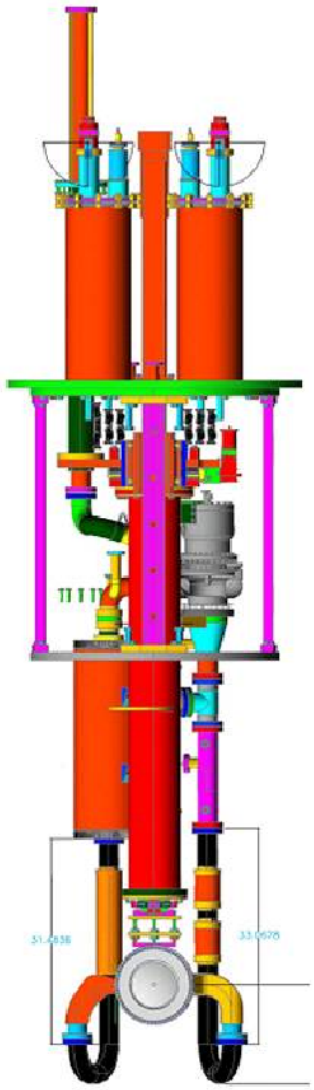

Figure 3.16: *Qweak target schematic.*

3.7.1 LH_2 Target

The hydrogen cell is 34.4 cm long and can dissipate 2500 watts of power deposited by the electron beam, which makes it the current highest power cryogenic target in the world. It contains 55 liters of hydrogen at 20 K and 35 psia, which is circulated using a modified

automobile turbo.

The design of the target was motivated by studies done with ANSYS FLUENT computational fluid dynamics (CFD). The hydrogen flow is transverse the electron beam direction and early CFD modeling revealed some hot spots within the cell. The flow speed was increased at these points to keep the temperature within specifications. The most notable hot spots were at the entrance and exit windows of the cell.

The hydrogen flows around a series of pipes, which contain helium at 4 K and 15 K provided by the central helium liquifier (CHL) and the end station refrigerator (ESR), respectively, which serves as a heat exchanger. There is also a high power heater, which can replace the heat deposited by the electron beam during beam trips. This heater is used to stablize the target in conjuction with the flow of the 4 K and 15 K coolant in a proportional integral derivative (PID) feedback system.

The stability of the target was an unknown for the experiment and had the potential to have significantly increase the time needed to reach the statistical error goal. Much effort was put into ensuring the stability of the target. The design criteria for the target density fluctuation contribution to the statistical width of the asymmetry measurement was less than 50 ppm at 180 μA at 4x4 mm^2 raster.

The fast polarization flip is done at a frequency of 960 Hz and the raster was designed to have a matching beat frequency. This insures each integration period (MPS) has the same complete raster pattern on the target, which prevents systematic differences in the beam position between macropulses.

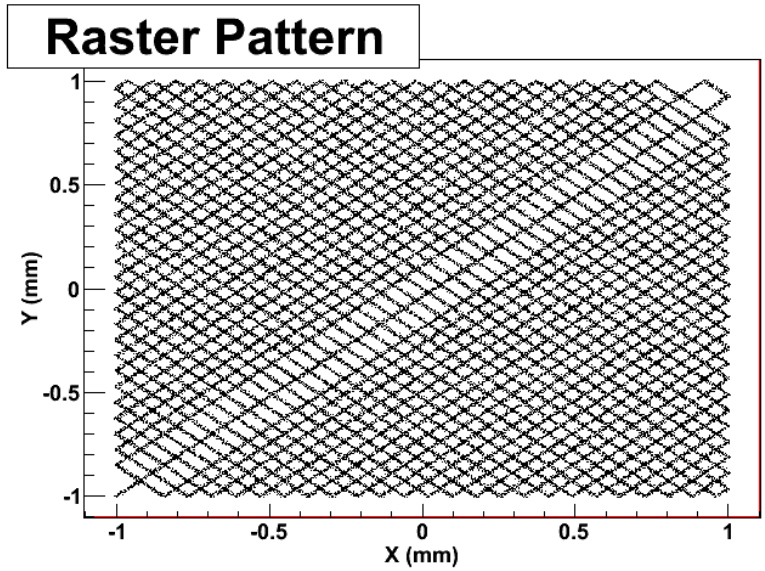

Figure 3.17: *Raster pattern on the face of the target. This is a 2x2 mm^2 pattern but the typical Qweak raster is 4x4 mm^2. One complete cycle of this pattern is completed at a frequency of 960 Hz.*

The instrinsic size of the electron beam is $\sim$ 2 μm in dimensions transverse to the beam direction. This results in a power density on the target that is too high. A set of fast (25 kHz) raster magnets are used to distribute the power deposited uniformly over the face of the target. A typical raster pattern is shown in Figure 3.17.

To determine the contribution of the target density fluctuations to the statistical width the electron beam raster size was varied and the main detector asymmetry width was measured. The results are shown in Figure 3.18.

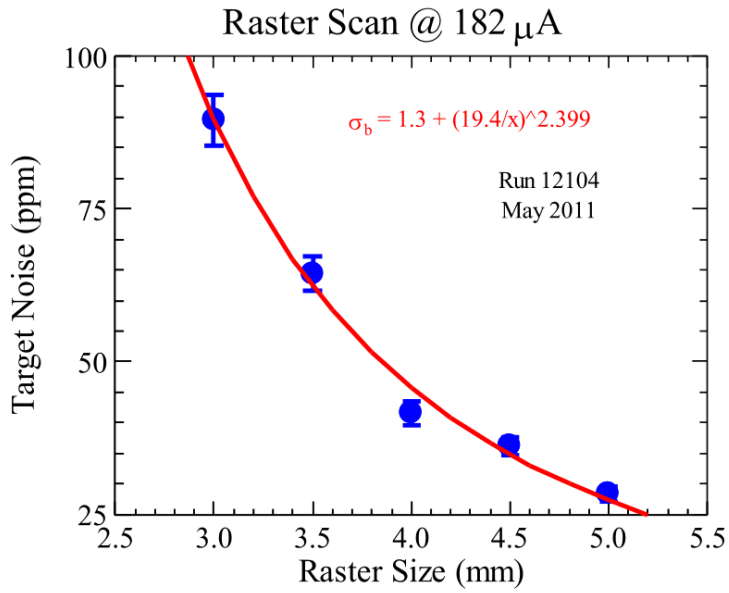

Figure 3.18: *Target density contribution to measured asymmetry width. The target met its design goal of less than 50 ppm at 180 μA and 4x4 mm^2 raster.*

As one can see from Figure 3.18, at 180μA and 4x4 mm^2 raster, Qweak's typical operating conditions, the asymmetry width contribution of the target met the design goal of less than 50 ppm. This is a relatively small contribution to the statistical width ($\sim$200 ppm) of our measurement.

3.7.2 Solid Targets

The liquid hydrogen cell is aluminum and the electrons that scattered from the target windows are a significant source of background. To control this background aluminum "dummy targets" were attached to the target system. The asymmetry of the aluminum dummy targets is measured frequently to constrain the contribution from the aluminum target windows.

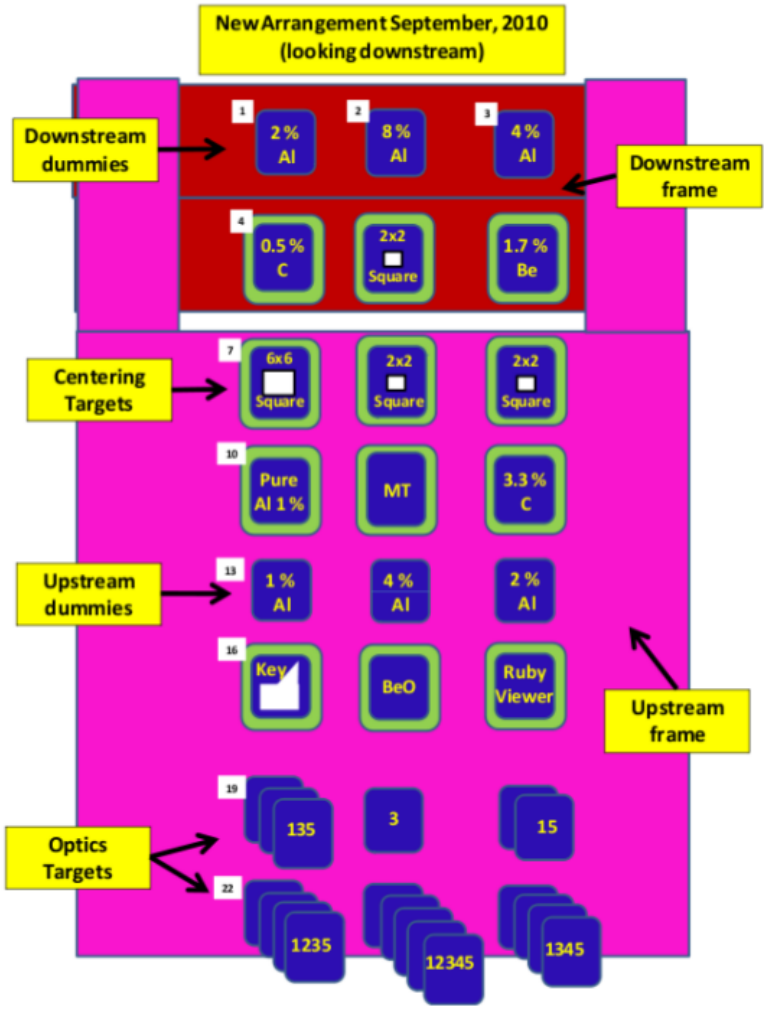

Figure 3.19: *Solid target assembly. The optics targets were primarily used for particle origin reconstruction via the tracking system.*

Three different aluminum dummy target thicknesses were used so radiative corrections could be disentangled from the measured asymmetry. The 2% and 4% aluminum targets were placed on the upstream and downstream locations of the solid target assembly to determine how the acceptance affects the measurement.

3.8 Data Acquisition

The event mode and integration mode require the Qweak experiment to have two data acquisition (DAQ) systems. The data-taking during event mode is triggered by the trigger scintillators and the rate depends on the beam current and several other factors. The data-taking during integration mode is triggered by the MPS signal from the accelerator at 960 Hz. Both systems use the CEBAF Online Data Acquisition (CODA) software to process the raw data.

In the integration mode CODA software there is a 70 μs hold off after each MPS signal is received from the accelerator. This allows the data buffers in the analog to digital converters (ADC) to be read out and the data recorded. The data-rate during integration mode is approximately 5.6 MB/s. The total data amount at the end of Qweak was approximately 20 TB.

In the event mode CODA software the primary trigger is the OR of the trigger scintillators but different systematic studies call for different triggers. Each hardware trigger has a software prescale factor that controls how often the DAQ is triggered by that specific trigger. Using this configuration several triggers can be used concurrently and separated for data analysis later.

Chapter 4

Luminosity Monitors

4.1 Introduction

Two types of luminosity monitors were designed and installed for the Qweak experiment. The "upstream" luminosity monitors are located on the front face of the primary defining collimator 5 m from the target and the "downstream" luminosity monitors are located 17 m from the target in cups inserted into the beampipe. Both sets are located in areas where the physics asymmetry is expected to be smaller than the main detectors and their primary purpose was to measure a zero, or "null", asymmetry.

The upstream set primarily detects Møller scattered electrons at 5°; this cross section is relatively less sensitive to beam energy and angle changes, so they could monitor density fluctuations within the LH_2 target. The downstream set are located at a scattering angle of 0.5° and are equally sensitive to Møllers and electrons elastically scattered from protons in the target.

The downstream set is more sensitive to helicity correlated beam properties than the main

detectors. This allows for a robust check of the helicity correlated correction algorithm before it is applied to the main detectors. Both sets of luminosity monitors are in locations where the particle flux is higher than the main detectors. As a result, a luminosity monitor statistical error should be smaller than a main detector.

4.2 Design

The design of the luminosity monitors was motivated by studies done using the particle simulation toolkit, Geant4 [3]. Each of the eight downstream luminosity monitors contain a small tapered piece of quartz made of Spectrosil 2000 fused silica from Heraeus. Their dimensions are 4x3x1.3 cm and they are situated 0.5° from the beam axis and 17 m from the target. Figure 4.1 shows the final CAD drawings submitted to Heraeus for fabrication. The downstream luminosity monitor assemblies are inserted into cups that penetrate the 2 ft diameter beampipe to within 13 cm of the beamline center. Each downstream luminosity monitor is read out with a 2 in quartz window Hamamatsu R375 photomultiplier tube (PMT). They are coupled to the quartz via a 35 cm long air-core light guide. The light guides were folded from a single sheet of highly reflective aluminum from Alanod. Figure 4.2 is a picture of the downstream luminosity monitors installed in Hall C at Jefferson Lab.

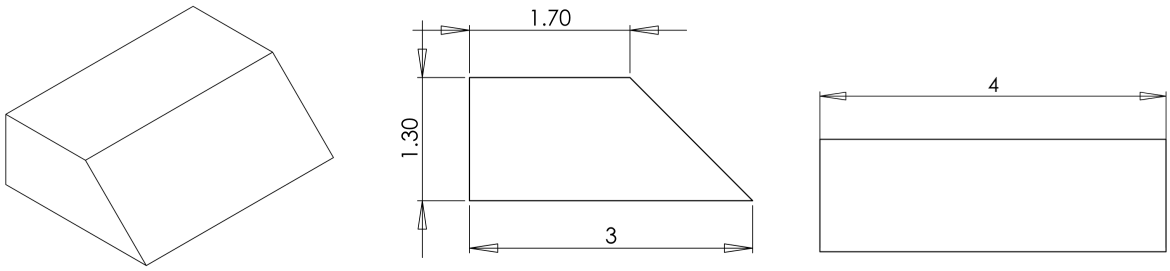

(a) Isometric view (b) Side view (c) Back view

Figure 4.1: *Downstream luminosity monitor quartz CAD drawings submmitted to Heraeus for fabrication. Units are in centimeters.*

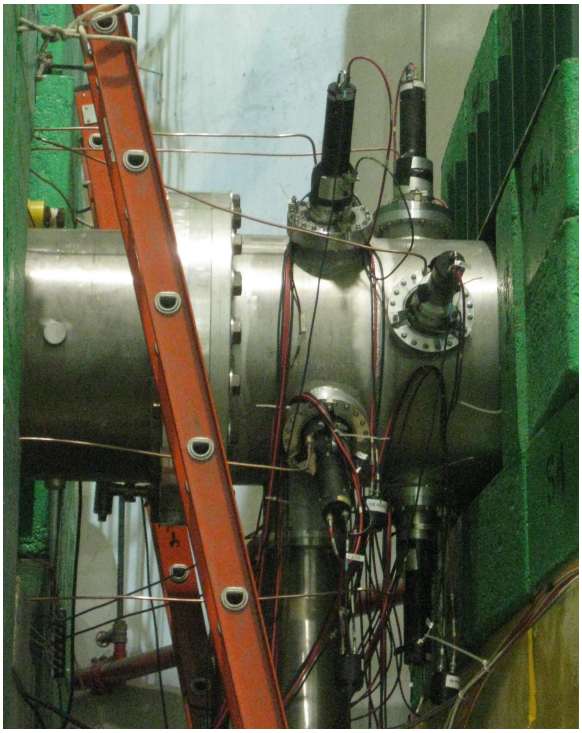

Figure 4.2: *Downstream luminosity monitors installed at Jefferson Lab. The large silver horizontal tube is the beampipe.*

The downstream luminosity monitors have an estimated ∼100 GHz flux of scattered electrons at an operating current of 160 μA and are expected to accumulate a dose of 4.8 Grad over

the life of the experiment. High-purity quartz has been used in similar applications with no degradation of light transmission with doses up to 2 Grad [11].

The four upstream luminosity monitors are composed of the same quartz as the downstream luminosity monitors but the active area is much larger. The upstream luminosity monitor quartz bars are 7x27x2 cm with 2 cm 45° notches at both ends, which allow light to escape the polished quartz surface. Both notches are then coupled to PMTs via 35 cm light guides. The upstream luminosity monitors are situated on the upstream face of the primary collimator 5 m from the target. Figure 4.3 shows the final CAD drawings of the upstream luminosity monitor quartz submitted to Heraeus for fabrication.

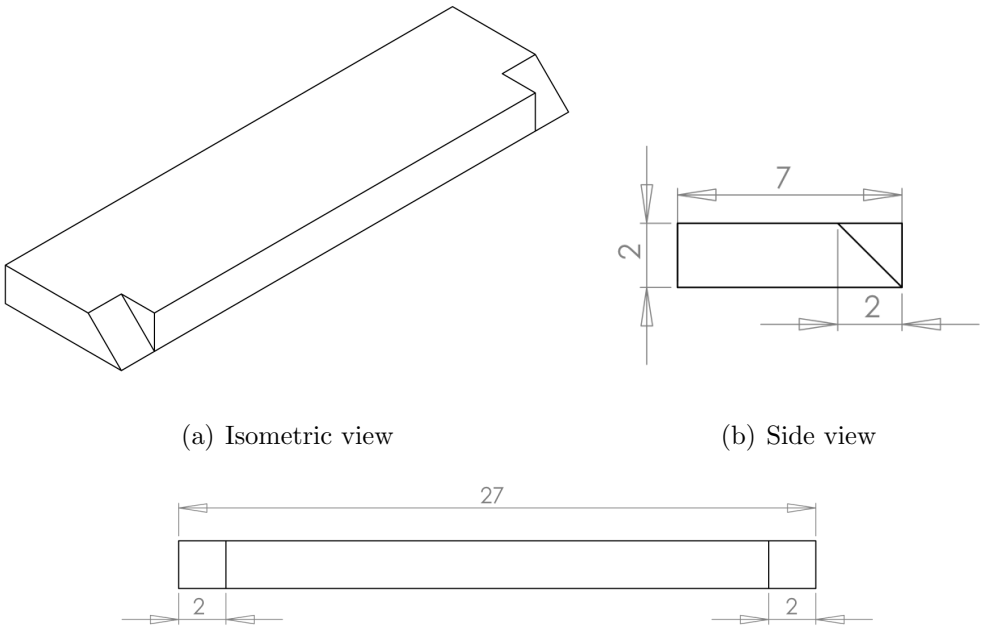

(a) Isometric view (b) Side view

(c) Front view

Figure 4.3: *Upstream luminosity monitor quartz CAD drawings submitted to Heraeus for fabrication. Units are in centimeters.*

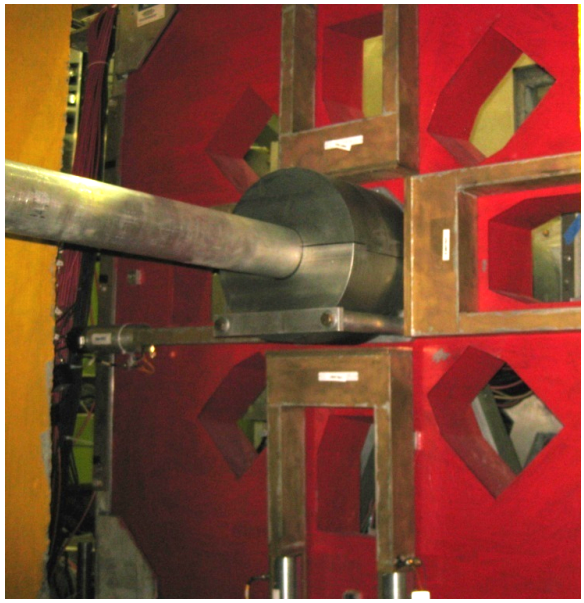

Figure 4.4: *Upstream luminosity monitors installed at Jefferson Lab. The upstream face of the primary collimator is red. Also pictured is the upstream beampipe.*

The upstream luminosity monitors primarily see Møller electrons scattered at 5°. At this angle they have an estimated rate of ∼133 GHz at 160 μA. Each quartz piece is coupled to two 2 in quartz window Hamamatsu R375 PMTs.

The Qweak experiment will run at two different ranges of currents. The high current range is from 30 to 180 μA, is called "integration mode", and is where Qweak spent the majority of its beam time. The less used but equally important "event mode" beam current range is from 50 pA to 50 nA. This low current range is necessary for the tracking detectors to record the position and angle of individual electrons as they pass through the Qweak apparatus.

The rate in the luminosity monitors is proportional to the Qweak operating current and spans seven orders of magnitude. The Hammamatsu R375, 10 stage, multi-alkali photomultiplier tube serves as the photodetector for both current regions. One needs to change the base of the PMT to switch between the two operating current ranges. In "event mode" a conventional

high gain voltage divider PMT base was used with a typical gain of $5 \cdot 10^5$ [16], which enables the detection of individual electrons. For "integration mode" the PMT base is configured to have a gain of one. To achieve unity gain in a photomultiplier tube all dynodes in the PMT must be electrically coupled as shown in Figure 4.5. In this configuration a small current of $\sim 1\mu$A is read out on the last dynode instead of single event pulses. The measured cathode current is proportional to the number of photons striking the PMT.

A multi-alkali photocathode was chosen over a bi-alkali because multi-alkali photocathodes have a lower "sheet resistance". A lower sheet resistance reduces space charge effects, which results in a more linear response from the photodetector.

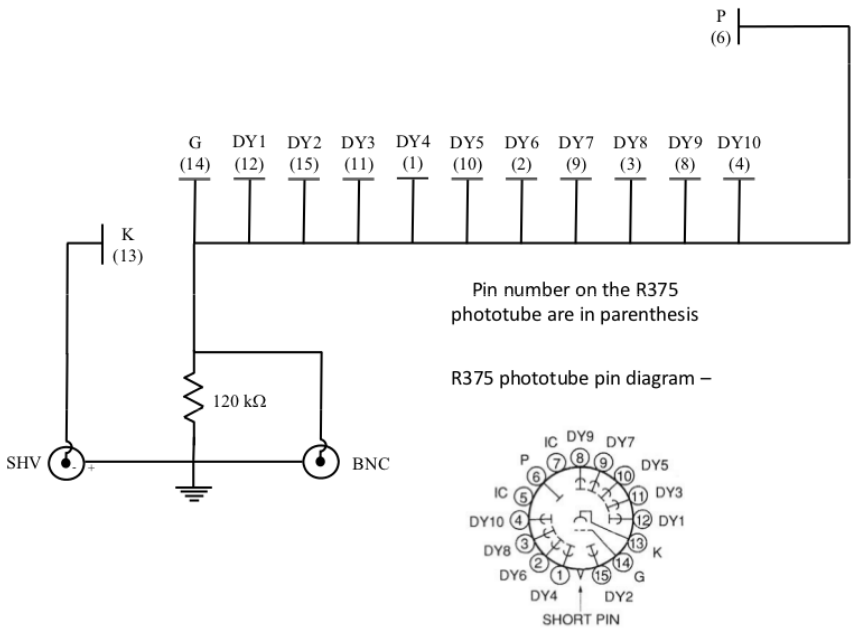

Figure 4.5: *Unity gain base wiring diagram for the R375.*

Figure 4.6 shows the integration mode signal chain for the luminosity monitors. The luminosity monitor integration mode current signals were coverted to voltages by TRIUMF

preamplifiers (Figure 4.7) and were integrated approximately every ∼1 ms using a TRIUMF VME 18-bit ADCs (Figure 4.8).

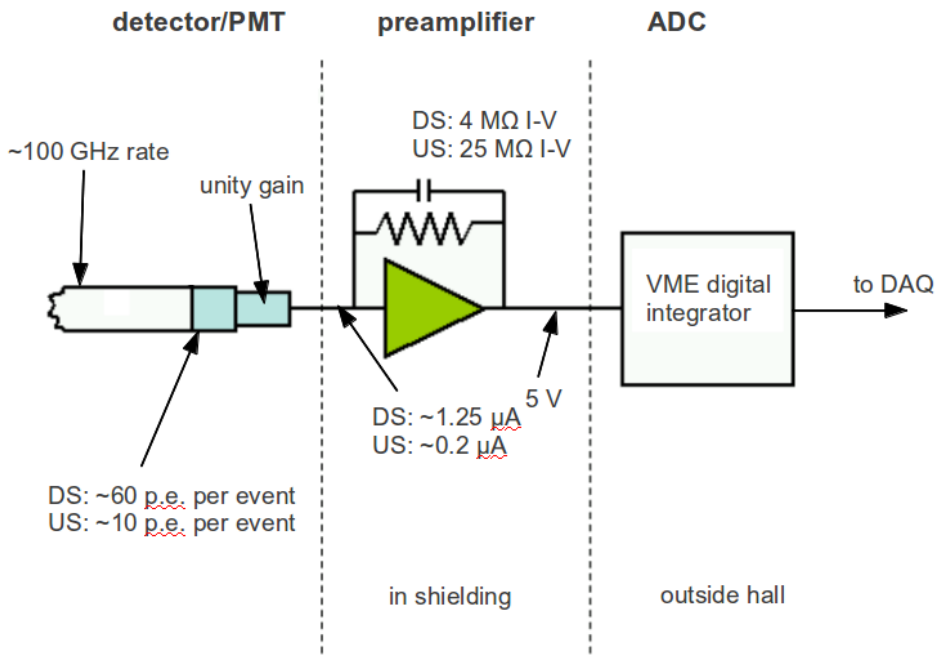

Figure 4.6: *Signal chain for the luminosity monitors. Differences between the values for the upstream (US) and downstream (DS) luminosity monitors are noted in the figure.*

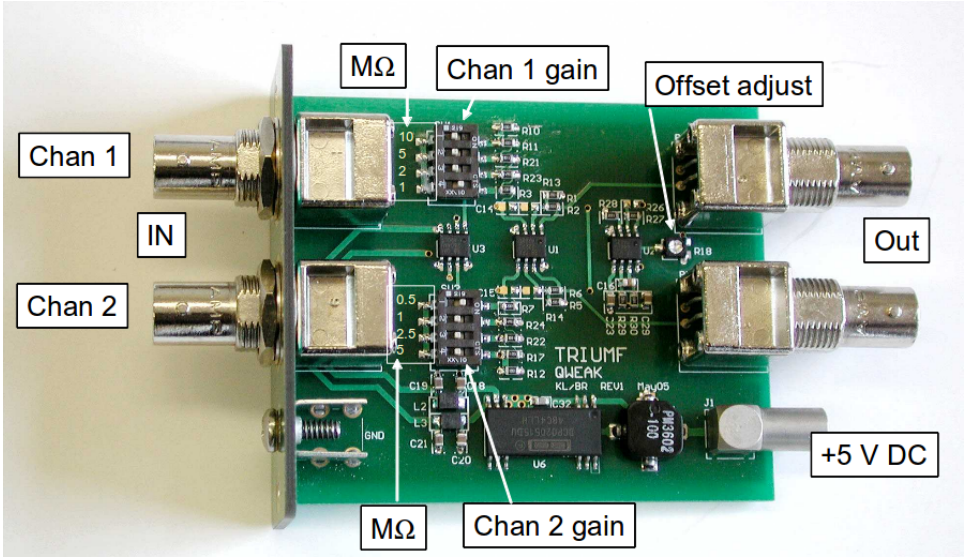

Figure 4.7: *Preamplifier design used with the downstream luminosity monitors and main detectors. The upstream luminosity monitor preamplifiers were similar but had a larger gain (up to 50 MΩ).*

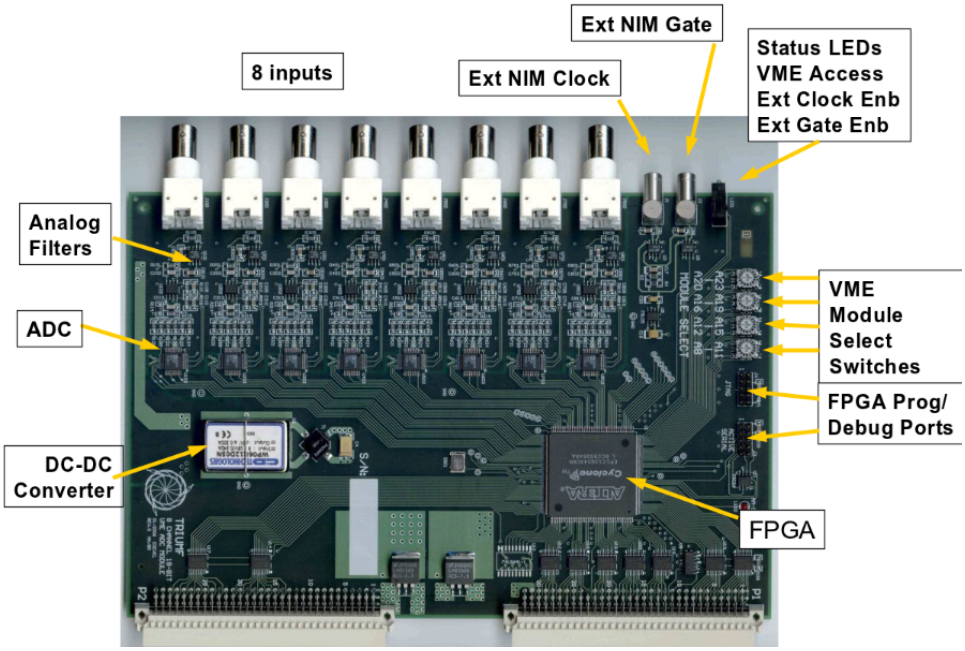

Figure 4.8: *ADCs used with the luminosity monitors, main detectors, and beam monitoring devices.*

The design of the luminosity monitors would have been less complicated if it could have incorporated plastics and/or glue. However, the main design consideration for both sets of luminosity monitors was radiation hardness. Shielding was placed in critical areas near the luminosity monitors in order to reduce the dose received by the less radiation hard components within the detectors. The design of the luminosity monitors incorporated light guides, which moved the PMTs to relatively low radiation areas. The light guides to directed the light emitted by the quartz onto the PMT. The light guides needed to be made of radiation hard material in order to survive the high radiation area.

A common light guide material is a clear plastic called lucite. This material was not an option for this application for two reasons. This material would not have survived in the radiation environment and it would have contributed, via Cerenkov radiation within the lucite, to the light detected by the PMT. A metal air-core light guide was investigated because it would

survive the radiation dose but simulations were needed to determine its light contribution. These contributions were limited to scintillation and Cerenkov radiation in were shown to be small effects in simulation [30].

Alanod makes aluminum sheets with different thicknesses and different reflective properties. Because the light guides needed to be folded the thinnest material available (0.02 in) was chosen. Light guides were made from sheets with three different quoted reflectivities to determine the best model. However, they all were observed to behave similarly. Table 4.1 shows the Manufacturer's reflectivity specifications for the three MIRO sheets used in the comparison.

Table 4.1: Manufacturer's specifications for MIRO reflectivity.

Al Sheet Type	Total Light Reflection	Diffuse Reflection
MIRO 4	$\geq$95%	<12%
MIRO 27	$\geq$95%	<6%
MIRO 27 Silver	$\geq$98%	<6%

The reflectivity of the aluminum was tested using a prototype quartz piece with dimensions 6x2x1 cm. The amount of light that escapes the quartz was determined by coupling the quartz piece to a PMT with optical grease. Of the light that escaped the quartz, $\sim$30% traveled the length of the light guide and struck the PMT. This qualitatively agrees with the SLAC E158 Scanner [18]. For the Qweak luminosity monitor light guides a photon is reflected an average of thirty times before reaching the PMT. Knowing this, the photon wavelength distribution, and the quantum efficiency of the PMT one would expect a factor of 2.5 more photons when using MIRO 27 Silver compared to MIRO 27.

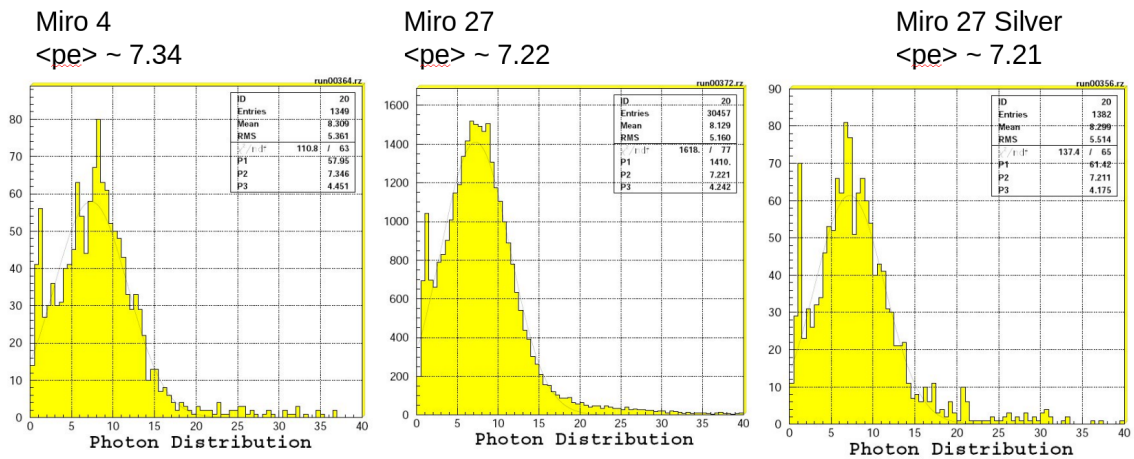

Figure 4.9: *Comparison of different MIRO material light guides. No meaningful difference in light yield was observed.*

Figure 4.9 shows that changing light guide materials did not increase the light yield in bench tests. One hypothesis to explain the unexpected agreement is that the reflectivity for UV photons is poorly controlled by the manufacturer. Since the majority of the photons emitted as Cerenkov radiation are in the UV, differences in the reflectivity in the UV would cause differences in the photon yield. Repeated attempts to attain a reflectivity as a function of wavelength for the MIRO material from the manufacturer failed.

The MIRO material comes in large sheets that need to be folded. The design of the fold pattern incorporated several features to make the final light guide robust including overlapping material and tabs for rivets. A quartz holder made of MIRO surrounds the downstream luminosity monitor quartz on all sides except the side facing the PMT. In addition to stabilizing the quartz this holder was designed to redirect any light that escaped through the surface of the quartz toward the PMT.

In general, the larger the cross sectional area of the light guide the fewer reflections occur before striking the PMT. The same is true for the length of a light guide. The cross sectional

area was constrained by the 2 in diameter of the PMTs but the length could be adjusted. A longer light guide would better shield the PMTs but would decrease the number of photons that reached the PMT. The optimal length of the light guides was found to be 35 cm.

The quartz pieces had 0.3 mm polished bevels on all edges because the manufacturer determined this prevents the quartz from chipping and prevents cuts while it is being handled. The beveled edges were shown to increase the light yield in simulation as shown in Figure 4.10. From left to right, the result of a simulation with no bevels, 0.3 mm bevels, and 0.5 mm bevels. The bevels increased the number of detected photons by ∼37%.

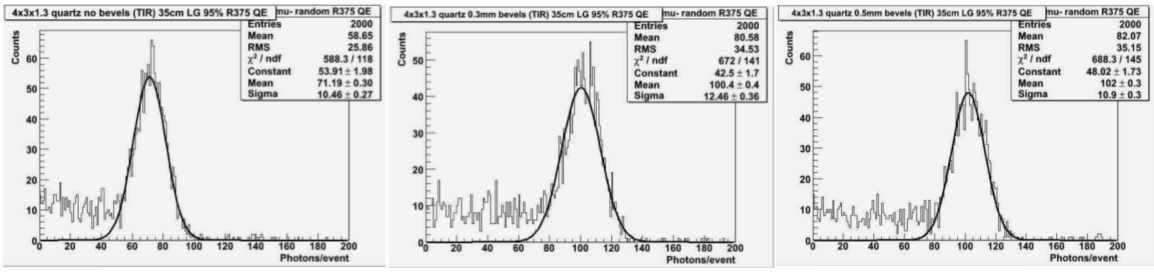

Figure 4.10: *Beveled edges in the quartz pieces were shown to increase light yield in simulation.*

The quartz pieces were expensive so during the early testing periods UVT (ultra-violet transmitting) lucite was used instead. This material could be easily machined in the Physics Machine Shop and the photoelectron yield of the UVT lucite was similar to quartz. UVT lucite was dismissed as a radiator for the final luminosity monitors because it is relatively easily damaged by radiation.

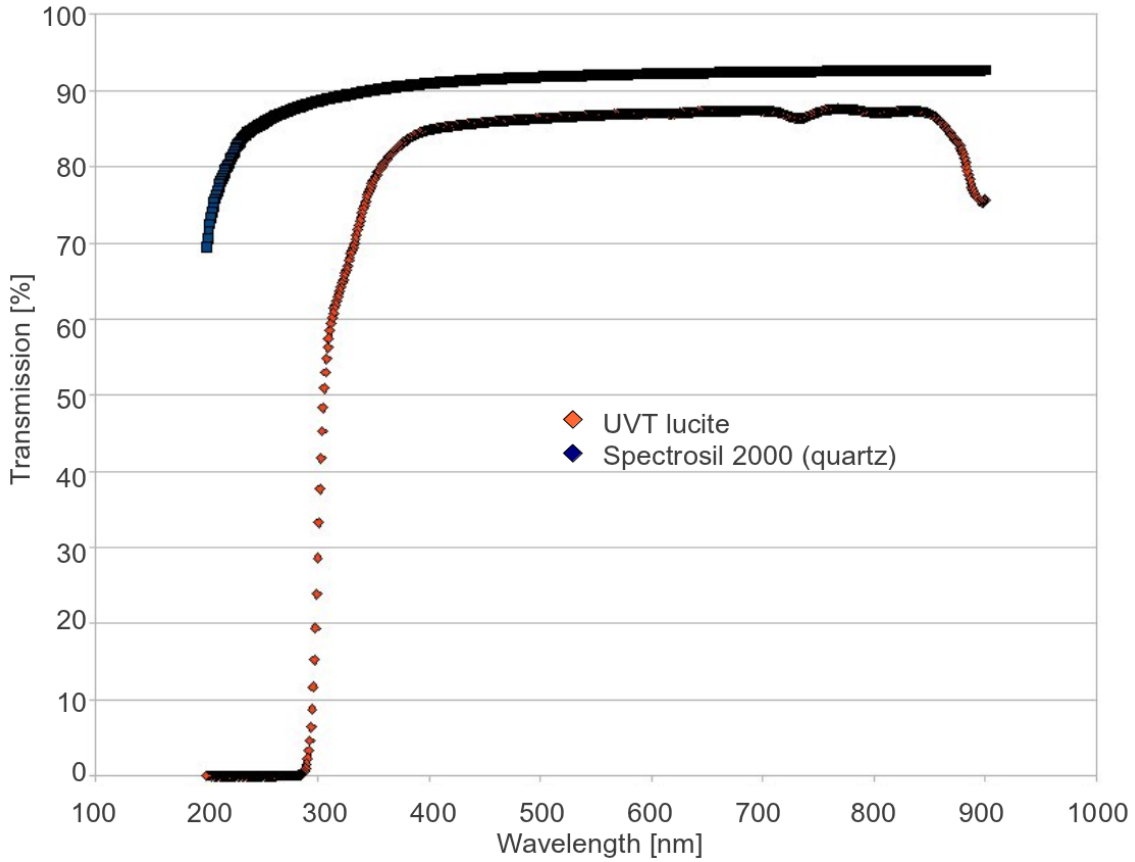

Figure 4.11: *Quartz and UVT lucite light transmission as a function of wavelength.*

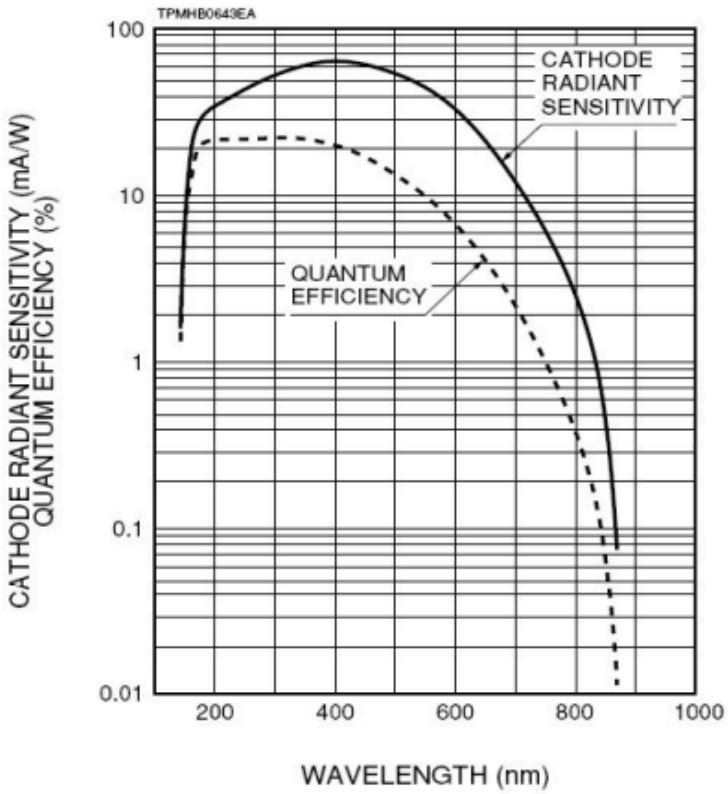

Figure 4.12: *Quantum efficiency of the R375 PMT.*

Figure 4.11 shows the quartz and UVT lucite light transmission for a range of wavelengths as measured at Virginia Tech. For UVT lucite the transmission falls rapidly after 300 nm. However, the quartz transmission begins falling at 200 nm. The quantum efficiency of the R375 PMT is show in Figure 4.12. The QE is still nonzero at 150 nm. This, and the good UV light transmission in quartz enables the detection of more UV photons.

The incident electron could vary about normal by $\sim 5^\circ$ without any loss of total internal reflection (TIR). For n=1.482, the critical angle for TIR is 42.4°. The angle at which Cerenkov light is emitted is defined to be,

$$\cos\theta_c(\lambda) = \frac{1}{\beta n(\lambda)} \ , \tag{4.1}$$

where n is the index of refraction as a function of wavelength of the fused silica and β is the relativisitic velocity of the incident particle. Using $n = 1.482$ (at 280 nm) and $\beta = 0.99999990$, $\theta_c = 47.56°$.

4.3 Simulation

The placement of the downstream luminosity monitors in the experimental hall was guided by analytical calculations and Geant3 simulations. The available radial position of the downstream luminosity monitors was between 0.5 and 0.8° and the final placement was 0.5°.

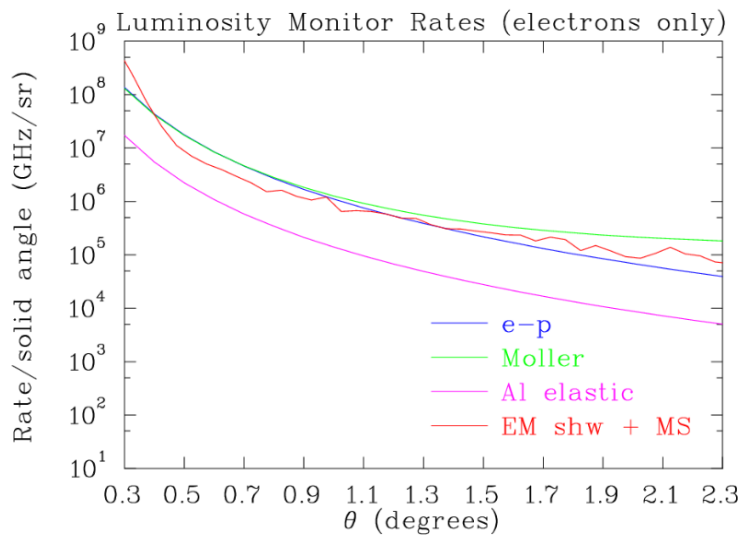

Figure 4.13: *Luminosity monitor rates as a function of scattering angle.*

Figure 4.13 shows the rate as a function of scattering angle for different sources of scattered electrons. $e-p$ is elastic scattering off of protons, *Møller* is elastic scattering off of electrons, *Al elastic* is elastic scattering off of the aluminum target windows, and *EM shw + MS* is electromagnetic showers plus multiple scattering interactions. The downstream luminosity monitors detect a mix of particles so they are sensitive to multiple interactions.

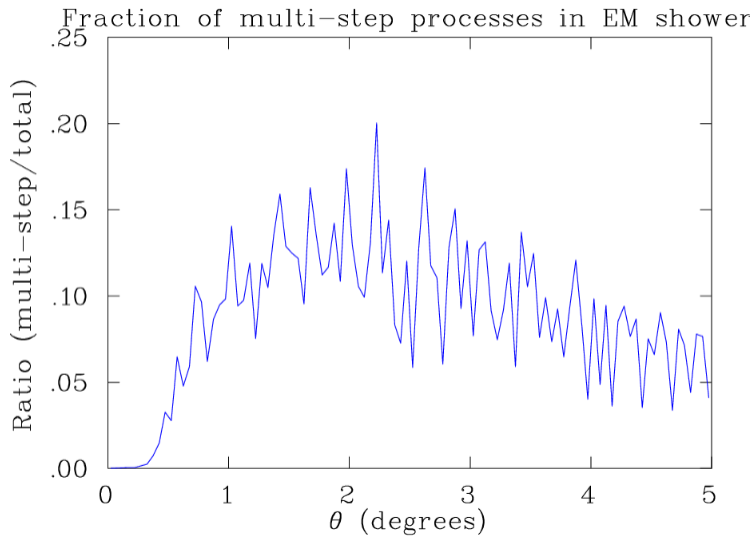

Figure 4.14: *Fraction of multiple scattering signal of total signal as a function of scattering angle for the range available to the downstream luminosity monitors.*

Figure 4.14 shows the fractional contribution due to multiple scattering to the total rate for a range of scattering angles. To accurately measure target density fluctuations the detectors need to be only sensitive to interactions that scale linearly with target length. Electromagnetic showering is a nonlinear process so a minimum contribution due to that interaction was desired for the upstream luminosity monitors.

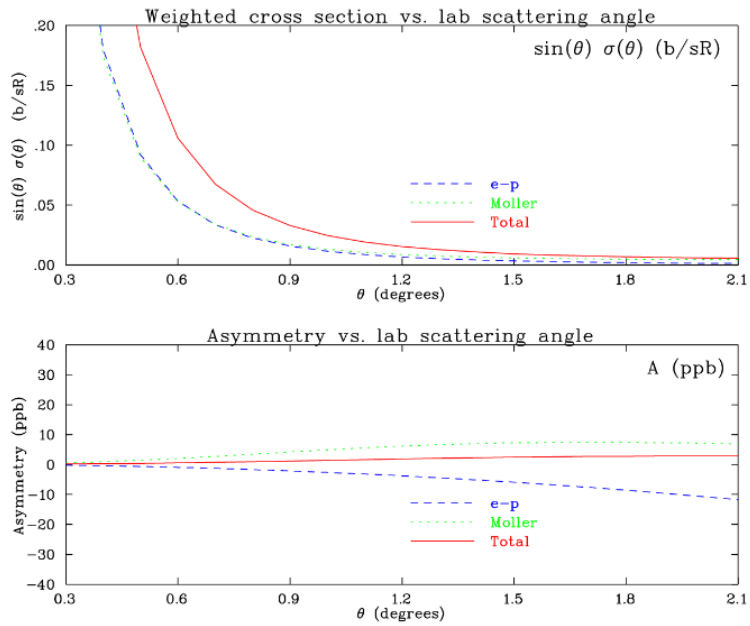

Figure 4.15: *Weighted cross section and asymmetry versus scattering angle.*

Figure 4.15 shows the cross section for $e-p$ and *Møller* scattering as a function of scattering angle. The cross section decreases rapidly as the scattering angle increases and the available range of 0.5 to 0.8° is in the volatile region. However, the asymmetry is a relatively stable ∼2 ppb, which is two orders of magnitude smaller than the expected asymmetry measured by the main detectors (∼200 ppb).

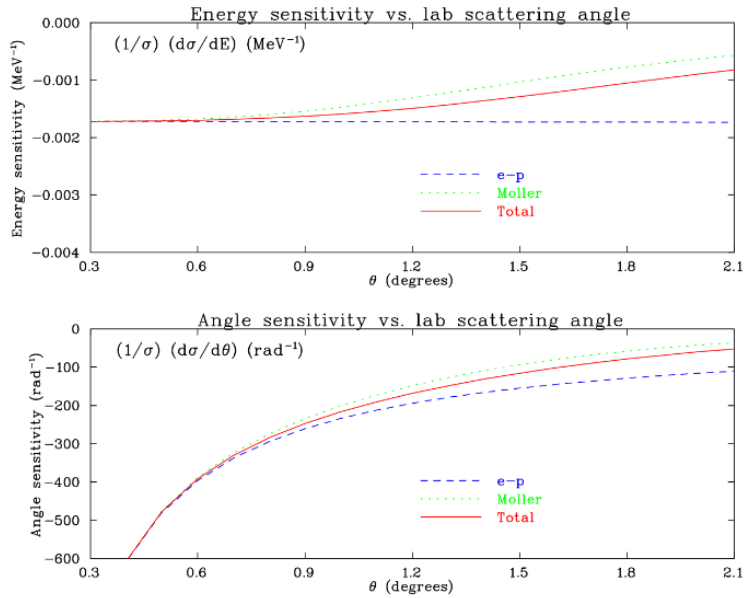

Figure 4.16: *Energy and angle sensitivity versus scattering angle.*

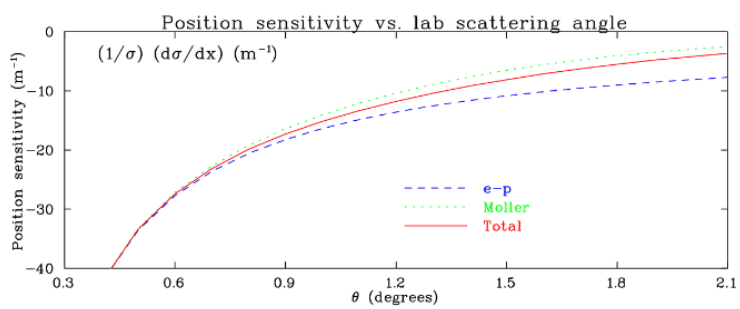

Figure 4.17: *Position sensitivity versus scattering angle.*

Figure 4.16 shows the sensitivity to energy and angle change as a function of scattering angle. The smaller the sensitivity the less impact nonzero energy or angle differences will have on the detectors. The sensitivities in Figure 4.16 are greater than those for the main detectors, which makes the luminosity monitors more sensitive to helicity correlated beam parameter changes. Thus, the luminosity monitors provide a good test of the regression procedure used to correct for helicity correlated beam parameters (see Section 5.3.1).

Table 4.2 gives parameters based three locations for the downstream luminosity monitors. The location of 0.5° was chosen as the final position.

Table 4.2: Estimated rate comparison of three locations for the downstream luminosity monitors.

Parameter	Location 1	Location 2	Location 3
scattering angle	$0.55 \pm 0.05°$	$0.65 \pm 0.05°$	$0.75 \pm 0.05°$
rate e-p elastics/detector	71 GHz	36 GHz	11 GHz
rate Møllers/detector	79 GHz	43 GHz	12 GHz
rate EM showers/detector	119 GHz	46 GHz	6 GHz
total rate/detector	269 GHz	125 GHz	29 GHz
typical photocathode current	11000 nA	5000 nA	1160 nA
multi-step target process fraction	2%	2%	1%
total dose during Qweak	4.8 Grad	2.3 Grad	0.5 Grad

While the placement of the downstream luminosity monitors was determined by Geant3 and analytical calculations, the final design of the luminosity monitors was heavily influenced by Geant4 simulation results. The simulations were used to determine the shape of the detectors and the materials used in their construction.

Included in the simulation:

- 1.165 GeV electron normal to surface of quartz
- DS:1.3 cm, US:2 cm thick quartz, n∼1.48
- 0.3 mm edge bevels
- light guide with 95% reflective surface
- PMT with quantum effiency curve applied to incident photons
- physics processes
  - Compton Scattering
  - Gamma Conversion
  - Photoelectric Effect
  - Multiple Scattering
  - Ionization
  - Bremsstrahlung
  - Annihilation
  - Cerenkov
  - Optical Absorption
  - Rayleigh Scattering
  - Decay

A factor of 1.6 increase in photons per event was expected when using a quartz window PMT over a borosilicate window PMT. Quartz is known to have better transmission in the UV

region than borosilicate.

The thickness of the quartz for the luminosity monitors was determined by simulation. In a simulation several thousand events were generated by passing a single electron through a piece of quartz multiple times.

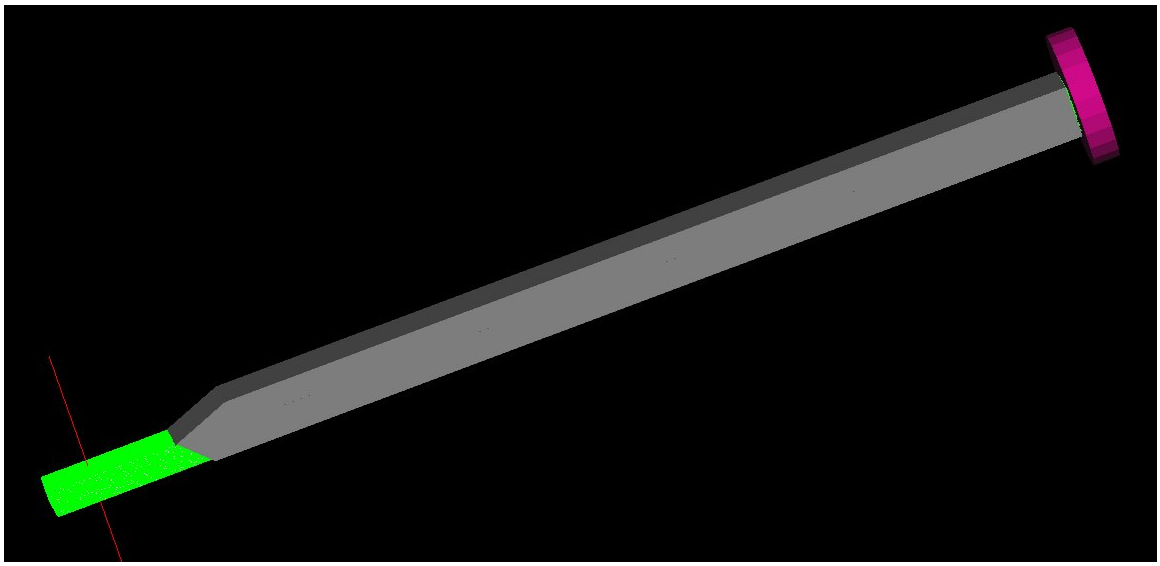

Figure 4.18: *Initial simulation of a downstream luminosity monitor. The relativistic incident electron is red, the quartz radiator is white but not visible because it is saturated with photons, the photons are green, the light guide is gray, and the PMT is magenta.*

For each incident electron the number of photoelectrons detected by the PMT would be recorded. From this collection of detected photoelectrons the mean and width of the distribution could be determined. As one increases the thickness of the quartz the mean and width of the distribution also increases. However, the width of the distribution increases more quickly. The number of photons emitted due to Cerenkov radiation increases linearly with material thickness but some intrinsically "noisy" processes, such as electromagnetic showers, increase exponentially. A compromise needed to be made between the number of photons detected and the width of the distribution and was determined by simulation.

Equation 4.2 describes the generation of Cerenkov light due to relativistic particles passing through matter,

$$\frac{d^2N}{dxd\lambda} = \frac{2\pi\alpha z^2}{\lambda^2}\left(1 - \frac{1}{\beta^2 n^2(\lambda)}\right) , \tag{4.2}$$

where N is the number of photons generated, x is the length of the interaction, λ is the wavelength of generated light, π is the usual constant, α is the fine-structure constant, z is the charge of the incident particle, β is the relativistic velocity of the incident particle, v/c, and $n(\lambda)$ is the index of refraction as a function of wavelength. The other dimensions of the luminosity monitor designs were largely determined from space constraints.

The expected number of photons from Cerenkov radiation for 1 cm thick quartz (no absorption, perfect internal reflectivity, etc.) according to Equation 4.2 is 410. This number was consistent with what was observed in simulation.

The simulation reliably predicted higher numbers of photoelectrons than was found in a similar experimental bench test. Some time was spent unsuccessfully trying to get the simulation and the experimental number of photoelectrons detected to agree. A ratio between the number of photoelectrons detected in two different simulations compared to a ratio of the same two configurations in experiment agreed better than the absolute number of photoelectrons detected. For example, the simulated over experimentally measured ratio of the number of photoelectrons escaping the flat surface of the quartz was 212/22=10 while the simulated over experimentally determined ratio number of photoelectrons that included the light guide was 92/7.4=12. These values are for the initial design of the downstream luminosity monitor using a quartz piece with dimensions 6x2x1 cm.

The disagreement was likely due to the complexity of simulating the optical properties of the photons. The reflectivity of the light guide as a function of wavelength was not known. The absolute polish of the quartz and some of the transmission properties used in the bench

tests were also unknowns. Despite these limitations, the luminosity monitors exceeded the requirements in the Qweak proposal.

4.4 Testing

4.4.1 Event Mode

An event mode test bed using cosmic rays was set up to characterize the light output of the luminosity monitors before they were installed at Jefferson Lab. The luminosity monitors were sandwiched between two scintillator paddles separated by 2 m, which created a "particle telescope". This setup reduced the incident cosmic ray radial spread to $\sim 8^\circ$ about normal. The scintillators and the luminosity monitor signals were recorded in a charge integrating ADC when the scintillators had a signal pulse above a set threshold.

A coincidence between two scintillators reduced the number of random triggers and slowed the data-rate to a manageable size. Varying the separation of the scintillator paddles to reduce the radial spread of the cosmics did not affect the number of photoelectrons detected.

To pick out the higher energy cosmic rays, 10 cm of lead was placed on top of the telescope. The addition of the lead hardened the cosmic ray energy spectrum, thus insuring that $\beta \approx 1$. However, the number of photoelectrons detected did not change.

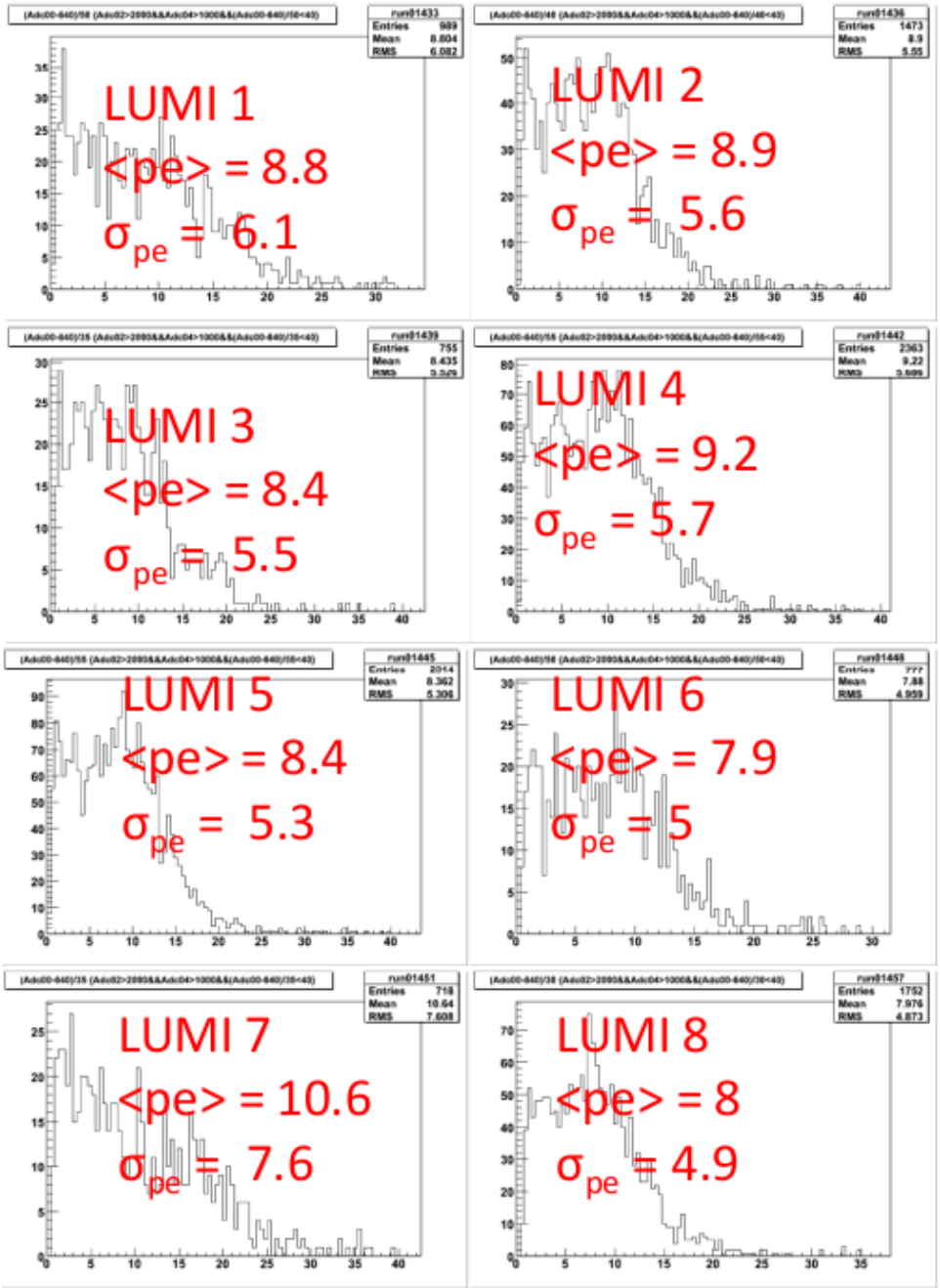

Figure 4.19: *Downstream luminosity monitor light yields in bench tests carried out at Virginia Tech. These are the photoelectron yields for the completed downstream luminosity monitors as they would be installed at Jefferson Lab.*

The average photoelectron yield for the downstream luminosity monitors was 8.9. A 2 cm thick lead preradiator was added in front of the downstream luminosity monitors for the actual experiment so the signal magnitude is approximately a factor of 8 higher.

A photoelectron yield measurement was done at Jefferson Lab during Qweak running. This measurement was performed using the main detector "event mode" electronics. These electronics include a charge to digital converter, which records the charge contained within a triggered pulse from the luminosity monitor. The threshold for data capture was approximately 1.5 photoelectrons and the timing was such that the detector self-triggered. The beam current was lowered to ∼100 pA so individual pulses could be distinguished.

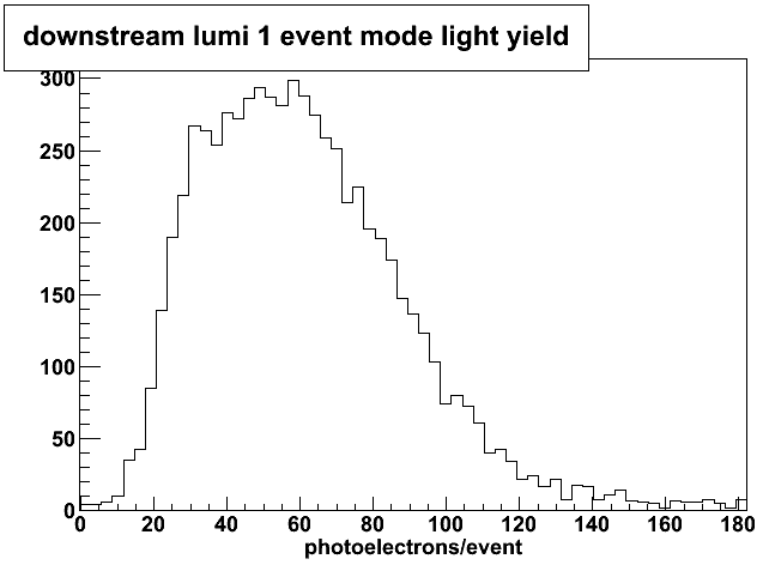

Figure 4.20: *Downstream luminosity monitor light yields at Jefferson Lab. The mean of this distribution is ∼60.*

The mean number of photoelectrons observed in this test was about 60 (Figure 4.20), which is in reasonable agreement with the expectation of ∼9 x 8 = 72, given the uncertainties of the gain of the PMTs in this measurement.

4.4.2 Integration Mode

A integration mode test bed was set up to characterize the linearity of the Hamamatsu R375 PMT. The R375 was required to measure the same asymmetry at the operating DC cathode currents of the Qweak experiment or potentially large corrections would need to be applied. Studies of the linearity of the PMT were made using a setup with DC and AC light emitting diodes (LEDs), a picoammeter to measure the photodetector cathode current, and a voltage to frequency converter (V/F) to monitor the photodetector AC response as the DC light level was varied. Figure 4.21 shows a schematic of the setup.

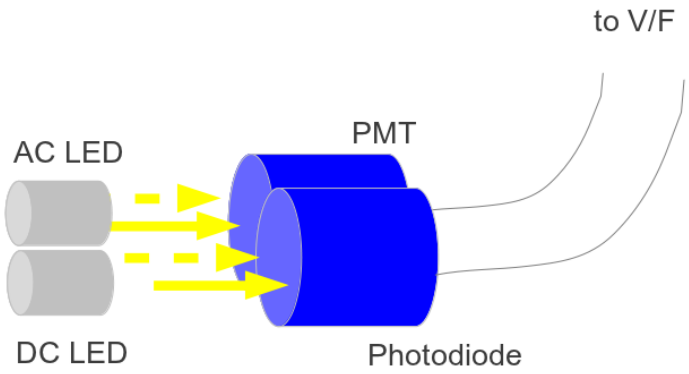

Figure 4.21: *Setup schematic of the linearity test.*

The AC and DC LEDs were positioned so that a Hamamatsu R2046PT photodiode and a Hamamatsu R375 PMT were both illuminated equally. Photodiodes have been measured to be linear beyond the Qweak PMT requirements so the photodiode was used to normalize out any fluctuations of the LEDs.

The linearity of the PMT was measured at a flip rate of 30 Hz. One LED was on constantly (DC) and one LED was turned on and off (AC). The current in the DC LED was varied to simulate different beam currents the PMTs would experience at Jefferson Lab. The AC

LED was kept at the same current. An asymmetry was formed,

$$Asymmetry = \frac{DC + AC - DC}{DC + AC + DC} = \frac{AC}{2DC + AC} \ . \tag{4.3}$$

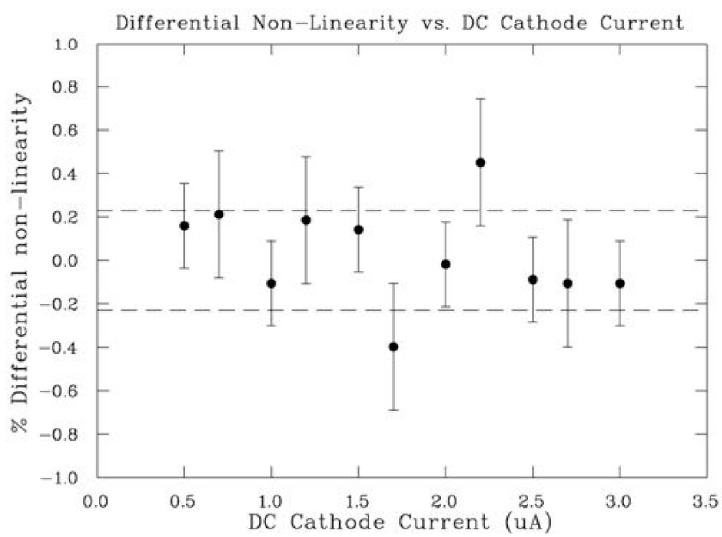

Figure 4.22: *Differential nonlinearity of an R375 PMT.*

The AC and DC current in the PMT was recorded for each DC LED setting. Each DC setting should measure the same AC value if the detector is linear. Under these conditions the observed differential nonlinearity ($< 0.2\%$) was below the required 1% over the Qweak operating range as seen in Figure 4.22.

The upstream luminosity monitor cathode current was $\sim 0.2\mu$A and there was very little variation between the detectors. Their preamplifiers were set to 25 MΩ gain. The highest allowed cathode current for a downstream luminosity monitor was $\sim 1\mu$A. This value varied by as much as factor of 3 for the other downstream luminosity monitors due to the angle of the incident electron beam and the strength of the bending magnet. The downstream

luminosity monitor's preamplifiers were set to 4 MΩ gain.

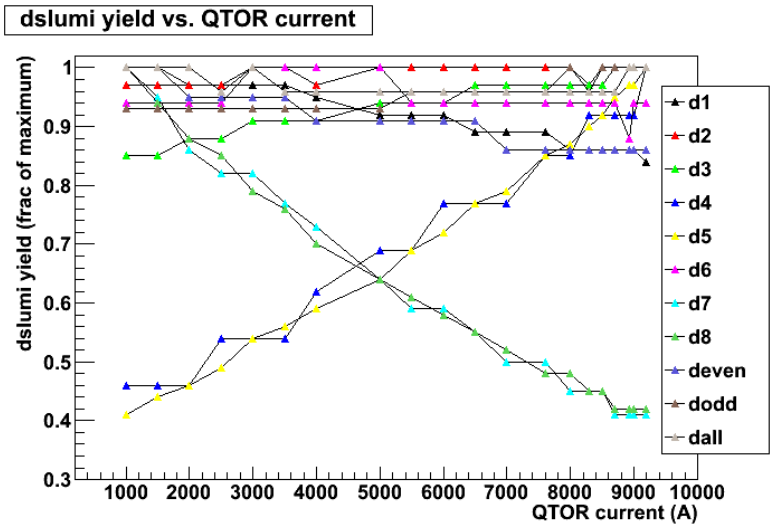

Figure 4.23: *QTOR electron beam steering observed by the downstream luminosity monitors. A low energy electron flux is steered from beam lower left at QTOR=0 A to beam upper right when QTOR is at full power (QTOR=8920 A).*

Figure 4.23 shows the signal variation as a function of bending magnet current. Clearly, the bending magnet had a large effect on the flux through the downstream luminosity monitor region. Given a perfectly aligned magnet, one would expect no residual steering effects for electrons travelling through the magnet's center. The Qweak bending magnet was not perfectly aligned so some beam steering was observed.

4.5 Prototype Luminosity Monitor and Target Density Fluctuation Frequency Dependence Study

4.5.1 Introduction

In June of 2008 a parasitic experiment was set up in Hall C of Jefferson Lab during the Gep experiment. The goal of this test was to determine the dependence of target density fluctuations on data-taking frequency and test a prototype downstream luminosity monitor.

The statistical width of an individual luminosity monitor on the LH_2 target used for this test can be approximated by the Equation 4.4. Electronic noise and noise due to beam parameter correlations have been neglected in this simple model,

$$\Gamma_{stat} = \sqrt{\Gamma^2_{counting} + \Gamma^2_{target}} \ . \tag{4.4}$$

The hypothesis was that at higher data-taking rates the contribution to the width of the measured asymmetry due to target density fluctuations will decrease. This was an important hypothesis to test at the time because the Qweak experiment was planned to be run at a much higher data-taking rate (1 kHz) than previous parity experiments at Jefferson Lab (30 Hz). For that to be an optimal strategy, it was important to demonstrate, in advance, that the relative contribution of any target density fluctuations decreased with increasing data-taking frequency. The target used in this test was not designed to have intrinsically small target density fluctuations like the Qweak target. Thus, this was a good target to check the frequency dependence of the fluctuations because they were easily measured. Details and results of this study are presented here.

4.5.2 Experimental Method

Six luminosity monitors were used in this study. All used Hamamatsu R375 quartz window PMTs and were positioned at a scattering angle of 0.6°. Details of the luminosity monitors and targets used in this study are given in Tables 4.3 and 4.4.

Table 4.3: Devices used in June 2008 beam test

Name	Type	Gain	Radiator	Preamp
LUMI 1	G0	20	7.62x3.56x3.56 cm, quartz	Hamamatsu
LUMI 2	Qweak	1	4.5x4x1.3 cm, lucite	TRIUMF I/V
LUMI 3	G0	20	7.62x3.56x3.56 cm, quartz	Hamamatsu
LUMI 4	G0	20	7.62x3.56x3.56 cm, quartz	Hamamatsu
LUMI 5	G0	20	no radiator	Hamamatsu
LUMI 6	G0	20	no radiator	TRIUMF I/V (clean power)

A current was drawn from the PMTs and sent to a preamp for conversion to voltage. The power supply that powered the preamp for LUMI 6 was of high quality and not the standard "wall wart" used for the other luminosity monitors.

Table 4.4: Targets used in June 2008 beam test

Target	Radiation Length	Density	Data-rate	Current Values
4.4 mm carbon	2.1% X_0	0.88 g/cm^2	30, 250 Hz	10 - 80 μA
20 cm LH_2	2.3% X_0	1.4 g/cm^2	30, 250, 1000 Hz	10 - 80 μA

The carbon target was used as the "control" because it was not susceptible to target density fluctuations. This allowed the electronic noise and beam parameter correlation noise to be characterized.

4.5.2.1 Linephase Contribution

AC power phase can contribute to the measurement in a number of ways. For example, unclean AC to DC power conversion for the preamps affected the test presented here. This effect artificially increased the uncertainty of our measurements.

Most of the AC to DC adapters used to power the preamps were low quality. This caused the AC oscillations to create an AC ripple on top of the otherwise constant DC power. In typical applications of AC to DC converters this would not be an issue. However, because of the sensitivity of the electronics and the data-taking frequency of the tests our data was adversely affected.

The typical Jefferson Lab data-taking frequency is 30 Hz. This rate effectively averages out the contributions due to the AC linephase. However, this test required different data-taking rates so a way to remove the linephase contributions was essential. A linephase monitor was implemented by Paul King to sample the linephase and determine correlations. Using this monitor, one could measure the linephase contribution and remove it.

Figure 4.24 shows LUMI 1's signal at 250 Hz data-rate plotted versus a linephase monitor and fit with a polynominal of order nine. A clear correlation is visible. A similar correlation was observed at 1000 Hz data-taking rate but there was absent in the 30 Hz data-taking rate dataset.

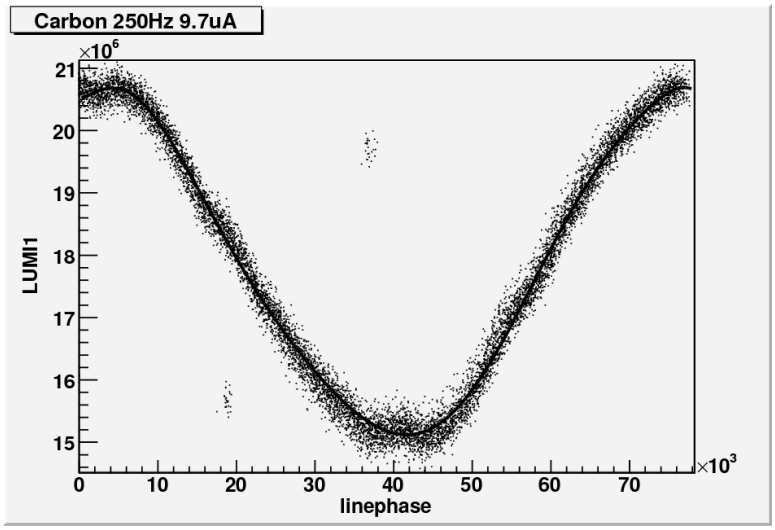

Figure 4.24: *Linephase correlation with LUMI 1 signal. Arbitrary units.*

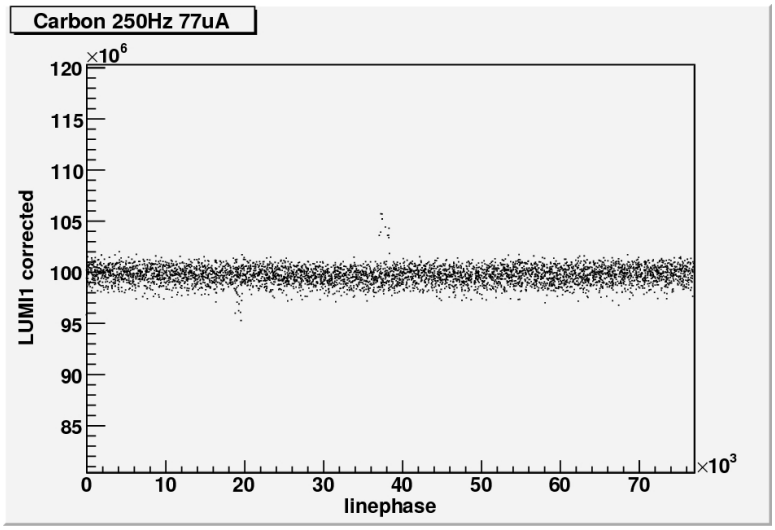

Figure 4.25: *Linephase correlation with LUMI 1 signal after linephase correction was applied. Arbitrary units.*

Figure 4.25 shows LUMI 1's signal as a function of linephase after the linephase correction was applied. One can see very little correlation.

AC power correlations were observed in the pedestals of the luminosity monitors. If one

removes the linephase dependence of the pedestal one would expect the beam on signal to be linephase independent. This assumes that there are no other linephase dependent variables. Removing the linephase dependence of the luminosity monitor pedestals did not remove the *beam on* linephase dependence.

One would naively assume that the only difference between the luminosity monitor pedestal (*beam off*) signals and the *beam on* signals was the beam. However, the beam charge monitor (BCM) and beam position monitors (BPM) showed no visible linephase dependence. So, the linephase dependence of the luminosity monitors was changing in an unexpected way. One possible explanation is that the response to the linephase changes from *beam on* to *beam off* because the load on the preamp changes.

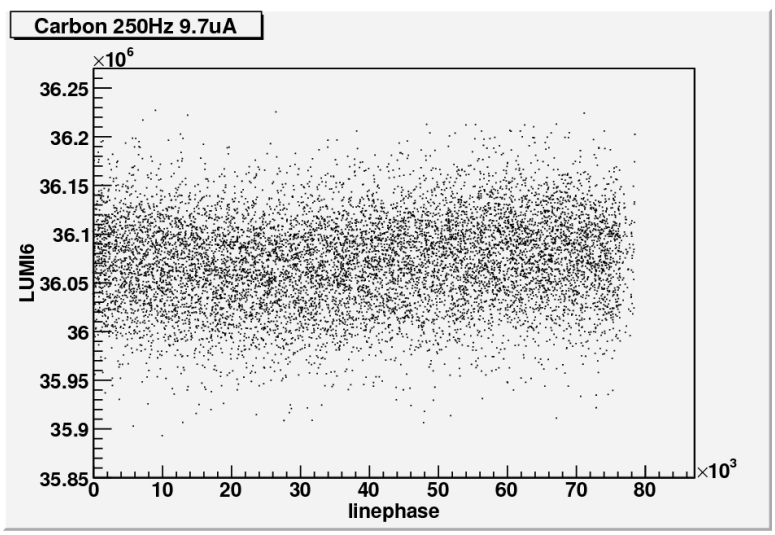

Figure 4.26: *Linephase correlation with LUMI 6 signal. Because of the isolated preamp power supply, no linephase corrections were needed to remove a correlation. Arbitraty units.*

The LUMI 6 preamp was in the cage upstairs and was connected to the well-isolated power supply. Because of this, LUMI 6 showed relatively little linephase dependence compared to the others (see Figure 4.26).

4.5.2.2 Normalizing the Luminosity Monitor Signals

For a linear luminosity monitor and a stable target one would expect the normalized signal, or yield, to be independent of the beam current. The signal in the luminosity monitors increases as the beam current increases so for a linear system the luminosity monitor signal divided by the beam current should be constant for the range of beam current being tested. The relation is given in Equation 4.5,

$$Yield = \frac{S_{lumi}}{S_{beam}} = constant \ , \tag{4.5}$$

where S is the unnormalized signal from the luminosity monitor or the beam current monitor.

For the carbon target Equation 4.5 was true but for the LH_2 target the yield dropped by 20% at the highest beam current for all of the luminosity monitors at all data-taking frequencies. This can be interpreted as the interaction length of the target decreased by 20% when the beam current was increased from 10 to 80 μA. The LH_2 target used in this study was known to be subject to boiling so this result was not unexpected.

4.5.2.3 Extracting Asymmetry Widths

An asymmetry was generated from the yields using randomly selected helicity pairs according to the equation,

$$Asymmetry = \frac{Y_+ - Y_-}{Y_+ + Y_-} \ . \tag{4.6}$$

A random asymmetry generator was used because only the width of the asymmetry was interesting for this test, not the central value.

The model used for the carbon asymmetry width was,

$$\Gamma^2_{carbon} = \left(\frac{A}{\sqrt{I}}\right)^2 + \left(\frac{B}{I}\right)^2 + C^2 \,, \tag{4.7}$$

where I is the beam current, the term involving A parameterizes the counting statistics contribution, the term involving B parameterizes electronic noise contribution, and C parameterizes the contribution due to the correlations with beam position monitors.

An example of the fit quality this model produces is shown in Figure 4.27.

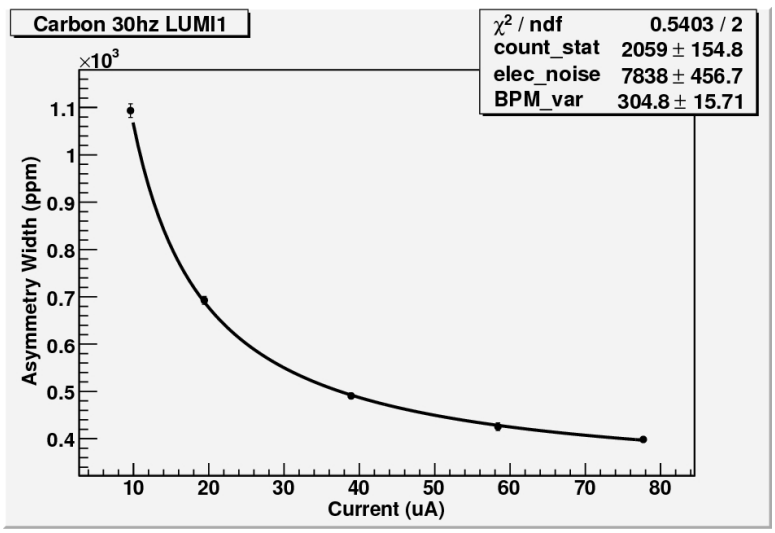

Figure 4.27: *Example of the quality of the fit to the asymmetry width curve on the carbon target.*

Table 4.5: Width contribution of noise sources

Contribution	Constant	Contribution at 80 μA [ppm]
Counting	2059	230
Elec. Noise	7838	98
BPM Corr.	304.8	304.8

Table 4.5 shows the contributions extracted from the fit in Figure 4.27. The fit values of the electronic noise and beam parameter contributions can be independently determined from the data. Both the electronic noise and beam parameter contributions determined from the data are in good agreement with the fit values.

Table 4.6: Comparison of extracted and fit values

	correlated parameter width noise:		elec. noise widths at 80 μA:	
30 Hz carbon	Data	Fit	Data	Fit
LUMI 1	314	305 ± 16	63	98 ± 6
LUMI 2	244	0.0235 ± 192	552	423 ± 6
LUMI 3	447	441 ± 17	66	99 ± 8
LUMI 4	363	345 ± 17	64	103 ± 7
LUMI 5	662	656 ± 32	186	286 ± 10
LUMI 6	630	681 ± 21	14	92 ± 14

To extract the beam parameter correlation widths from the data one must determine the correlation of the asymmetry to the beam position monitor. This slope is then multiplied by the width of the beam position monitor. The result gives a good estimate of the beam parameter correlation contribution to the width. Ideally, one would use a matrix of correlations for all beam parameters but this capability was not available for this analysis.

On the carbon target as the current increased the total asymmetry width decreased. This indicated that the total asymmetry width was dominated by counting statistics (see Figure 4.28). However, the opposite is true for the LH_2 target. As the current increased the total asymmetry width also increased (see Figure 4.29). This indicated that the total asymmetry width was dominated by target density fluctuations.

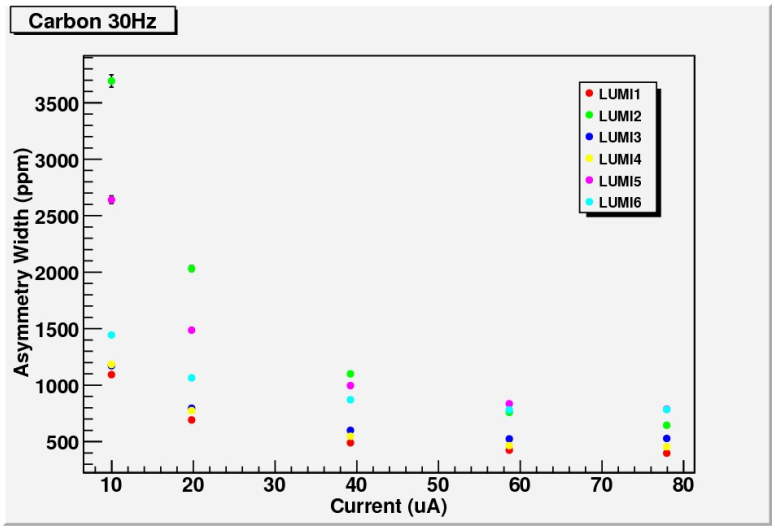

Figure 4.28: *Asymmetry width on the carbon target.*

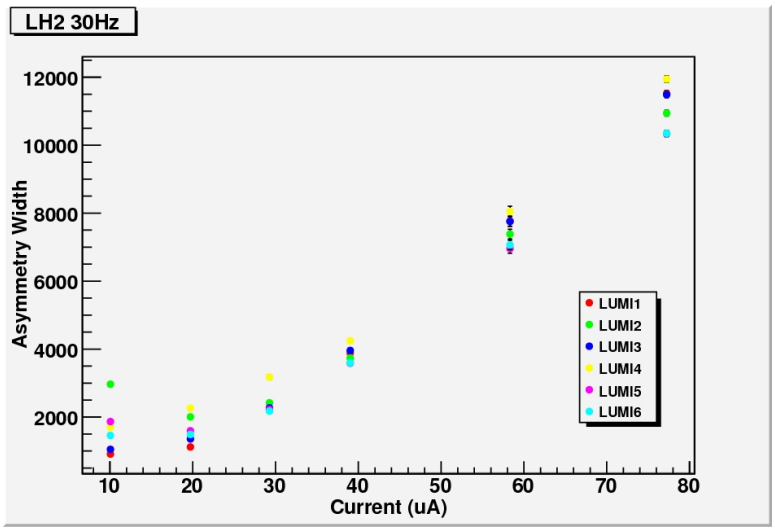

Figure 4.29: *Asymmetry width on the LH_2 target. Contrary to the asymmetry width on the carbon target this width increases as the current increases.*

The model for the LH_2 target asymmetry width is given in Equation 4.8 and is a modified version of the carbon model. It includes an additional term for contributions due to target density fluctuations and the ratio $\frac{Y_{LH_2}}{Y_C}$, which normalizes the yields to be equal on both

targets at 80 μA.

$$\Gamma^2_{LH_2} = \left(\frac{A}{\sqrt{\frac{Y_{LH_2}}{Y_C}I}}\right)^2 + \left(\frac{B}{\frac{Y_{LH_2}}{Y_C}I}\right)^2 + C^2 + \Gamma^2_{target} \tag{4.8}$$

Using Equation 4.8, one can extract the target density fluctuation, or "boiling", contributions as a function of current. One expects the contribution to increase as the current increases, and, as seen in Figure 4.30, that is the case. Similar results were seen for the other data-taking rates.

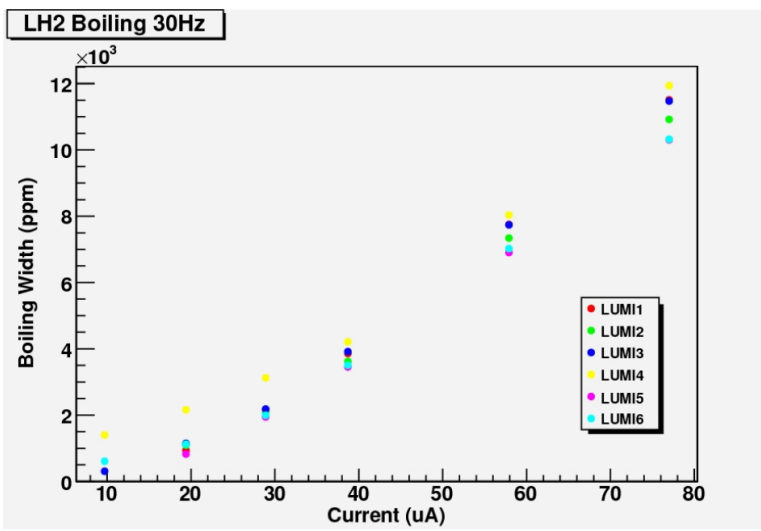

Figure 4.30: *Extracted boiling widths as a function of beam current on LH_2 for the 30 Hz data-taking rate.*

4.5.3 Results

If Γ_{target} stays constant or decreases with frequency the relative contribution of the target boiling term is reduced by going to higher data-taking frequencies, i.e. increase $\Gamma_{counting}$ (see Equation 4.4). Figure 4.31 shows the asymmetry width contribution due to boiling versus

data-taking rate.

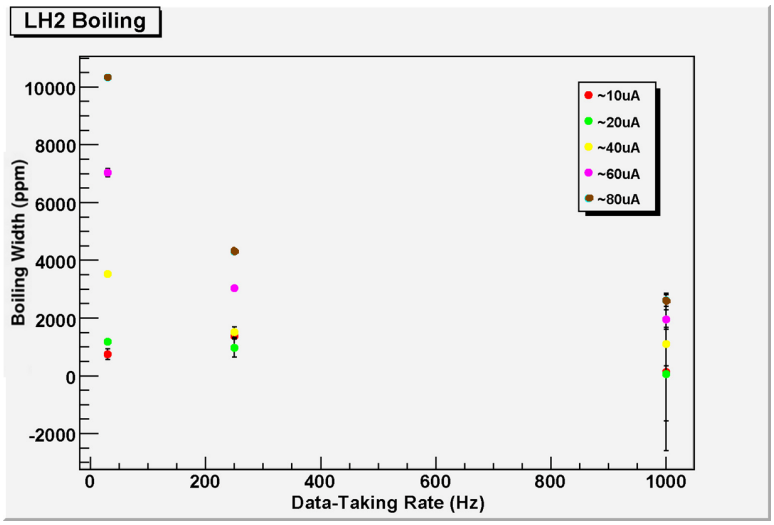

Figure 4.31: *Boiling width dependence on data-taking rate.*

The data here indicate that the boiling term drops with frequency as,

$$\Gamma_{target} = \Gamma_{30Hz} \left(\frac{30Hz}{f} \right)^{0.4} . \tag{4.9}$$

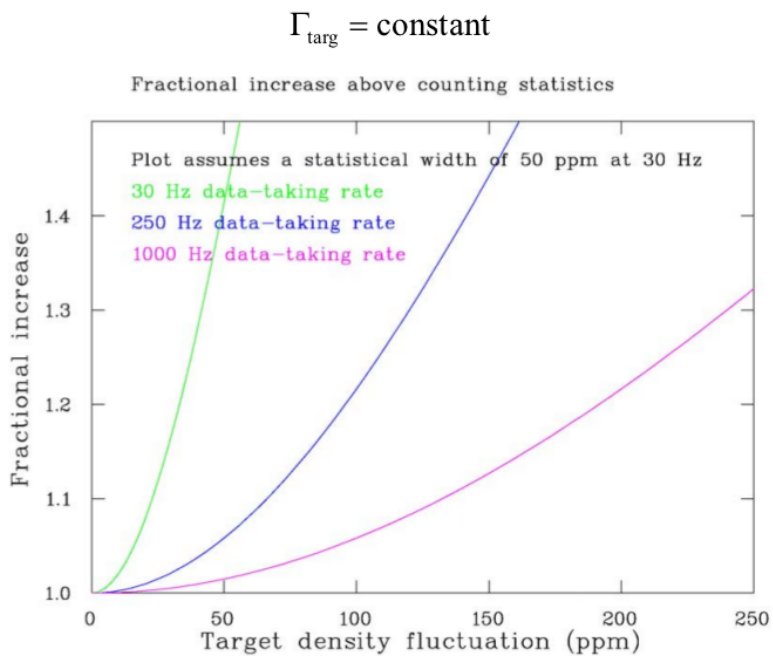

Figure 4.32: *Fractional increase of asymmetry width above counting statistics assuming the contribution due to target density fluctuations remains constant for each data-taking frequency.*

$$\Gamma_{\text{targ}} = \Gamma_{30\,\text{Hz}}\left(\frac{30\ \text{Hz}}{\text{f}}\right)^{0.4}$$

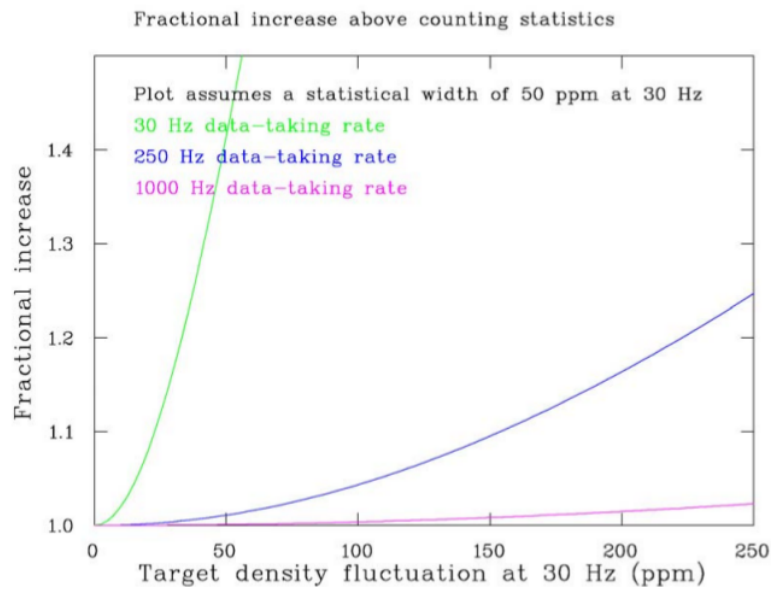

Figure 4.33: *Fractional increase of asymmetry width above counting with observed frequency to boiling of* $\Gamma_{target} = \Gamma_{30Hz}\left(\frac{30Hz}{f}\right)^{0.4}$.

One can see from Figures 4.32 and 4.33 that as long as the target density fluctuations remain constant or decrease as a function of data-taking frequency the relative contribution to the statistical error will decrease as frequency increases.

4.5.4 Conclusion

Increasing the data-taking frequency decreases the target density fluctuation noise contribution according to our empirically determined equation $\Gamma_{target} = \Gamma_{30Hz}\left(\frac{30Hz}{f}\right)^{0.4}$. A 20% drop in luminosity indicates the target was suffering from a large target density reduction at 80 μA. Applying this model to other targets should be done carefully because it is not clear the model will hold under conditions in which the target is more stable. This study helped

motivate the 960 Hz data-taking rate for Qweak.

4.6 Performance

Qweak is measuring an asymmetry of order 200 ppb so to be sensitive to this small of an asymmetry one must reduce all contributions of noise that may affect the detector widths. Approximately every 1 ms the signal is integrated, thereby reducing noise from target density fluctuations and long term drifts in the detector signals. Noise on the order of 100 μV on a typical 5 V signal is comparable to the 20 ppm counting statistical width of a luminosity monitor.

As explained above, longevity of the luminosity monitors was a major concern. Many precautions were taken to reduce the exposure of the detectors to radiation. Previous experiments observed a white powder form on the exposed metal of highly dosed detectors in similar radiation conditions seen by the Qweak luminosity monitors [42]. It is believed that this powder is caused by nitric acid corroding the metal. This acid is formed by scattered electrons interacting with the moisture in the air. Nitrogen was used to purge the active elements of the Qweak luminosity monitors to encourage a nonvolatile environment. Implementing a nitrogen purge likely increased the longevity of the luminosity monitors. After 1/8 of their total 4.8 Grad expected dose, no evidence of degradation of the nitrogen flushed parts was observed. Parts that were not flushed with nitrogen showed clear evidence of radiation damage.

After 1/10 of their total expected dose some of the luminosity monitors started showing strange pedestal behavior. Upon inspection, the insulating material in the signal (BNC) connector had turned to paste. Radiation damage had turned the insulator into a dielectric, which created a battery between the center pin and the shielding of the BNC connectors. The

bases were constructed by a local vendor and several attempts to learn the manufacturer of the BNC connectors were unsuccessful. The bad connectors were replaced with the common KINGS BNC connectors with Teflon insulation.

Initial operation of the downstream luminosity monitors was plagued by noise from unknown sources. A Fourier analysis of the detector signal revealed a number of peaks above the noise floor. These included the 60 Hz linephase, 60 Hz harmonics, and a 600 Hz peak. The linephase and harmonics were easily suppressed by electrically isolating the luminosity monitor housing from the beam pipe using insulating inserts. However, the noise at 600 Hz was intermittent and isolating the cause proved difficult.

Eventually, the source was found to be a vacuum pump near the downstream luminosity monitors, which was causing a vibration in the detectors. In Figure 4.34 time is on the X axis and luminosity monitor signal is on the Y axis. The turbo pump was turned on halfway through each plot.

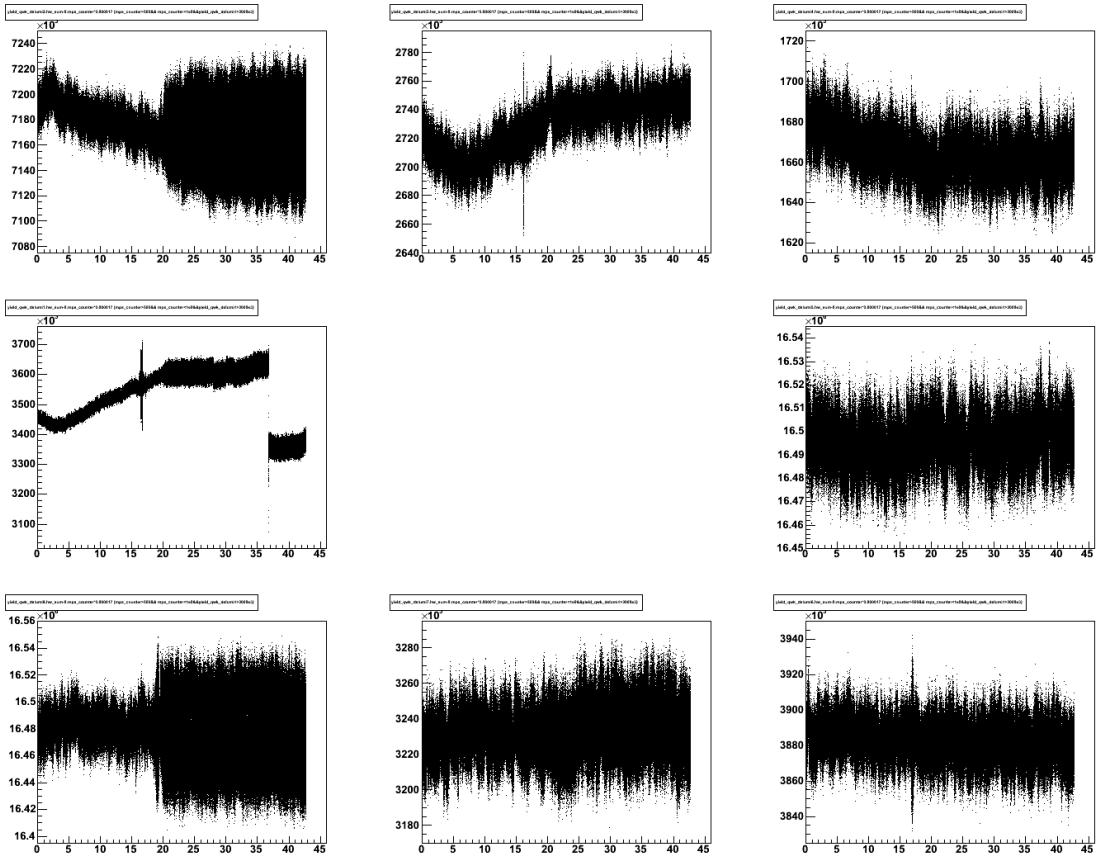

Figure 4.34: *Effect of turbo pump vibration on luminosity monitor signals. Clockwise from middle left is dslumi1, dslumi2, dslumi3, dslumi4, dslumi5, dslumi6, dslumi7, and dslumi8.*

Notice the width of the signal increases dramatically in the plots on the left. The middle left plot drop in signal is due to a bad connection that was fixed before data-taking began. The vibration effect was not limited to the dslumi1, dslumi2, and dslumi8 as this plot implies but affected all downstream luminosity monitors at some point.

The magnitude of the noise was dependent on the torque applied to the set screws that held the detectors in place. These issues were resolved by redesigning the mounting hardware to be acoustically as well as electrically isolating.

The luminosity monitors are extremely sensitive to beam position and angle. This has helped benchmark the regression scheme for the less sensitive main detectors. The deliberate 4 mm motion of the raster causes a 30% modulation of the signal in the downstream luminosity monitors (see Figure 4.35).

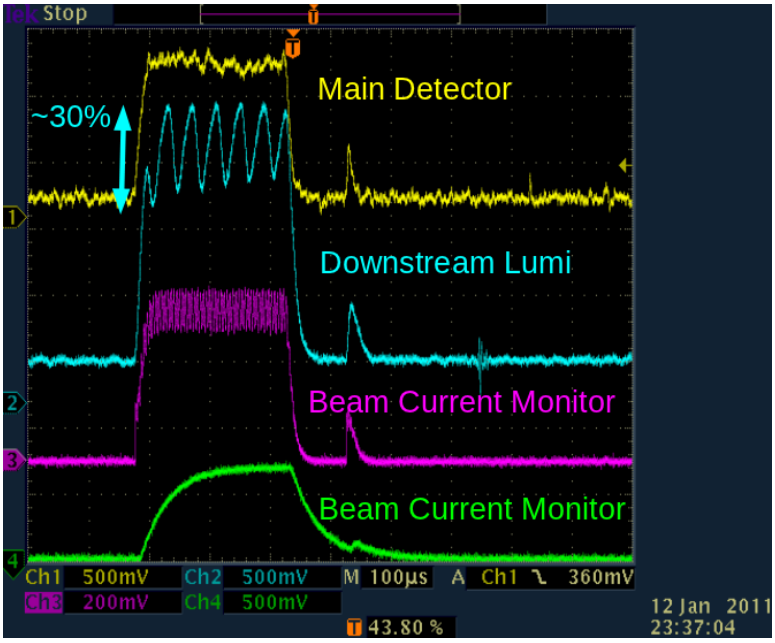

Figure 4.35: *Raster modulation of BCM, MD, and downstream luminosity monitor signals. The intrinsic width (ignoring the raster modulation) of the downstream luminosity monitor is smaller than the main detector, however, the main detector asymmetry width was approximately the same as the luminosity monitor asymmetry width. The green beam current monitor bandwidth setting had not been optimized when this image was recorded. The lagging short pulse is an accelerator technique to allow the operators to properly direct each end station's beam.*

One can take advantage of the azimuthal symmetry of the detectors by averaging their signals. Averaging over the eight downstream luminosity monitors lessens the raster modulation effect and reduces the sensitivity to beam parameters. The averaged downstream luminosity

monitor asymmetry width before regression was ∼200 ppm and after regression the width was as small as ∼180 ppm. Regression's effect on individual detectors was more pronounced.

Regression is a technique used to remove correlations between several parameters and is ideally suited to remove helicity correlated beam parameter effects from the Qweak detectors. A more detailed treatment of regression can be found in Section 5.3.1.

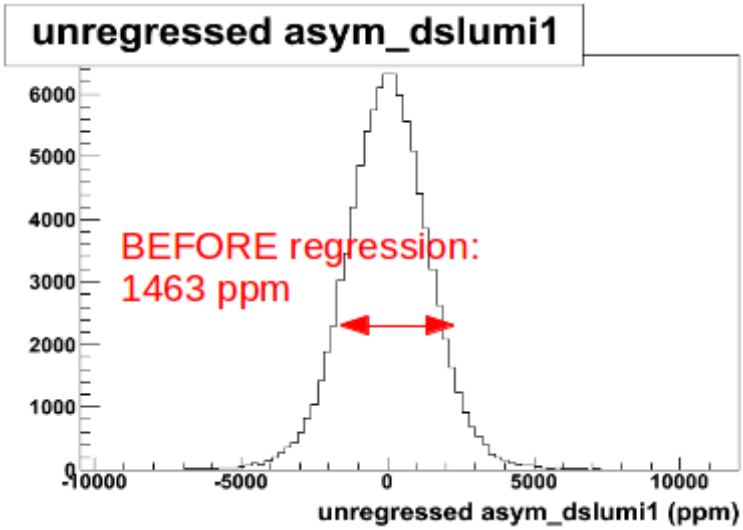

Figure 4.36: *Downstream luminosity monitor 1 asymmetry width before regression.*

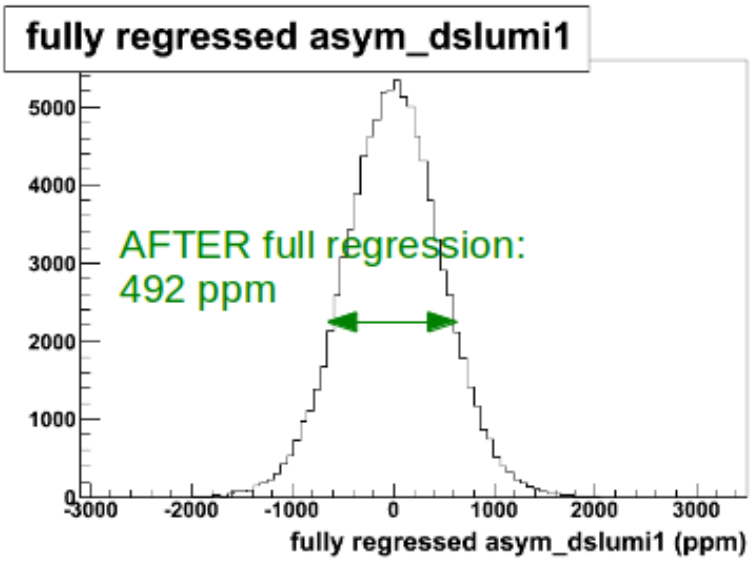

Figure 4.37: *Downstream luminosity monitor 1 asymmetry width after regression.*

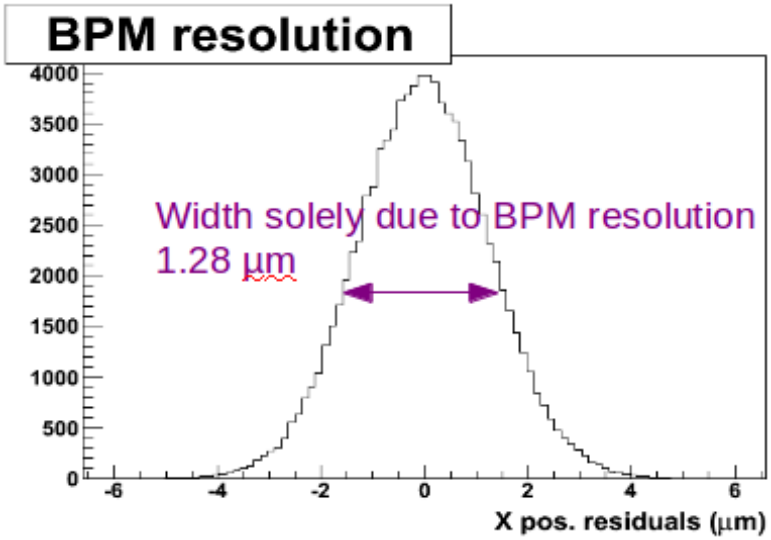

Figure 4.38: *Intrinsic BPM resolution calculated from residuals.*

The asymmetry width of one downstream luminosity monitor before regression (Figure 4.36) is greatly reduced by regression (see Figure 4.37). The asymmetry width of a single downstream luminosity monitor after regression can largely be accounted for by the intrinsic BPM

resolution. For this case, the sensitivity to an X BPM was 234700 ppm/mm and the resolution was ∼1.3 μm. This gives a contribution to the width of the detector from the BPM of 305 ppm. The total width was 492 ppm.

The upstream luminosity monitors were designed to monitor the target density fluctuations but the Qweak LH_2 target was largely immune to this type of noise. Instead, the luminosity monitors have mainly played a "canary" role for Qweak. Given the greater flux and the larger sensitivity to helicity correlated beam parameters, symptoms of poor quality beam are more quickly evident in the luminosity monitors than in the main detectors.

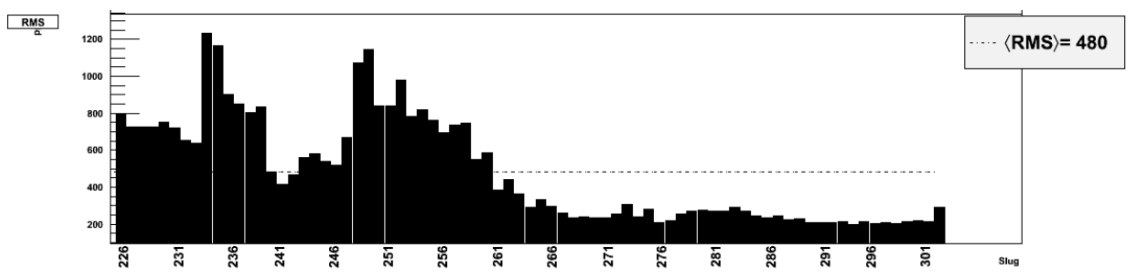

Figure 4.39: *Upstream luminosity monitor asymmetry widths (in ppm). An increase in the width of the upstream luminosity monitors was correlated to an increase in detected background asymmetry width.*

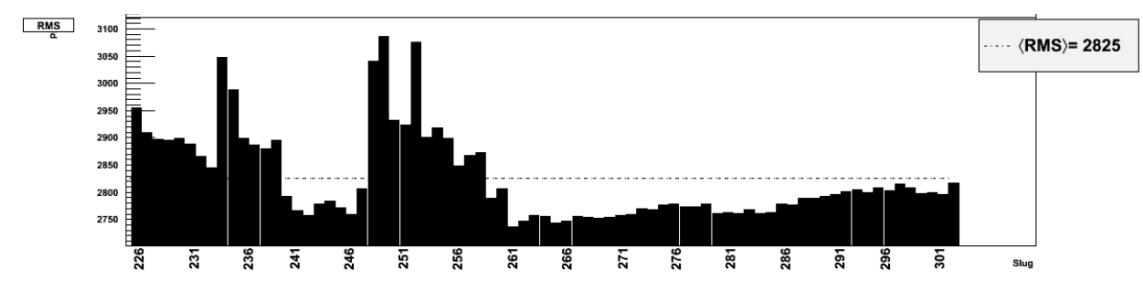

Figure 4.40: *pmtltg background detector asymmetry widths (in ppm).*

As one can see from Figures 4.39 and 4.40 the width of the measured upstream luminosity

monitor was correlated to large asymmetry widths in the *pmtltg* background detector. *pmtltg* is located just a few feet from the main detectors, so large asymmetry widths are concerning. Some of the signal it detects may be present in the main detectors, which could lead to a false asymmetry.

The actual correlation between beamline background and the signals in the various background and lumi detectors was extensively studied near the end of the run using insertable tungsten shutters to block two holes in the first collimator. These studies will be used to determine how much of the signal detected by the background detectors may have been present in the main detectors. The upstream luminosity monitor will serve as a precise continuous monitor of this background and will likely be important as the analysis of the full data set proceeds.

Chapter 5

Elastic Electron-Proton Analysis

Analysis of the Qweak data has been split into three sections, each with increasing precision on the extracted value of Q_W^p of 25%, 8%, and 4%. The analysis presented here is of the first dataset or the 25% measurement also called Wien 0.

The corrections presented here are sufficient for this dataset because the statistical uncertainty dominates the error budget. More work must be done for the corrections for the 8% and 4% extractions of Q_W^p.

Also, a blinding factor has been applied to this dataset to remove bias in the way corrections are applied. The blinding factor is a number between ±60 ppb added to the measured asymmetry. There is a firm prediction of the extracted elastic asymmetry from the Standard Model of -230 ppb. If there were no blinding factor, deviations in the measured asymmetry from the Standard Model prediction could be introduced or removed subconsciously by the analysis team. The blinding factor prevents this bias from entering the analysis.

For this analysis the blinding factor will be considered an added source of random noise of ∼68 ppb, which contributes to the final uncertainty of the extracted asymmetry. This value

is obtained by taking twice the RMS of a 120 ppb (±60 ppb) wide flat distribution.

5.1 Q^2

A precise determination of the four momentum transfer is not necessary for this analysis. However, the final 4% measurement of Q_W^p will require a knowledge of Q^2 with an uncertainty of 0.5%.

The elastic asymmetry is a function of Q^2 so a precise determination of the four momentum will reduce the error on the extraction of Q_W^p. Equation 5.1 shows this relationship.

$$A = \frac{G_F}{4\pi\alpha\sqrt{2}}[Q_W^p Q^2 + Q^4 B(Q^2)] \ , \tag{5.1}$$

where G_F is the Fermi's coupling constant, α is the fine structure constant, Q_W^p is the weak charge of the proton, Q^2 is the four momentum transfer, and $B(Q^2)$ contains the form factor corrections.

The four momentum is a function of the three variables in the following equation,

$$Q^2 = 4EE' \sin^2\theta/2 \ , \tag{5.2}$$

where E is the energy of the incident particle, E' is the energy of the incident particle after the collision, and θ is the scattering angle of the incident particle. Since the scattering of interest is elastic and only two-body, the post scattering energy can be written,

$$E' = \frac{E}{1 + 2\frac{E}{M_p}\sin^2\theta/2} \ , \tag{5.3}$$

where M_p is the mass of the proton, the target particle. Combining Equation 5.2 and

Equation 5.3 one can rewrite Q^2 as a function of only two variables,

$$Q^2 = \frac{4E^2 \sin^2 \theta/2}{1 + 2\frac{E}{M_p} \sin^2 \theta/2} \ . \tag{5.4}$$

The tracking subgroup of the Qweak collaboration will choose which two of the three variables will be used in the final determination of Q^2. The third variable will then be used as a cross check. The likely choice will be E and θ, the energy and the scattering angle, because E' requires more assumptions about the geometry of the Qweak apparatus while E and θ are directly measured.

5.1.1 Beam Energy

The beam energy is precisely determined by using absolute position determination of the electron beam at the opening, middle, and exit of the Hall C arc. The position determination is carried out by superharps [48, 49], which scan a 10 μm wire tranversely through the beam. When the beam strikes the wire a current is induced and the position of the wire is recorded by a high precision encoder. An individual superharp system's resolution is limited by the width of the wire.

One of the magnetic fields of a bending magnet in the Hall C arc was mapped and the other three are assumed identical. Knowing the magnetic field traversed by the electron in addition to its entry and exit points one can determine the beam energy to a precision of 10^{-4}. Incident beam energy is the best known of the three variables in the Q^2 calculation and will likely be used in the final determination of Q^2.

One measurement of the beam energy occured before the 25% dataset and one occured after. The first measurement was 1160.33 $\pm$ 0.1 MeV and the second was 1160.44 $\pm$ 0.1 MeV.

5.1.2 Scattered Beam Angle

The scattered beam angle is determined from the HDCs described in the apparatus section. There are two HDCs on both sides of the beamline before the QTOR bending magnet. Because they are in front of QTOR the flux detected by the HDCs includes all of the scattered particles from 4 to 12∘. This flux of particles is dominated by lower energy Møller scattered electrons and limits the beam current at which the HDCs can be operated. The VDCs were able to take data at a beam current of 100 nA but the high rate in the HDCs limited dedicated Q^2 runs to 100 pA. At 100 pA the cosmic ray triggers in the VDCs and trigger scintillators were a significant source of background. A coincidence between two trigger scintillators would have greatly reduced the number of cosmics recorded.

Each event in Figure 5.1 was a "good" event. This is defined to be an electron that passes through QTOR and hits the trigger scintillator. This also means it was a charged particle, had the correct momentum to navigate the QTOR field, and had a scattering angle within the Qweak acceptance.

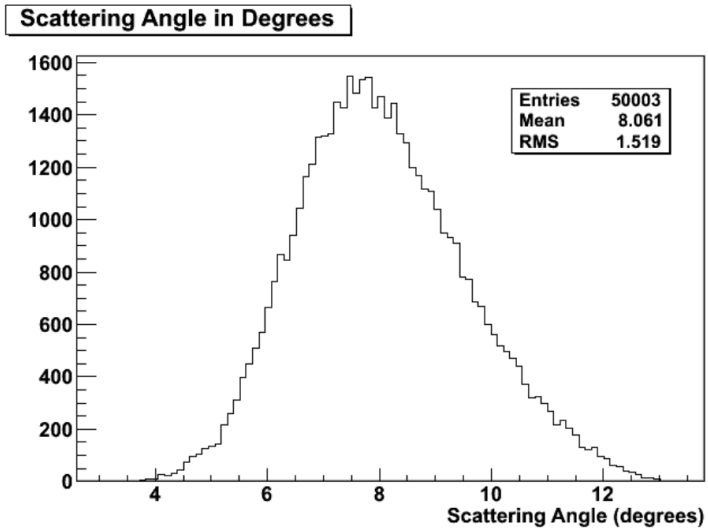

Figure 5.1: *Scattering angle of electrons.*

5.1.3 Reconstructed Q^2 for the 25% Dataset

A statistically precise determination of Q^2 can be made with only minutes of beam time. The dominant uncertainty comes from systematic effects including, but not limited to, reproducibility of measurement, beam parameter dependence, and raster dependence. Leckey's dissertation discusses many of these systematic corrections and the uncertainties assigned to them [21].

For the 25% dataset a simulation of the Q^2 would be sufficient. However, the uncertainty needed for the 4% dataset is 0.5%, and a simulation will not suffice.

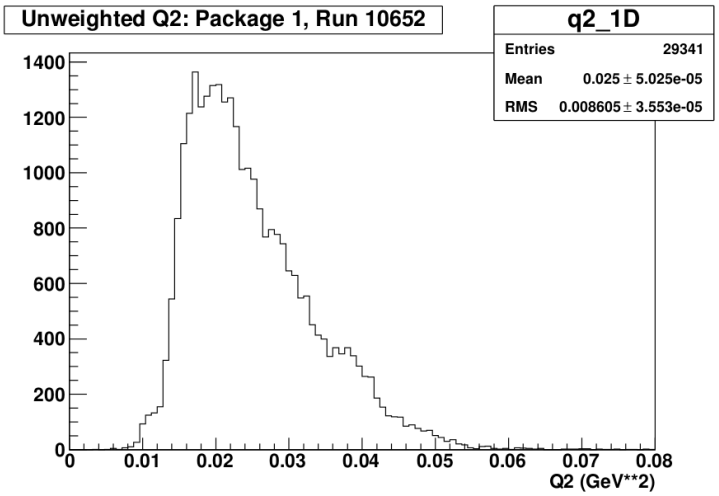

Figure 5.2: *Reconstructed Q^2 for the 25% dataset.*

The final value for the four momentum used in this analysis is $Q^2 = 0.0252 \pm 0.0007$ GeV^2. More information can be found in Myers's thesis [27].

5.2 Polarization

Qweak had two polarimeters for the majority of the experiment. However, the Compton Polarimeter was still being commissioned during the 25% dataset. Results for the Møller polarimeter during the 25% dataset will be presented here.

5.2.1 Møller Polarimeter

Approximately three times a week the Møller polarimeter would take a 0.3% measurement of the polarization of the beam. Each measurement would consist of three measurements with the half-wave plate IN and three measurements with the half-wave plate OUT. The value for the polarization of the beam during the 25% measurement was (88.88 ± 2.52)%. The errors in Figure 5.3 are only statistical and systematics dominate the uncertainty for this dataset.

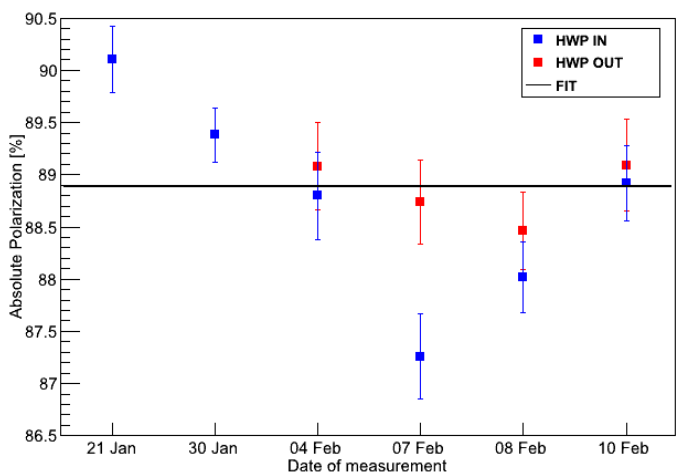

Figure 5.3: *Polarimetry data for the 25% dataset.*

Contributions to the uncertainty associated with the polarization for the 25% Q_W^p measure-

ment are listed in Table 5.1. The final uncertainty for the 4% Q_W^p measurement is 1%, so the uncertainties listed in Table 5.1 will need to be reduced.

Table 5.1: Contributions to the uncertainty of the Møller polarization in the 25% dataset

Uncertainty Source	Relative Uncertainty
Statistics	0.97%
Systematics	0.65%
Current Dependence	1%
Quad3	2%
TOTAL	2.52%

In Table 5.1 the systematics uncertainty entry includes beam position, magnet current/position, collimator position, target temperature/polarization, and magnet field direction/strength among less significant contributions. The current dependence entry accounts for the Møller measurement beam current of 2 μA being different from the Qweak experiment beam current of 180 μA. Current dependence studies have been done and this uncertainty will decrease once they have been analyzed.

The Quad3 uncertainty entry in Table 5.1 dominates. This entry addresses the uncertainty of the magnetic field in the third quadrupole. There was a short in this magnet that caused the magnetic field to decay over time. Simulations and field mapping are in progress to reduce this uncertainty but have not been finalized.

5.3 Parity-Violating Asymmetry

The measured asymmetry has several contributions. Equation 5.5 shows the expression for the measured asymmetry,

$$A_m = P \cdot \left[\left(1 - \sum f_{bkgd} \right) A_{ep} + f_{Al} A_{Al} + f_{inel} A_{inel} + f_{bl} A_{bl} \right] + A_{false} \ , \tag{5.5}$$

where A_m is the experimentally measured asymmetry, P is the beam polarization, $1 - f_{tot}$ is the fraction of the total rate seen by the main detectors that is elastically scattered electrons off of protons, A_{ep} is the asymmetry of the elastically scattered electrons, f_{Al} is the fraction of the total rate seen by the main detectors that is from the target's aluminum windows, A_{Al} is the asymmetry of the electrons that are scattered by the target's aluminum windows, f_{inel} is the fraction of the total rate seen by the main detectors that is from inelastic scattering of electrons off of protons, A_{inel} is the asymmetry of the electrons that are inelastically scattered from protons, f_{bl} is the fraction of the total rate seen by the main detectors that is from the beamline, A_{bl} is the asymmetry of the electrons originating from the beamline, and A_{false} is the contribution to the measured asymmetry caused by beam parameter correlations with the measured asymmetry.

The detector signals are divided by the beam current value to remove any leading order charge dependence. However, there is a $\sim$2% nonlinearity in the main detectors that has not been accounted for. By keeping the charge asymmetry small and its width relatively narrow the contribution to the measured asymmetry will be small. A charge feedback loop was implemented to reduce the mean of the charge asymmetry. The charge asymmetry is monitored via the data acquisition system and the Pockels cell voltage is adjusted to move the asymmetry closer to zero.

Some time was spent trying to find a neutral beam axis to take full advantage of the azimuthal symmetry of the Qweak experiment. Ideally, the position and angle of the beam would be such that opposing detector sensitivities to beam parameters would identically cancel. Such a beam position and angle is called a neutral axis. The cancellation of the sensitivities for Qweak was approximately a factor of 10, which is similar to what other experiments

achieved.

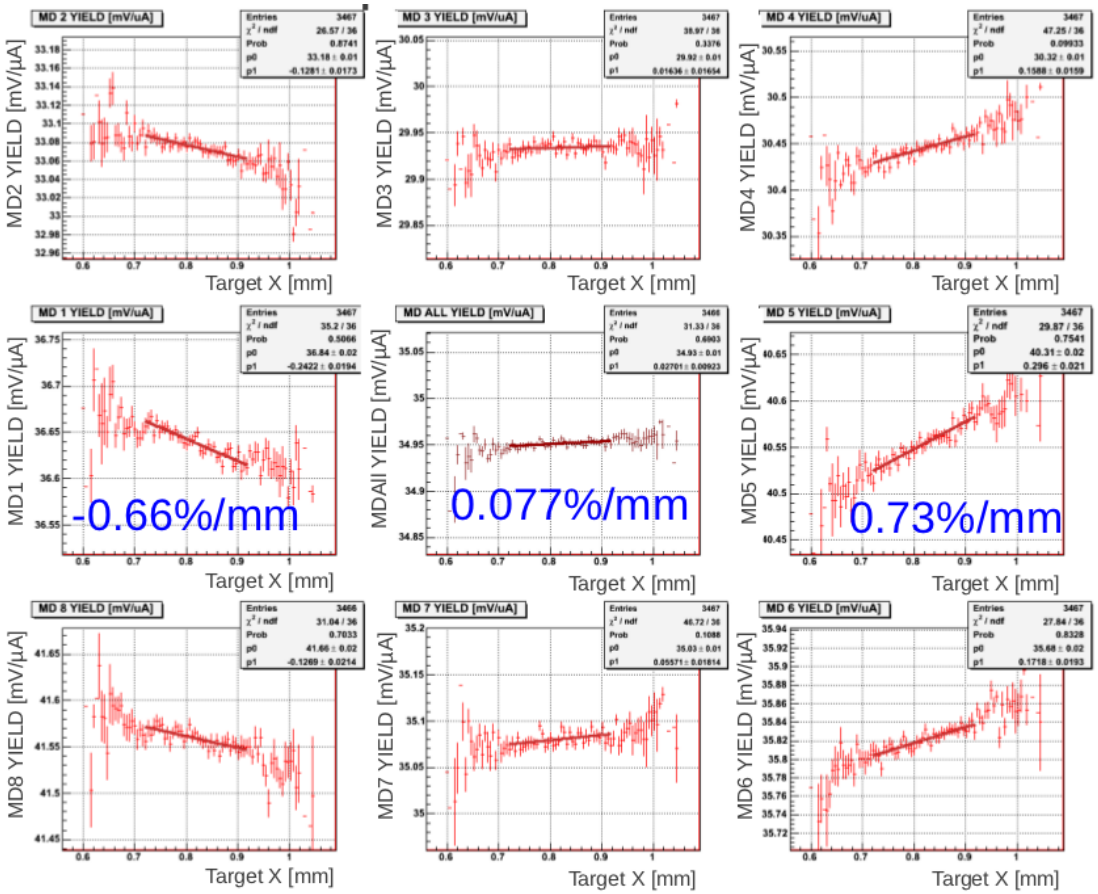

Figure 5.4: *Main detector sensitivity cancellation for the Qweak experiment. Clockwise from middle left is md1, md2, md3, md4, md5, md6, md7, and md8. The center plot is a weighted average of all of the main detectors. The Y axis is the normalized yield and the X axis is the helicity correlated beam position measured in the X direction and projected to the center of the target.*

Figure 5.4 shows the ring of eight main detectors and the central plot is the weighted average of the all the main detector sensitivities. A smaller average sensitivity reduces the size of the regression correction.

As stated above, the measured asymmetry has many components. Separating the contributions from each source would be impossible during production running because several thousand electrons are all integrated into one signal. Each of these contributions need to either be estimated by simulation or measured, if possible. Each contribution will be addressed in later sections.

5.3.1 Regression

Regression is used to remove the false asymmetries due to beam parameters. Regression assumes a linear correlation between each variable, beam position in X, beam position in Y, beam angle in X, beam angle in Y, energy, and charge asymmetry. A matrix of these correlations is then inverted revealing the de-correlated sensitivities of the measured asymmetry to each beam parameter. The false asymmetry due to beam parameters is then calculated according to Equation 5.6,

$$A_{false} = \sum_i \frac{\partial A}{\partial P_i} \Delta P_i \ , \tag{5.6}$$

where $\frac{\partial A}{\partial P_i}$ is the de-correlated sensitivity of the measured asymmetry to the beam parameter and ΔP_i is the helicity correlated mean of the beam parameter.

This procedure takes advantage of the intrinsic "jitter" of the electron beam in position and angle to determine sensitivities. Another method for determining the sensitivities involves intentionally modulating the beam position and angle. This method was not functioning for the 25% dataset.

Several regression schemes were used in analyzing these data. They are defined in Table 5.2. The purpose of the regression variables is to determine the helicity correlated beam parameters at the target. Because this can be done several ways, nine regression schemes were developed to determine our sensitivity to different regression variables.

The prefix *diff* is used to denote that the helicity correlated difference is being reported except for the energy variable which is *dp/p*. *asym* defines the variable as an asymmetry. *qwk* is Qweak jargon that denotes the variable is being recorded by a high precision 18-bit ADC. *targetX* and *targetY* are position variables and *targetXSlope* and *targetYSlope* are angle variables. *bpm3c12X* is an alternate measure of the energy of the electron beam.

Table 5.2: Regression schemes

std	5+1	set3
diff_qwk_targetX	diff_qwk_targetX	diff_qwk_targetX
diff_qwk_targetY	diff_qwk_targetY	diff_qwk_targetY
diff_qwk_targetXSlope	diff_qwk_targetXSlope	diff_qwk_targetXSlope
diff_qwk_targetYSlope	diff_qwk_targetYSlope	diff_qwk_targetYSlope
diff_qwk_energy	diff_qwk_energy	diff_qwk_bpm3c12X
	asym_qwk_charge	asym_qwk_charge

set4	set5	set6
diff_qwk_targetX	diff_bpm_9b4pX	diff_bpm_9b4pX
diff_qwk_targetY	diff_bpm_9b4pY	diff_bpm_9b4pY
diff_qwk_targetXSlope	diff_bpm_9b4mX	diff_bpm_9b4mX
diff_qwk_targetYSlope	diff_bpm_9b4mY	diff_bpm_9b4mY
diff_qwk_energy	diff_qwk_bpm3c12X	diff_qwk_bpm3c12X
asym_qwk_bcm5		asym_qwk_charge

set7	set8	set9
diff_bpm_94pX	diff_bpm_94pX	diff_bpm_94pX
diff_bpm_94pY	diff_bpm_94pY	diff_bpm_94pY
diff_bpm_94mX	diff_bpm_94mX	diff_bpm_94mX
diff_bpm_94mY	diff_bpm_94mY	diff_bpm_94mY
diff_qwk_bpm3c12X	diff_qwk_bpm3c12X	diff_qwk_bpm3c12X
	asym_qwk_charge	asym_qwk_charge
		asym_uslumi_sum

Note that,

diff_bpm_9b4p ≡ diff_qwk_bpm3h09b + diff_qwk_bpm3h04,

diff_bpm_94p ≡ diff_qwk_bpm3h09 + diff_qwk_bpm3h04,

diff_bpm_9b4m ≡ diff_qwk_bpm3h09b - diff_qwk_bpm3h04,

diff_bpm_94m ≡ diff_qwk_bpm3h09 - diff_qwk_bpm3h04,

involve only two beam position monitors. The p refers to plus and represents position-like variables. The m refers to minus and represents angle-like variables. Beam position and direction regression variables that include more than two beam position monitors are diff_qwk_targetX, diff_qwk_targetY, diff_qwk_targetXSlope, diff_qwk_targetYSlope, and diff_qwk_energy. Regression schemes std, set5, and set7 do not include any charge asymmetry regression variables. Regression scheme set9 includes the upstream luminosity monitor asymmetry. The effect of including the upstream luminosity monitor asymmetry in the regression has not been studied in detail nor is there a working model. The regression scheme set9 will be ignored for this analysis.

5.3.2 Transverse Asymmetry

The longitudinal polarization of the electron beam is determined by the magnitude of the polarization vector and is set by the longitudinal polarization of the low energy electrons as the leave the GaAs crystal. There is a transverse polarization component if the polar angle between the polarization vector and the Z direction in the experimental hall is nonzero. Other than for special runs, the transverse polarization of the electron beam was constrained to be less than 5% and was typically smaller.

Transversely polarized electrons have an azimuthal asymmetry, and, given a perfectly azimuthally symmetric detector system, conserve parity. An issue arises when the detection system is not perfectly azimuthally symmetric.

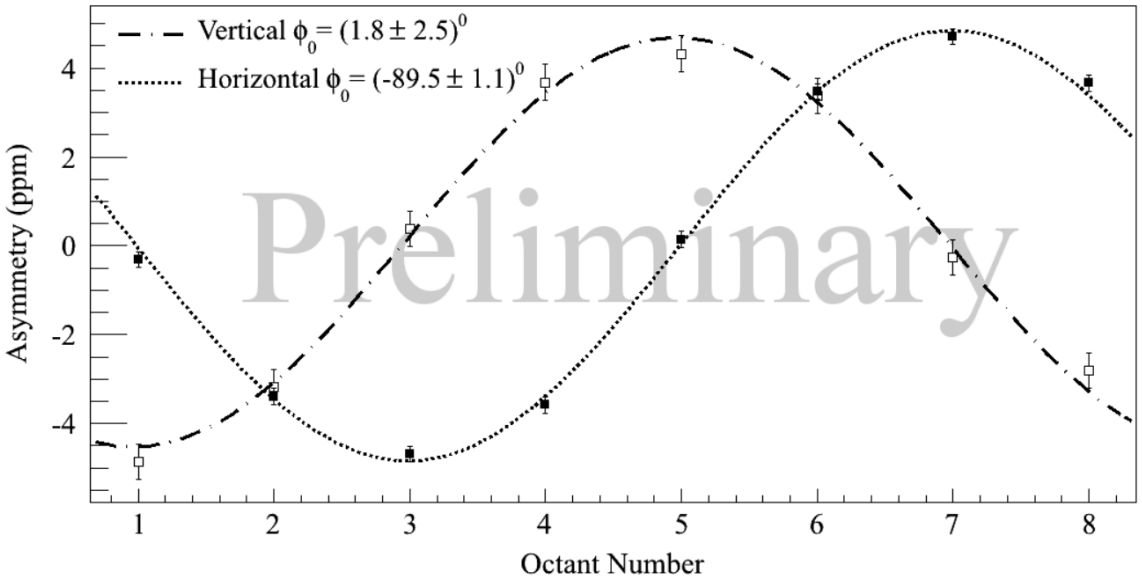

Figure 5.5: *Preliminary results of the transverse asymmetry measurement. The amplitude is ∼4 ppm and the azimuthal dependence can be easily seen.*

Figure 5.5 shows the azimuthal dependence of the measured asymmetry when the electron

beam is completely transversely polarized. For the elastic and inelastic analysis described in this thesis the transverse asymmetry contributes to the systematic error. However, in the final extraction of the elastic asymmetry a correction may be applied due to transverse symmetry breaking. More information can be found in Waidywansa's CIPANP 2012 conference proceedings [43].

5.3.3 Aluminum Background

The aluminum contribution to the measured asymmetry is the largest. While the majority of the particles in the Qweak acceptance interact within the liquid hydrogen, $\sim$3% of the total originated from either the upstream or downstream aluminum window. This dilution of the desired elastic electron-proton signal due to the aluminum background is relatively small. However, the expected aluminum asymmetry is almost a factor of 10 larger than the elastic electron-proton asymmetry. The expected correction due to aluminum dilution is approximately 30%.

Because the correction was expected to be large, the dilution needed to be known precisely. Dedicated runs were taken with different pressures of hydrogen gas in the target cell. Using the known pressure of hydrogen gas at three different points one can extrapolate to zero pressure. Data was also taken an evacuated target cell and the results agreed with the extrapolation technique. The result of those studies is shown in Figure 5.6. The value of the dilution used in this analysis is 0.0367 ± 0.0031.

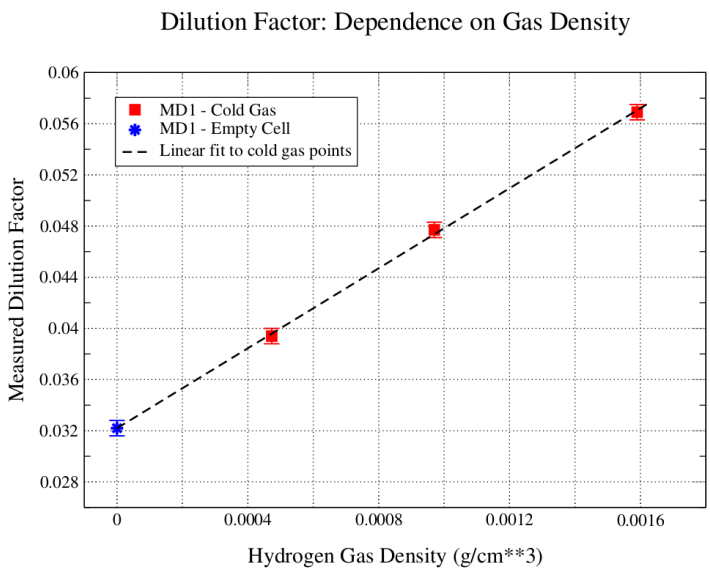

Figure 5.6: *Aluminum dilution measurements at different hydrogen gas pressures.*

The aluminum asymmetry was measured with aluminum "dummy" targets made of the same alloy as the target windows. The dummy targets were much thicker than the hydrogen cell windows and could handle much more beam current. This allowed a relatively quick measurement of the aluminum asymmetry.

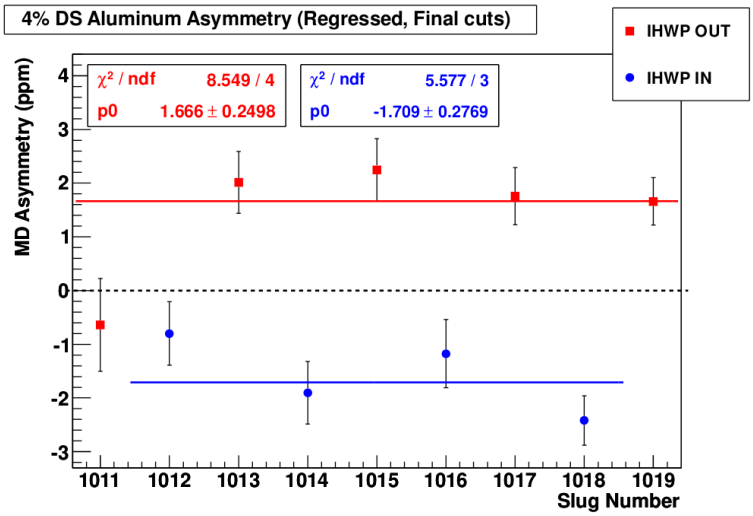

Figure 5.7: *Aluminum asymmetry results grouped in eight hour datasets or slugs.*

Figure 5.7 shows the data quality of several aluminum measurements. The value of the aluminum asymmetry used in this analysis is 1.52 ± 0.19 ppm. More information about the aluminum analysis can be found in Katherine Myers's thesis [27].

5.3.4 Inelastic Background

The inelastic background is a relatively small contribution to the measured asymmetry. A small fraction of the total rate of electrons at the production QTOR value of 8921 A are from electrons scattering inelastically off of protons in the target. The first resonance of the proton is the Δ and the tail of that resonance fails into the Qweak acceptance. The asymmetry of the inelastic asymmetry was expected to be a factor of 10 larger than the elastic asymmetry and the dilution was estimated to be as high as 0.2%. This would have been a 2% correction.

Measuring the asymmetry of the inelastic contribution is not as straight forward as the

aluminum measurement. There is no target that would provide solely inelastic events so the Qweak spectrometer needed to be altered. Simulations of the Qweak experiment were used to determine the QTOR focusing magnet value that would provide the highest fraction of inelastic events was performed. Figure 5.8 shows the fraction of inelastic events at several QTOR settings. Note 8921 A is where production running took place and 6700 A is where inelastic running took place.

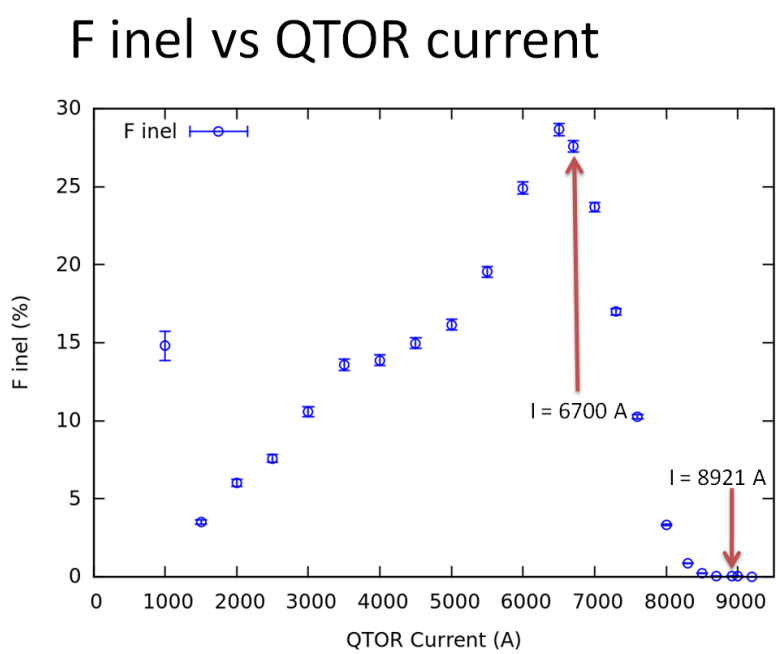

Figure 5.8: *Inelastic dilution.*

The fraction of events that are inelastic at 8921 A is 0.0002 ± 0.000005 (stat. only). The fraction of inelastic events at 6700 A is 0.2757 ± 0.0036 (stat. only). The dominating signal at 6700 A is due to the radiative tail of the elastic events.

To measure the inelastic contribution the QTOR bending magnet current was reduced to 75% of its nominal value to 6700 A. At this QTOR setting, the inelastic contribution $f_{inel}A_{inel} =$ 0.8 ppm, would dominate the elastic radiative tail contribution $f_{ep}A_{ep} = 0.13$ ppm.

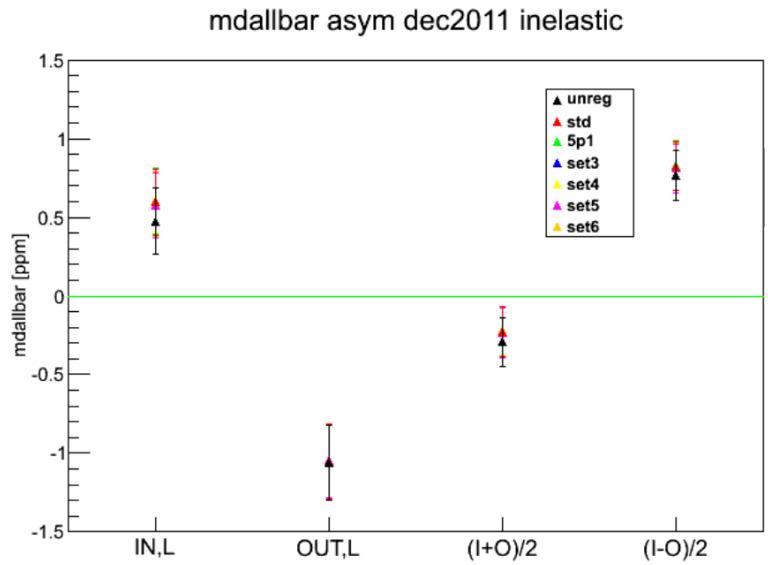

Figure 5.9: *Inelastic asymmetry.*

Figure 5.9 shows the data quality for the inelastic dataset from December 2011. The data was taken at the HWP and Wien settings of IN, LEFT and OUT, LEFT. The (I+O)/2 is a zero check to insure systematic effects between the two half-wave plate settings cancel. For 5+1 regression (I+O)/2 = -0.235 ± 0.156 ppm which is 1.5 σ from zero. This is an acceptable level of cancellation and has a 13% probability of occurring by chance. As one can see from the plot the (I+O)/2 improves after regression. To combine this data to get the measured asymmetry one needs to take a weighted average of HWP states and correct the sign for HWP, Wien, and 2-pass accelerator sign flips. More detail on the inelastic data analysis is given in Chapter 6. However, the result of the detailed inelastic analysis is needed to continue with the elastic analysis. After corrections, $A_{inel} = -3.02 \pm 0.97$ ppm.

5.3.5 Beamline Background

Beamline backgrounds encompass all events that can create a signal in the main detectors not originating from the target. This background was significantly reduced by the addition of shielding throughout the Qweak experiment. The largest reduction in beamline background was due to the tungsten collimator placed inside of the first collimator. It was composed of a water cooled corkscrew shaped cylinder of tungsten with an inner radius $\sim$7 mm. This collimator absorbed small scattering angle events directly downstream of the target before they could interact with the apparatus.

Initially, the main detectors were unshielded, but higher than expected soft backgrounds led the collaboration to preradiate the main detectors. Preradiating refers to placing some amount of material to shield the detectors from low energy particles and cause a shower of the higher energy particles. This boosts the signal from high energy electrons while suppressing the signal from low energy backgrounds. Extra shielding was also put in place throughout the beamline where the main detectors had line of sight of the beamline. Nevertheless, there is a small dilution due to events from the beamline that avoid the shielding and create a signal within the main detectors.

A plan to measure the beamline dilution was developed that included blocking different collimator's octants in such a way to determine the source of the signals in the main detectors. By blocking an octant in the first collimator the events from the target are highly suppressed. This leaves only events from downstream of the first collimator. By blocking the octant in the second collimator, only events generated downstream are left. The beamline background was determined from comparing the blocked octants to the unblocked octants.

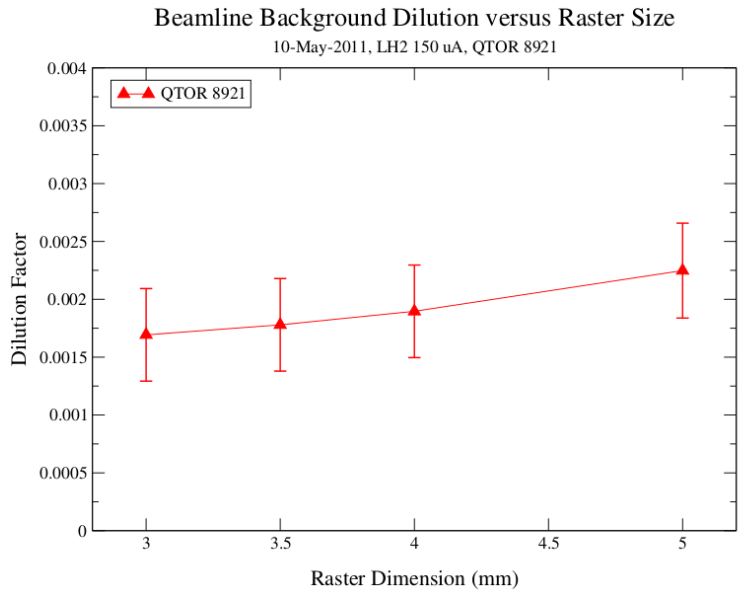

Figure 5.10: *Beamline dilution for production running with QTOR at 8921 A.*

The dilution due to beamline events for production running at QTOR 8921 A are shown in Figure 5.10. The final value for the dilution is $f_{bl} = 0.00184 \pm 0.00046$. More details on the beamline dilution measurement can be found in Myers's thesis [27].

The asymmetry of the beamline background is needed to constrain its contribution to the measured asymmetry. This asymmetry was measured by the background detector, *pmtonl*. During the 25% dataset this detector was placed where it would be sensitive to the diffuse room background. *pmtonl* is a main detector PMT not coupled to a radiator. Before Wien 2, it was placed in the superelastic region of the acceptance. The superelastic region is a better estimate of the beamline background, so the asymmetry values for Wien 0 and Wien 1 will be ignored for this analysis.

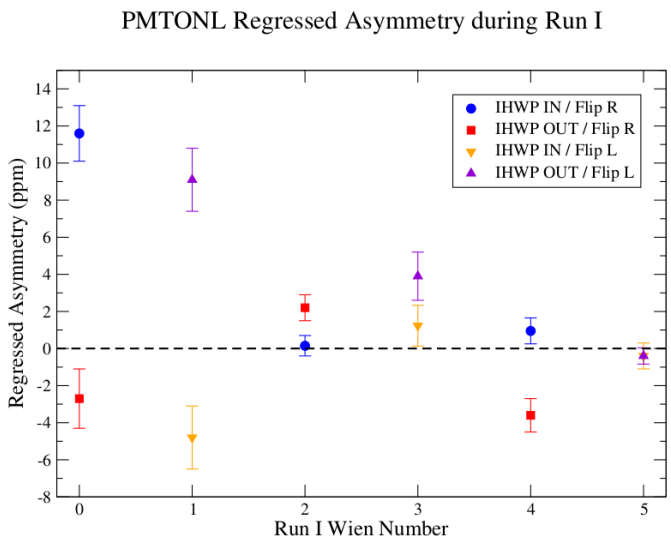

Figure 5.11: *Beamline asymmetries for Run I. Wien 0 is the 25% dataset but the background detectors were not moved to the superelastic region until the start of Wien 2.*

Using the dilution results of the blocked octant study from Figure 5.10 and the asymmetries measured by the background detectors from Figure 5.11 an estimate of the contribution to the measured asymmetry from beamline events can be obtained. The asymmetry value used for this analysis is $A_{bl} = 0 \pm 2$ ppm.

5.4 Elastic Electron-Proton Asymmetry

The measured asymmetry is a combination of elastic electron-proton scattering and numerous backgrounds. For this analysis slug rootfiles with minimal cuts were used. A slug rootfile is a chunk of data approximately eight hours in length where no large changes in the experimental setup are allowed. For example, each slug rootfile contains only one half-wave plate setting and one Wien setting. No cuts to remove outlier beam parameter sensitivities were applied.

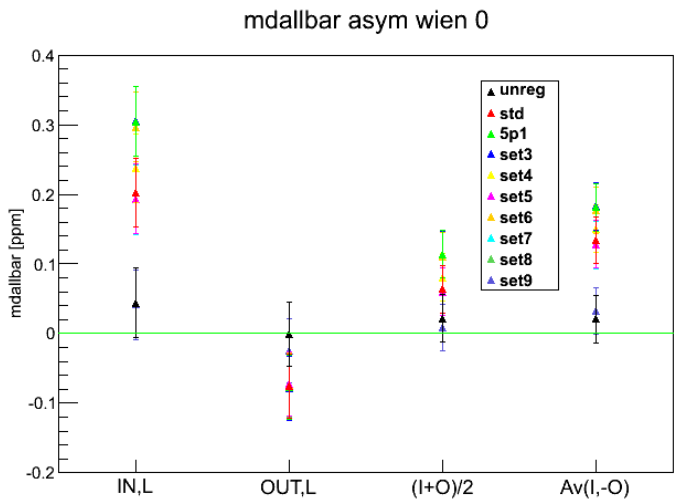

Figure 5.12: *25% dataset measured asymmetry.*

Figure 5.12 shows the combined main detector bar asymmetry measured during the 25% dataset with minimal cuts. The regression scheme set9 includes the upstream luminosity monitor asymmetry and will be ignored for this analysis.

Table 5.3: Measured asymmetries using different regression schemes for 25% dataset in ppm

Reg. Scheme	IN	OUT	(IN+OUT)/2	Av(IN,-OUT)	err Av(IN,-OUT)
raw	0.0440	-0.0008	0.0216	0.0207	0.0341
std	0.2025	-0.0756	0.0635	0.1341	0.0339
5+1	0.3048	-0.0766	0.1141	0.1815	0.0338
set3	0.3053	-0.0784	0.1134	0.1828	0.0339
set4	0.2375	-0.0763	0.0806	0.1504	0.0339
set5	0.1934	-0.0729	0.0602	0.1285	0.0340
set6	0.2969	-0.0748	0.1111	0.1770	0.0339
set7	0.1923	-0.0720	0.0602	0.1275	0.0340
set8	0.2965	-0.0747	0.1109	0.1768	0.0339
set9	0.0414	-0.0245	0.0085	0.0323	0.0338

The schemes std, set5, and set7 do not include charge asymmetry as a regression variable. Charge asymmetry was shown to be an important factor in the stability of the beam parameter sensitivities. Without charge asymmetry regression the results are suspect. BCM5 is a charge asymmetry regression variable in set4, but since it was not properly calibrated for this running, the set4 regression scheme should be ignored. The regression schemes considered for the following analysis include 5+1, set3, set6, and set8. Keep in mind the regression schemes all had the same raw data input. If regression were perfect, each scheme would produce identical results.

Table 5.4: Good regression schemes and the mean for 25% dataset in ppm

Reg. Scheme	IN	OUT	(IN+OUT)/2	Av(IN,-OUT)	err Av(IN,-OUT)
5+1	0.3048	-0.0766	0.1141	0.1815	0.0338
set3	0.3053	-0.0784	0.1134	0.1828	0.0339
set6	0.2969	-0.0748	0.1111	0.177	0.0339
set8	0.2965	-0.0747	0.1109	0.1768	0.0339
mean	0.3009	-0.0761	0.1123	0.1795	0.0339

The mean (IN+OUT)/2 zero check is 3 σ from zero which means there is a $2.7{\cdot}10^{-3}$ probability that this fluctuation occurred solely by chance. Likely, there is some unknown systematic issue with these data that must be corrected before unblinding.

5.4.1 Cut Dependence

Figures 5.13 and 5.14 show the measured asymmetry's dependence on cuts placed on the charge asymmetry regression variable. The lines in the figures represent the allowed shift in the mean due to loss of events by cuts. Equation 5.7 describes the allowed statistical shift due to events lost assuming a gaussian distribution,

$$\Delta^{pt2pt}_{i\to j} = \sigma_i \left(\frac{1}{\sqrt{N_j}} - \frac{1}{\sqrt{N_i}} \right) , \tag{5.7}$$

where N_i is the number of events in the uncut distribution, N_j is the number of events in the cut distribution, and σ_i is the RMS of the uncut distribution.

Other beam parameter regression variable cut dependence plots were generated but none showed as an effect as dramatic as the charge asymmetry.

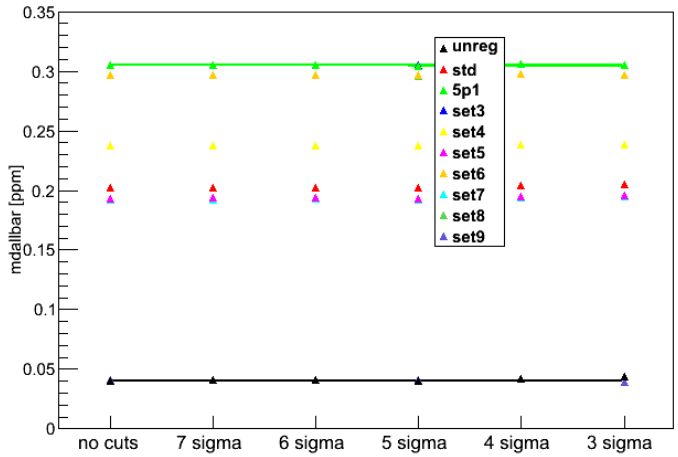

Figure 5.13: *Cut dependence of 25% dataset HWP IN.*

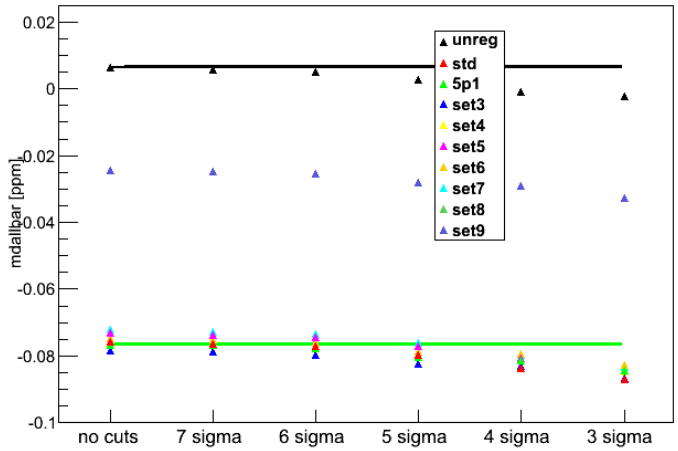

Figure 5.14: *Cut dependence of 25% dataset HWP OUT.*

Table 5.5 and 5.6 show the measured asymmetry after removing any event that fell outside of 5 σ of the following beam parameters, diff_qwk_targetX, diff_qwk_targetY, diff_qwk_targetXSlope, diff_qwk_targetYSlope, diff_qwk_energy, and asym_qwk_charge.

Table 5.5: Regression schemes with 5 σ cuts on each beam parameter mean for 25% dataset in ppm

Reg. Scheme	IN	OUT	(IN+OUT)/2	Av(I-O)	err Av(I-O)
raw	0.0823	0.0026	0.0424	0.0398	0.0342
std	0.2435	-0.0821	0.0807	0.1628	0.0340
5+1	0.2809	-0.0773	0.1018	0.1791	0.0340
set3	0.2814	-0.0802	0.1006	0.1808	0.0340
set4	0.2575	-0.0800	0.0887	0.1687	0.0340
set5	0.2340	-0.0809	0.0766	0.1574	0.0340
set6	0.2736	-0.0770	0.0983	0.1753	0.0340
set7	0.2327	-0.0803	0.0762	0.1565	0.0340
set8	0.2731	-0.0766	0.0982	0.1748	0.0340
set9	0.0049	-0.0243	-0.0097	0.0146	0.0340

The regression scheme agreement does not improve with the 5 σ beam parameter cuts.

Table 5.6: Good regression schemes with 5 σ cuts on each beam parameter mean for 25% dataset in ppm

Reg. Scheme	IN	OUT	(IN+OUT)/2	Av(I-O)	err Av(I-O)
5+1	0.2809	-0.0773	0.1018	0.1791	0.0342
set3	0.2814	-0.0802	0.1006	0.1808	0.0340
set6	0.2736	-0.0770	0.0983	0.1753	0.0340
set8	0.2731	-0.0766	0.0982	0.1748	0.0340
mean	0.2772	-0.0778	0.0997	0.1775	0.0340

Note that the asymmetry must be sign corrected due to the HWP and Wien configuration

during the 25% measurement. The mean (IN+OUT)/2 zero check is 2.9 σ from zero, which means there is a $4{\cdot}10^{-3}$ probability that this fluctuation occurred solely by chance. The cuts improve the agreement with zero but the disagreement is still unlikely statistical. Because the means of the regression schemes should be identical, an additional uncertainty is needed and will be discussed in Section 5.6.

5.5 Corrections

Using the mean value of the measured asymmetry for the good regression schemes with beam parameter cuts, $A_m = -177.5 \pm 34$ ppb, one must now correct for the contributions defined in Equation 5.5 not associated with the elastic electron-proton scattering. Note that A_{false} has already been removed from this value by regression. Solving Equation 5.5 for A_{ep} one gets,

$$A_{ep} = \frac{A_m/P - f_{Al}A_{Al} - f_{inel}A_{inel} - f_{bl}A_{bl}}{1 - \sum f_{bkgd}} \ . \tag{5.8}$$

Table 5.7: Contributions to the measured asymmetry

Background	Dilution Factor	Asymmetry [ppm]	Correction [ppb] ($f_{bkgd}A_{bkgd}$)
Al	0.0367 ± 0.0031	1.52 ± 0.19	55.7
Inelastic	0.0002 ± 0.000005	-3.02 ± 0.97	-0.6
Beamline	0.00184 ± 0.00046	0.0 ± 2.0	0.0
TOTAL	0.0387		55.1

The total correction due to backgrounds is $\sum f_{bkgd}A_{bkgd} = 55.1$ ppb. The false asymmetry corrected by regression is $A_{false} = 135.9$ ppb giving a total correction of 191 ppb. This correction is ∼70% of the extracted elastic electron-proton asymmetry and is unacceptable

for the final 4% measurement. Issues with the injector during the 25% measurement caused this heavy reliance on regression. The problem was fixed soon after this measurement and should be a much smaller correction for the high precision measurement.

5.6 Uncertainties

The uncertainties associated with the extraction of the elastic asymmetry are given in Table 5.8. The largest uncertainty of the extraction of the elastic asymmetry is due to blinding. This uncertainty will drop to zero when unblinding takes place. More detail about blinding can be found in at the beginning of Chapter 5.

The second largest uncertainty is due to the statistical precision of the measurement. A statistical uncertainty that is approximately the same size as the systematic uncertainty is desired for experimental physics whereby the result is not limited by either.

Table 5.8: Contributions to the uncertainty of A_{ep}

Source	Contribution [ppb]
Blinding	68
Statistics	40
Regression (A_{false})	14
Transverse asymmetry	10
Al asymmetry	7.2
Polarization	5.9
Al dilution	5.7
Regression variation	4
Beamline asymmetry	3.8
Beamline dilution	0.4
Inelastic asymmetry	0.2
Inelastic dilution	0.04
TOTAL (without blinding)	45
TOTAL	82

The uncertainty due to the aluminum and beamline backgrounds were discussed earlier and the inelastic background will be discussed in detail in Chapter 6.

The uncertainty labeled Regression (A_{false}) is due to the uncertainty associated with the determination of the mean and correlated slopes during the regression procedure.

The variation between the values produced by different regression schemes in Table 5.6 must be included. This variation about the mean was 4 ppb.

The polarization error is dominated by a 2% systematic uncertainty that will be reduced as

more analysis and simulation take place. More detail is given in Section 5.2.

Transverse asymmetry is discussed in Section 5.3.2. The uncertainty associated with the transverse asymmetry is a product of the measured transverse amplitude (4 ppm), a very conservative main detector symmetry breaking factor (1/20), and the worse case residual transverse polarization during the inelastic dataset (5%).

The final value of the elastic electron-proton asymmetry is $A_{ep} = -265 \pm 40 \pm 22 \pm 68$ ppb (stat., sys., and blinding).

Chapter 6

Inelastic Electron-Proton Analysis

This chapter is a detailed analysis of the inelastic background measurement described briefly in Section 5.3.4. These data were taken with 75% of nominal QTOR bending magnet current but otherwise using an unaltered Qweak apparatus. The lower QTOR setting focuses more of the inelastic electrons on the main detector bars while defocusing the elastically scattered electrons.

These data are going to be used to determine the inelastic background for the extraction of the elastic electron-proton asymmetry and constrain the low energy constant d_Δ, described in Section 2.3.

Early estimates of the correction due to the inelastic background were as large as $f_{inel}A_{inel} =$ 4 ppb or 2% of the expected elastic asymmetry. The final error goal on the determination of the elastic electron-proton asymmetry is 4 ppb, so a precise value for the inelastic asymmetry contribution was necessary. Fortunately, more detailed simulations showed the contribution to be just 0.6 ppb.

The quality of the inelastic datasets will be discussed and a detailed analysis of the second

dataset will be presented. This dataset was taken during large helicity correlated beam parameter values due to poor beam conditions. A helicity correlated pedestal survey bracketing and including this inelastic dataset will also be presented.

For the third and final dataset the four momentum, polarization, and background contributions will be discussed along with the corrections, cut dependence, and uncertainties. Finally, the extraction of the inelastic electron-proton asymmetry will be presented.

6.1 Initial Inelastic Dataset

There were three datasets taken at the inelastic QTOR setting of 6700 A. Because beamtime is precious, an initial dataset was taken, which only included a few hours of beam. Once this data was shown to be of good quality, a longer and thus more precise dataset was taken.

Table 6.1: The inelastic datasets

Dataset	Date	Total Beamtime	dA_m	dA_{inel}
1	February 2011	3 hours	0.6 ppm	2.7 ppm
2	April 2011	48 hours	0.2 ppm	0.9 ppm
3	December 2011	60 hours	0.156 ppm	0.7 ppm

Table 6.1 shows when each dataset was taken, how much beamtime was used, the statistical uncertainty on the measured asymmetry, and the expected statistical uncertainty on the extracted A_{inel}.

Table 6.2: The initial inelastic dataset helicity correlated beam parameters

	IN	OUT
Helicity Correlated Beam Variable	Mean	Mean
X position [nm]	-30 ± 25	-22 ± 26
Y position [nm]	4.6 ± 17	-2.9 ± 18
X angle [μrad]	(-8.5 ± 6.3)$\cdot 10^{-4}$	(-3.1 ± 6.6)$\cdot 10^{-4}$
Y angle [μrad]	(-2.4 ± 5.7)$\cdot 10^{-4}$	(-4.7 ± 6.0)$\cdot 10^{-4}$
Energy [ppm]	-11 ± 6.2	7.4 ± 6.5
Charge [ppm]	0.48 ± 0.6	0.58 ± 0.66

Table 6.2 shows the helicity correlated beam parameters for the initial dataset. Large helicity correlated beam parameter values can cause large regression corrections. Beam parameters consistent with zero are desirable, which is essentially the case for this dataset. The energy variable was incorrectly calculated for the initial and second datasets. It is included here so a comparison between the two datasets can be made.

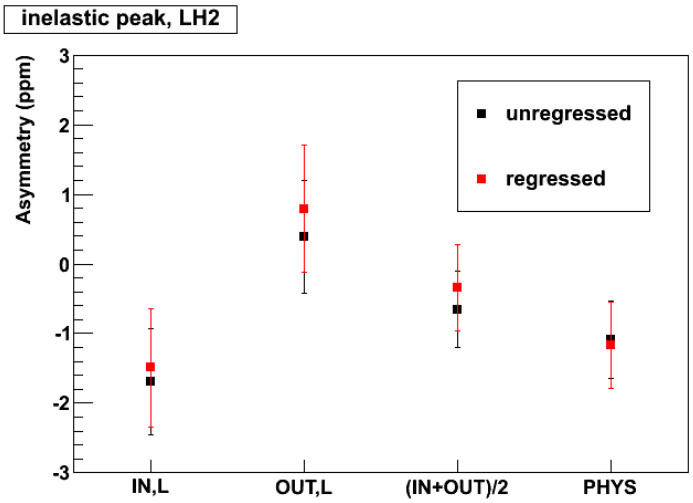

Figure 6.1: *Initial inelastic dataset quality.* IN, L *is the uncorrected asymmetry while the half-wave plate was IN and the wien was LEFT,* OUT, L *is the uncorrected asymmetry while the half-wave plate was OUT and the wien was LEFT,* $(IN + OUT)/2$ *is the average of the IN and OUT values, and* $PHYS$ *is the error weighted sign corrected average of the IN and OUT values. See Section 3.2.1 for more details on the half-wave plate and wien filter.*

Figure 6.1 shows the data quality of the initial dataset with $A_m = -1.2 \pm 0.6$ ppm. The $(IN + OUT)/2$ value is an essential check of the data quality of a parity-violating result. If the $(IN + OUT)/2$ value is not consistent with zero then it is likely systematic effects are shifting the dataset. This check is necessary to control false asymmetries that are hidden due to the small nature of the final expected value. For the initial dataset the $(IN + OUT)/2$ agrees with zero within errors. Both the regressed and unregressed values are presented here. As described in Section 5.3.1, regression removes helicity correlated false asymmetries due to beam parameters.

6.2 Second Inelastic Dataset

The second dataset's regressed systematic zero check, $(IN + OUT)/2$, was an unacceptably large 7 σ from zero. This dataset's quality can be seen in Figure 6.2.

Table 6.3: The second inelastic dataset helicity correlated beam parameters

	IN	OUT
Helicity Correlated Beam Parameter	Mean	Mean
X position [nm]	480 ± 6.1	510 ± 6.7
Y position [nm]	400 ± 4	490 ± 4.5
X angle [μrad]	$1.70{\cdot}10^{-2} \pm 1.70{\cdot}10^{-4}$	$1.70{\cdot}10^{-2} \pm 1.90{\cdot}10^{-4}$
Y angle [μrad]	$1.50{\cdot}10^{-2} \pm 1.60{\cdot}10^{-4}$	$1.80{\cdot}10^{-2} \pm 1.70{\cdot}10^{-4}$
Energy [ppm]	-110 ± 1.3	-81 ± 1.4
Charge [ppm]	-0.64 ± 0.2	-0.31 ± 0.23

Notice the beam position parameters are ∼500 nm and the beam angle parameters are two orders of magnitude larger than in the initial dataset in Table 6.2. The energy variable is an order of magnitude larger than in the initial dataset.

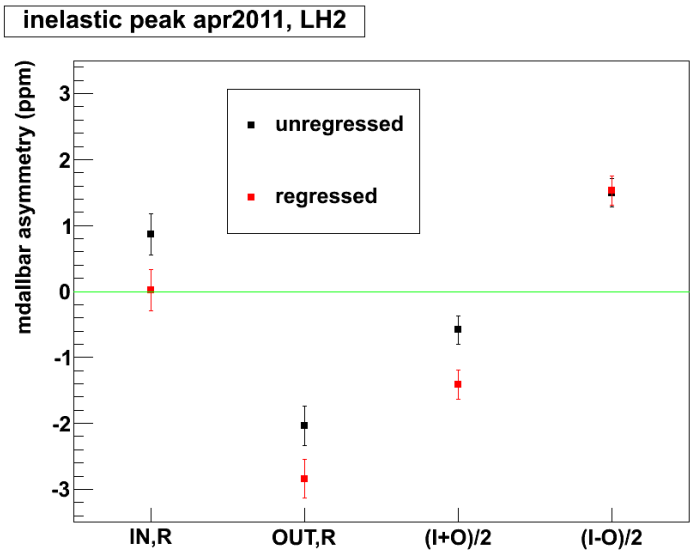

Figure 6.2: *Second inelastic dataset quality.*

6.2.1 (IN+OUT)/2≠0 Hunt

The process to determine the cause of the (IN+OUT)/2 = 0 check will now be discussed. Initially, the regression looked to be correcting with the wrong sign. This was dismissed as the cause after observing the complete removal of correlations between the measured asymmetry and the regression variables in Figures 6.3 and 6.4.

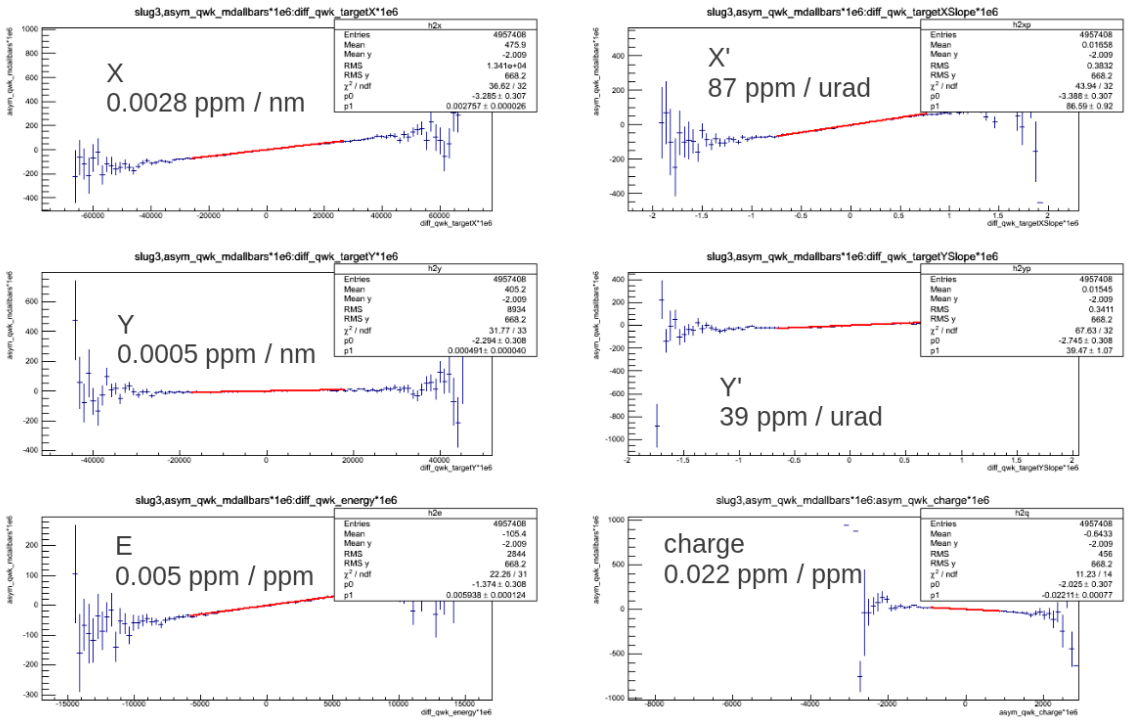

Figure 6.3: *Second inelastic dataset sensitivities before regression.*

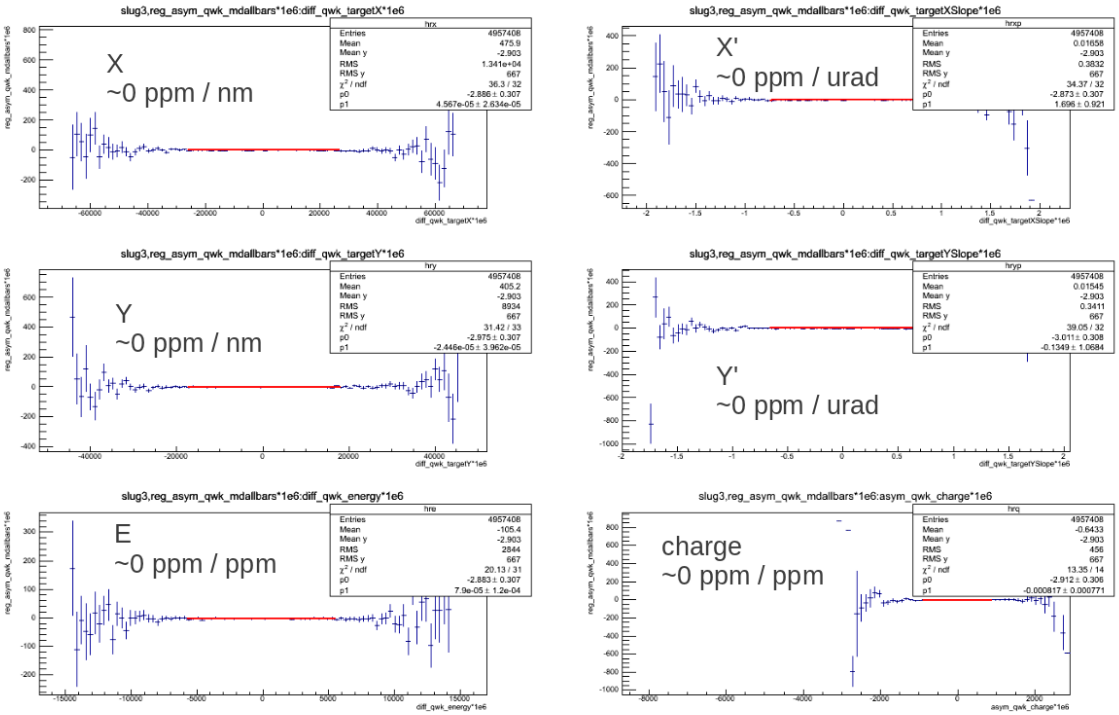

Figure 6.4: *Second inelastic dataset sensitivities after regression.*

The measured asymmetry from each main detector bar should be consistent. Figure 6.5 shows the poor agreement between the bars before regression and Figure 6.6 shows the improved agreement after 5+1 regression.

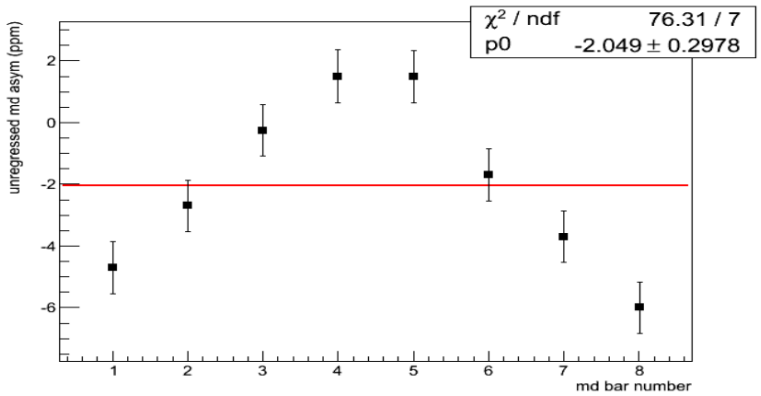

Figure 6.5: *Individual bar measured asymmetry agreement before regression.*

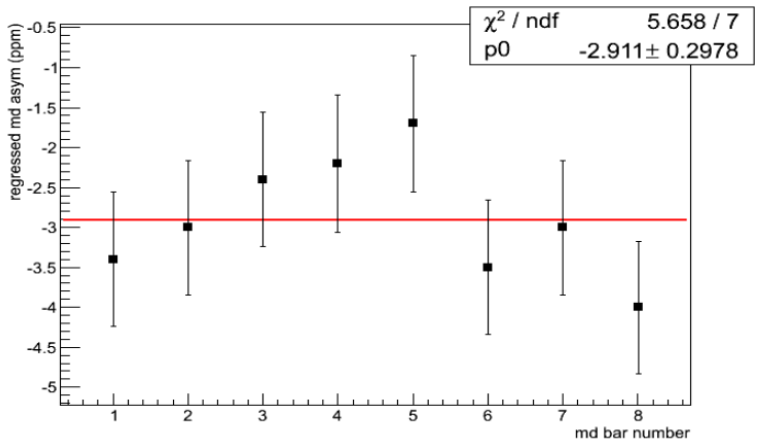

Figure 6.6: *Individual bar measured asymmetry agreement after regression.*

The improved agreement of the individual bars and the lack of correlation between the measured asymmetry and the regression variables exonerates regression as the cause of the (IN+OUT)/2 $\neq$ 0 issue.

Next, the linearity of the main detector bars was examined to insure each bar measured a similar nonlinearity. After standard regression (std) the measured asymmetry was plotted against the charge asymmetry variable. Standard regression does not include the charge asymmetry as a regression variable. The observed nonlinearities were consistent among bars and similar to those observed during normal production (-1.7 ppm/ppm). The nonlinearity did not appear to be the cause of the (IN+OUT)/2 $\neq$ 0 issue. Figure 6.7 shows the agreement between the main detector bar measured asymmetry.

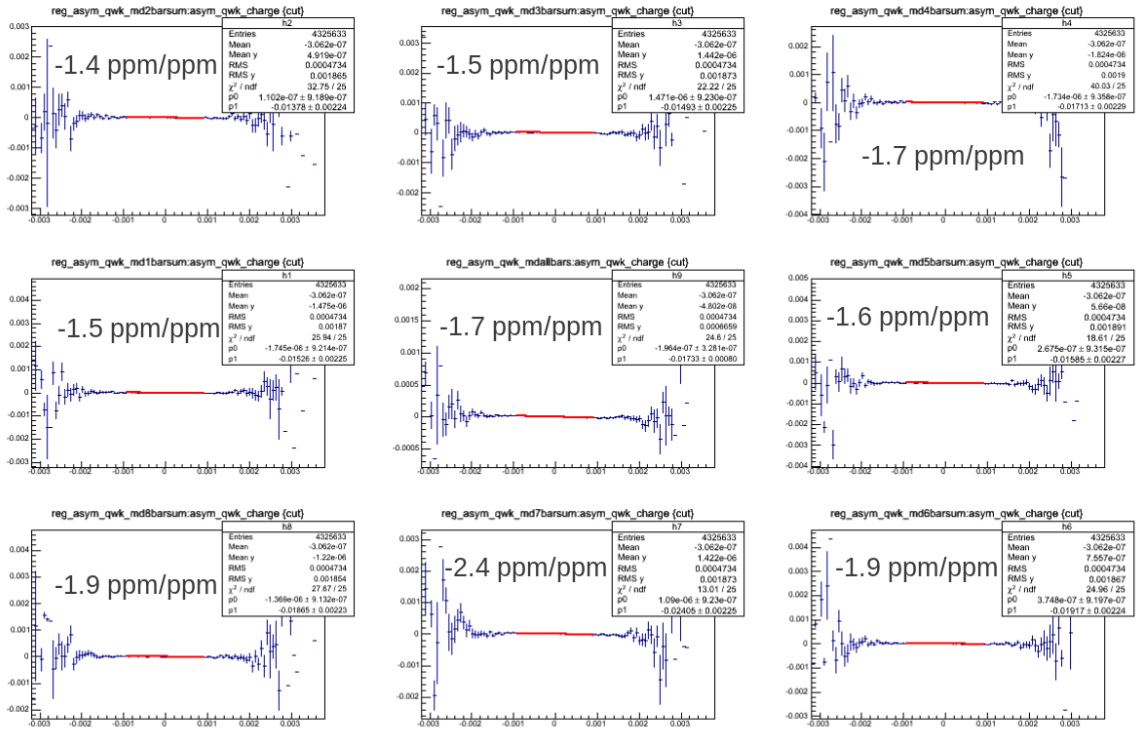

Figure 6.7: *Nonlinearities of the second dataset.*

Next, the consistency of the measured charge asymmetry was examined. The charge asymmetry could be different for different helicity patterns. Allowed helicity patterns are four quartets in a particular order, $(+--+)$ and $(-++-)$, denoted 1 and 0, respectively. The pattern preceding the measured pattern affects the charge asymmetry. In Figure 6.8 one can see the change in measured charge asymmetries given a different preceding helicity pattern. This effect is understood and has been highly suppressed since the HAPPEX II experiment at Jefferson Lab [20].

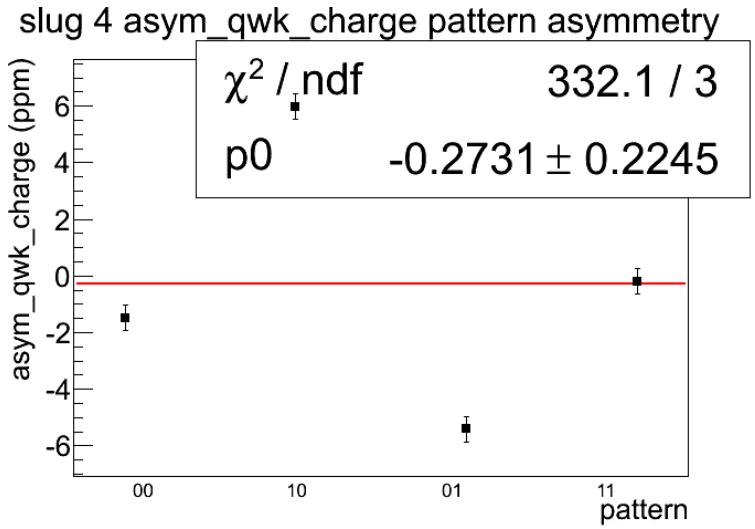

Figure 6.8: *Measured charge asymmetry pattern dependence in second dataset slug IN,R. 00 is the pattern* $(-++-)(-++-)$*, 10 is the pattern* $(+--+)(-++-)$*, 01 is the pattern* $(-++-)(+--+)$*, and 11 is the pattern* $(+--+)(+--+)$*.*

Since the main detector signals are normalized to the beam current any charge variation between quartets is removed to first order. The measured main detector bar asymmetry shown in Figure 6.9 shows no dependence on the charge asymmetry pattern shown in Figure 6.8.

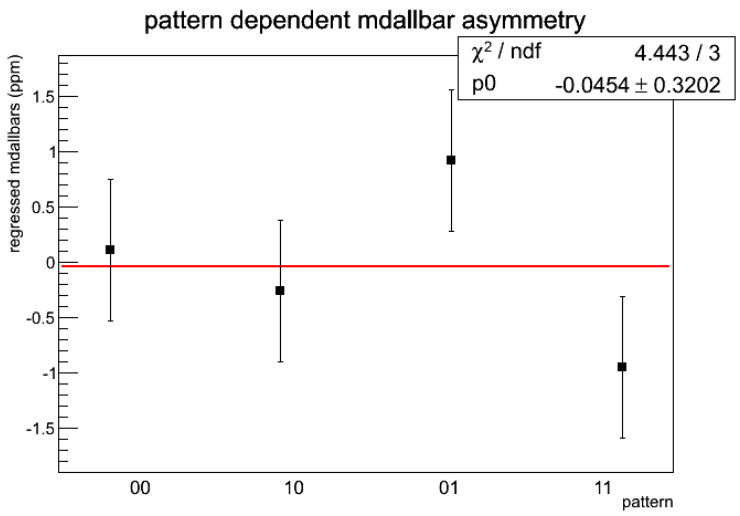

Figure 6.9: *Measured main detector asymmetry pattern dependence in second dataset slug IN,R.*

A battery background detector was implemented to measure electronic false asymmetries for Qweak. It consists of a 6 V battery connected directly to an ADC in the second floor electronics cage.

When the asymmetry of the battery background detector is plotted versus helicity pattern a clear separation between $(+--+)$ and $(-++-)$ can be seen. The first two points in Figure 6.10 are $(-++-)$ with different preceding patterns and the third and fourth points are $(+--+)$ with different preceding patterns. There is some leakage in the electronics that affects the two patterns differently. This effect is small and is not the cause of the second inelastic dataset's (IN+OUT)/2 $\neq 0$ problem but hints at an electrical isolation issue.

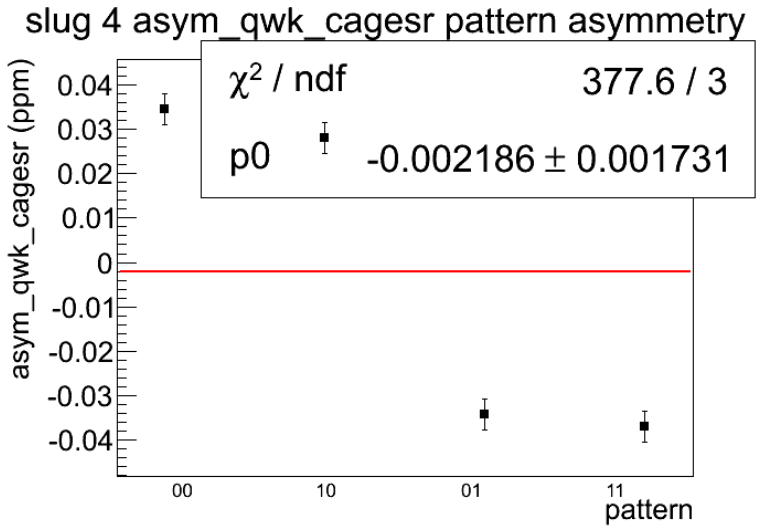

Figure 6.10: *Measured battery asymmetry pattern dependence in second dataset slug IN,R.*

Another electronic isolation issue that was uncovered during the (IN+OUT)/2 $\neq$ 0 investigation was the battery background detector asymmetry correlation to the measured charge asymmetry in Figure 6.11.

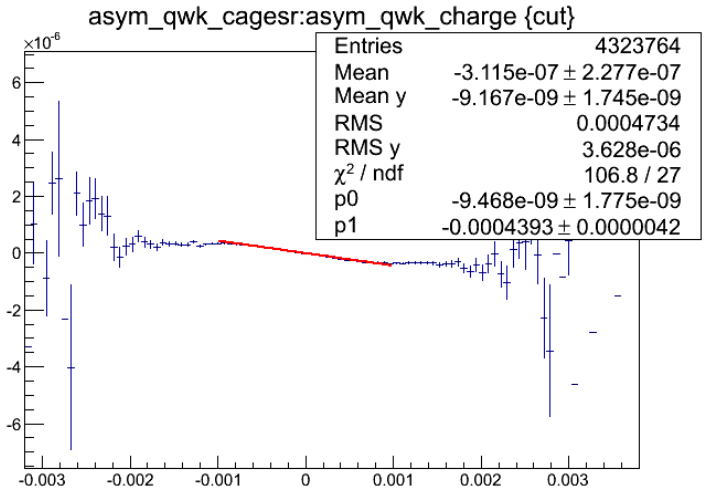

Figure 6.11: *Measured battery asymmetry correlation with charge asymmetry.*

This battery should have no correlation to the measured charge asymmetry. A correlation

is present and electronic cross-talk is the likely cause. The correlation (p1 term in Figure 6.11) is relatively small, but is 100 σ from zero.

Background detectors sensitive to the scattered beam in the experimental hall measured relatively large asymmetries during the second inelastic dataset. With a beamline background dilution of ∼2% this could have been the cause of the (IN+OUT)/2 = 0 check failure.

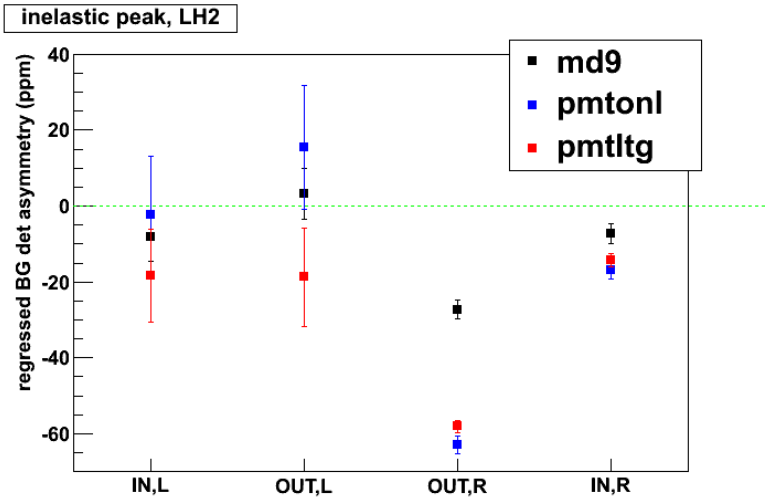

Figure 6.12: *Background detectors for the first and second datasets. md9 is a main detector bar, pmtonl is a main detector PMT, and pmtltg is a main detector PMT coupled to a light guide.*

Figure 6.12 shows the measured asymmetry of some background detectors for the first and second datasets. The IN,L and OUT,L points were part of the first dataset when the *pmtonl* and *pmtltg* background detectors were in a diffuse room background. The OUT,R and IN,R points are from the second dataset when *pmtonl* and *pmtltg* were in the superelastic region (closer to the beamline than the main detectors). This region is a better estimate of the beamline background. If one assumes a ∼2% dilution due to beamline background and a -60 ppm asymmetry the product would be enough to shift the measured asymmetry by

-1.2 ppm.

Another background detector had a nonzero aymmetry during the IN,R slug. This background detector is simply an LED and photomultiplier tube in a light tight box placed near the main detectors in the experimental hall. The measured asymmetry was 0.31 $\pm$ 0.1 ppm and was at least 3 σ nonzero. The signal in this background detector was dominated by the LED, however, approximately 10% of the signal was due to the diffuse room background. This could have caused a $\sim$-3 ppm shift in the measured asymmetry. The nongaussian shape in Figure 6.13 is due to 60 Hz pickup within the detector. The extra noise broadens the width of the distribution but should not affect the mean.

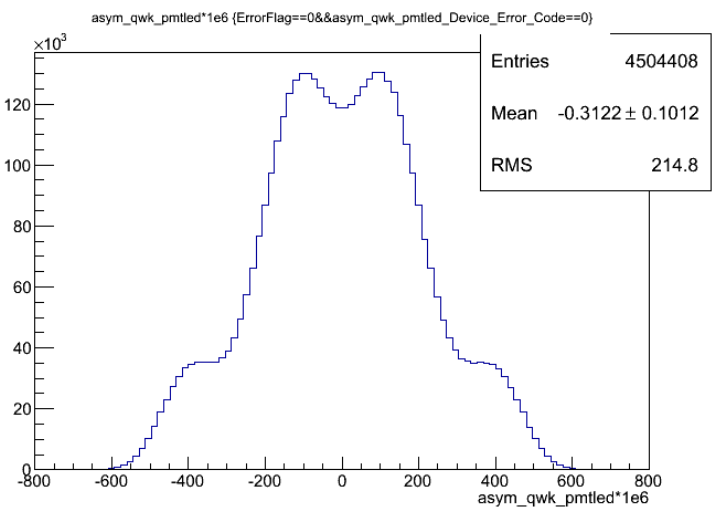

Figure 6.13: *Background detector pmtled in second dataset slug IN,R.*

The measured main detector asymmetry was shifted negative in both IN and OUT half-wave plate states for the second inelastic dataset. The nonzero background detector asymmetries discussed above provide evidence for the $\sim$1 ppm shift in the measured asymmetry. The background detector nonzero asymmetries combined with the potential signal leakage into the main detectors was large enough to explain the (IN+OUT)/2 $\neq$ 0 issue. As a result of

this study, the background detectors were more closely monitored.

6.2.2 Helicity Correlated Pedestal Difference Study

6.2.2.1 Introduction

As a further investigation into the problems of the April 2011 dataset, helicity correlated pedestal differences were investigated. Helicity correlated pedestal differences can cause false asymmetries. A helicity correlated pedestal difference is a detector pedestal that is consistently different between the two helicity states. As mentioned in Chapter 4, a pedestal is the output signal of a detector with *beam off*.

A pair helicity correlated pedestal difference in the main detectors or beam charge monitors of 1 μV and a typical *beam on* signal of 5 V would imply a 100 ppb false asymmetry. Keep in mind the magnitude of the expected measured asymmetry is 230 ppb. The false asymmetry caused by helicity correlated pedestals for pairs is,

$$A_{false} = \frac{\Delta ped}{2 \cdot signal} \ . \tag{6.1}$$

There are several ways helicity correlated pedestal differences could occur. One simple example would be leakage from Pockels cell high voltage. The Pockels cell changes the polarization of the laser light that produces electrons from the photocathode. The Pockels cell voltage flips between ± 4 kV. Electrically isolating the main detectors and beam charge monitors from this voltage switching helps prevent helicity correlated pedestals. This isolation must suppress the ± 4 kV high voltage by eleven orders of magnitude if one wants to constrain the contribution to the measured asymmetry to a few parts per billion.

Pedestal data were taken every day for approximately five minutes during the experiment.

The purpose of these pedestal runs was to minimize nonlinear distortions of asymmetries due to incorrect pedestals in the main detectors in the DC regime. An asymmetry is formed,

$$A_{measured}(+\ -\ -+) = \frac{S_1^+ - S_2^- - S_3^- + S_4^+}{S_1^+ + S_2^- + S_3^- + S_4^+ - 4P}\ , \tag{6.2}$$

where S is the detector signal and P is the detector pedestal.

Using these runs, one can extract the helicity correlated pedestal differences to determine if they were the cause of the problems with the April 2011 inelastic dataset. An analysis of the April 2011 pedestal runs that bracket and include the inelastic dataset will be presented here.

6.2.2.2 Experimental Method

The cross section of a parity-violating (PV) interaction is defined,

$$\sigma = \sigma_0(1 + A\ \cos\theta) \tag{6.3}$$

where σ_0 is the electromagnetic cross section, $\theta_+ = 0°$ and $\theta_- = 180°$ is the polarization of the electron beam in the $+$ and $-$ helicity states, respectively, and A is the parity-violating asymmetry.

Pair and quartet asymmetries are defined to be the same but the numerator is a factor of two different. See Equation 6.4 and 6.5.

$$A_{pair} = \frac{\sigma_+ - \sigma_-}{\sigma_+ + \sigma_-} = \frac{2A\sigma_0}{2\sigma_0} \tag{6.4}$$

$$A_{quartet} = \frac{4A\sigma_0}{4\sigma_0} \tag{6.5}$$

However, the Qweak analyzer reports the *reduced difference* and the *average yield*, so comparing quartets and pairs is straight forward. The *reduced difference* and the *average yield* are,

$$reduced\ difference \propto A\sigma_0 \tag{6.6}$$

$$average\ yield \propto \sigma_0 \tag{6.7}$$

To be sure the analyzer was calculating the correct difference values, the *pair difference* and *reduced difference* reported by the analyzer were compared. According to the numerator in Equation 6.4, the *pair difference* should be exactly twice the *reduced difference*. This is what was observed.

6.2.2.3 Results

One channel from one run was examined a 2 σ nonzero helicity correlated pedestal difference was found. However, there is a 32% chance of selecting a channel that is more than 1 σ from zero in a statistically distributed dataset. The distribution is clearly statistical if one includes all of the channels for all of the runs from April (see Figure 6.14).

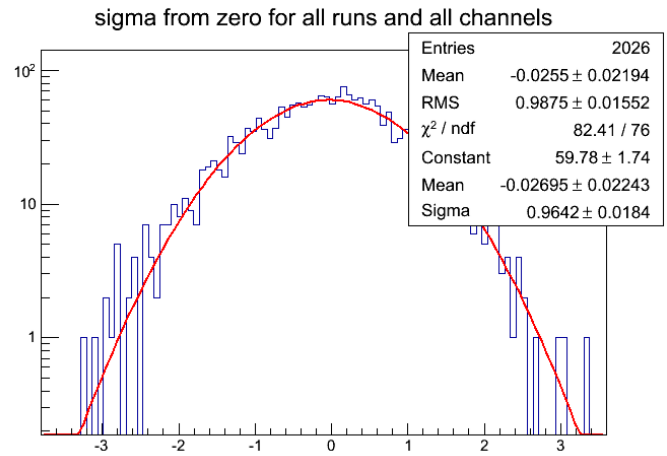

Figure 6.14: *Statistical distribution of mean divided by sigma of all channels of all pedestal runs.*

The main detectors are normalized to the charge monitor so it is important that neither have any evidence of helicity correlated pedestal differences. The charge monitor shows no signs of helicity correlated pedestals. For this dataset the BCM helicity correlated pedestal difference contribution to the measured asymmetry is constrained to be less than 2 ppb at 1 σ confidence.

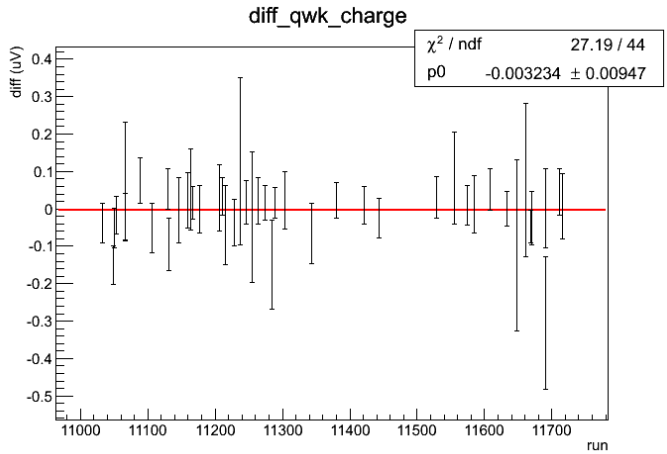

Figure 6.15: *BCM pedestal differences in μV from pedestal runs in April 2011.*

The main detectors show no signs of helicity correlated pedestals. For this dataset the MD helicity correlated pedestal difference contribution to the measured asymmetry is constrained to be less than 4 ppb at 1 σ confidence.

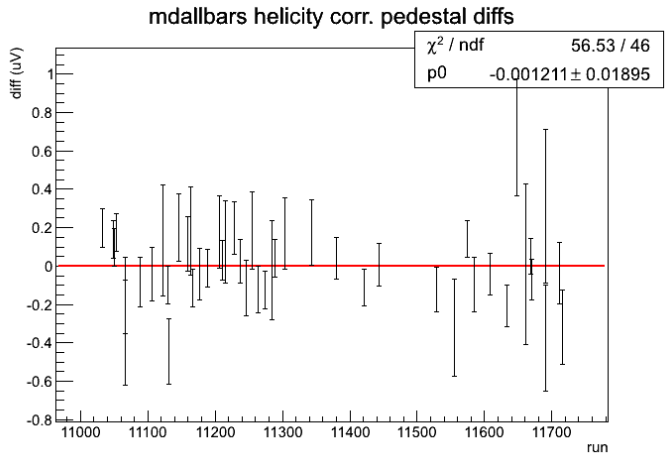

Figure 6.16: *Main detector pedestal differences in μV from pedestal runs in April 2011.*

The width of the main detector pedestal difference determines how long it will take to constrain the helicity correlated pedestal difference contribution to the asymmetry.

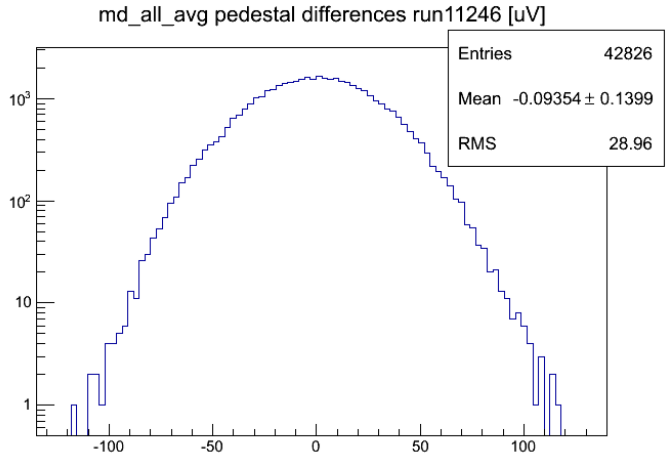

Figure 6.17: *Pedestal value distribution of the unweighted average of all main detector bars.*

Constraining the contribution from helicity correlated pedestals to the measured asymmetry to 2 ppb (0.01 uV) would take 10 hours.

6.2.2.4 Conclusion

While planning this analysis it was discovered that there was some risk of revealing the blinding factor. This risk was eliminated by only considering runs that did not include any beam on the liquid hydrogen target. A comparable analysis of data from the same month could use beam trips. Beam trips occur a few times per hour during normal production running. One would have to be careful to preserve the integrity of the blinding factor in this analysis but comparing the results would be interesting.

The month of April includes the second inelastic dataset, which failed the (IN+OUT)/2 zero check. This study confirms the issues with the second dataset were not caused by helicity correlated pedestals.

The helicity correlated pedestal contribution for the April dataset was constrained to be less than 4 ppb at the 1 σ confidence level.

6.3 Third Inelastic Dataset

Due to the poor quality of the second dataset the collaboration decided to take a third set of data for the inelastic measurement. This was done while the QTOR power supply was misbehaving and was limited to a lower current than necessary for elastic production. A discussion of the better behaved third dataset follows. This dataset will be used to determine the inelastic contribution to the elastic asymmetry and extract the d_Δ parameter.

Table 6.4: The third inelastic dataset helicity correlated beam parameters

	IN	OUT
Helicity Correlated Beam Parameter	Mean	Mean
X position [nm]	-101 ± 6	-65 ± 6
Y position [nm]	-29 ± 2	-29 ± 2
X angle [urad]	$-3{\cdot}10^{-3} \pm 2{\cdot}10^{-4}$	$-2{\cdot}10^{-3} \pm 2{\cdot}10^{-4}$
Y angle [urad]	$-8{\cdot}10^{-4} \pm 1{\cdot}10^{-4}$	$-6{\cdot}10^{-4} \pm 1{\cdot}10^{-4}$
Energy [ppm]	0.01 ± 0.003	-0.01 ± 0.003
Charge [ppm]	-0.59 ± 0.1	0.06 ± 0.1

Table 6.4 shows the quality of the beam parameters for the third inelastic dataset. All values are not consistent with zero, however, the largest nonzero number is a factor of five smaller than the same parameter in the poorly behaved second dataset.

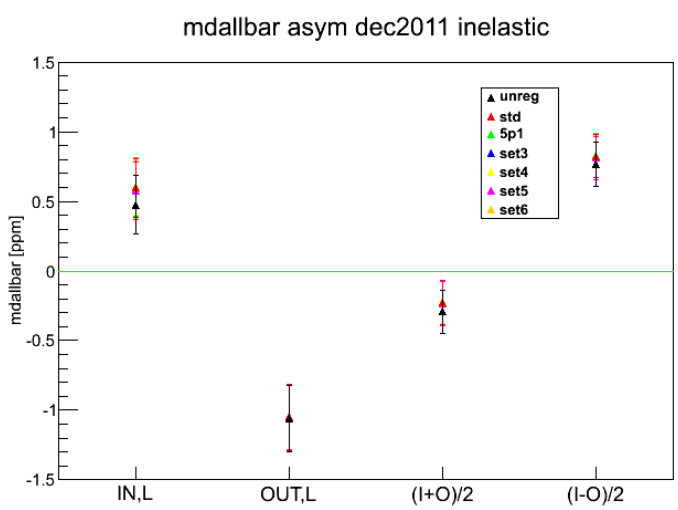

Figure 6.18: *Third inelastic dataset quality.*

Figure 6.18 shows the quality of the measured asymmetry for the third inelastic dataset. The $(IN + OUT)/2$ check is consistent with zero within 1.5 σ. This is a huge improvement

over the 7 σ disagreement of the second dataset.

6.3.1 Q^2

The four momentum transfer for the inelastic measurement is lower than for the elastic measurement. Figure 6.19 shows the simulated Q^2 distribution given a beam energy of 1160 MeV. To determine the inelastic contribution to the main measurement, and to extract d_Δ, this precision will suffice.

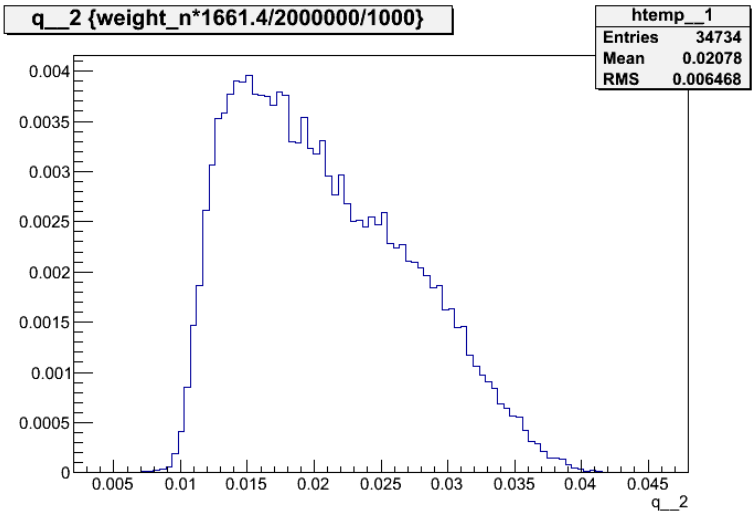

Figure 6.19: *Simulated Q^2 distribution for the inelastic measurement in GeV.*

In Figure 6.20 a simulated distribution of the missing mass, or W, is plotted for inelastic reactions. The distribution is centered on the mass of the delta resonance (1232 MeV).

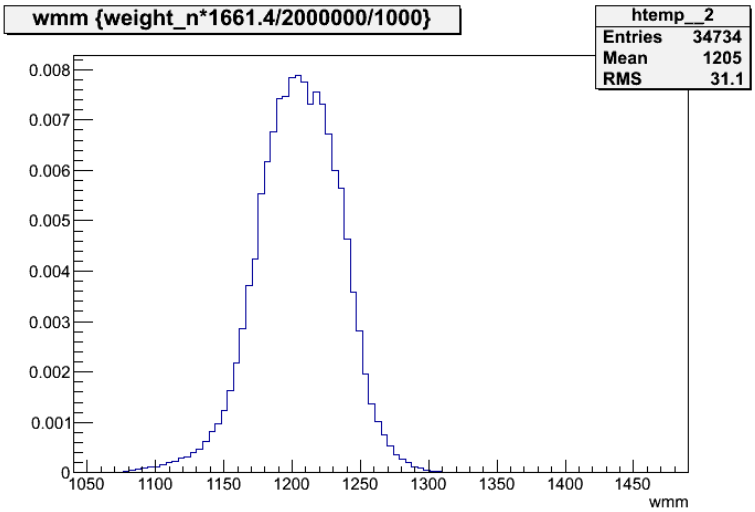

Figure 6.20: *Simulated missing mass, W, distribution at the inelastic QTOR setting in MeV.*

The beam energy measurement on 20 December 2011, just a few days after the third inelastic dataset returned the value $E = 1158.27 \pm 0.1$ MeV. The value of Q^2 used for this analysis is taken from Figure 6.19 and is $Q^2 = 0.02078 \pm 0.0005$ GeV.

6.3.2 Polarization

Both the Møller and Compton polarimeters were operational during the final inelastic running. The measured polarizations agreed and the precision needed for this measurement was achieved. A additional 2% systematic uncertainty has been assigned to both the Compton and Møller measurements for corrections that have not been applied. The final inelastic dataset took place between Compton runs 22936 to 23016 in Figure 6.21. The final values for the polarization are in Table 6.5.

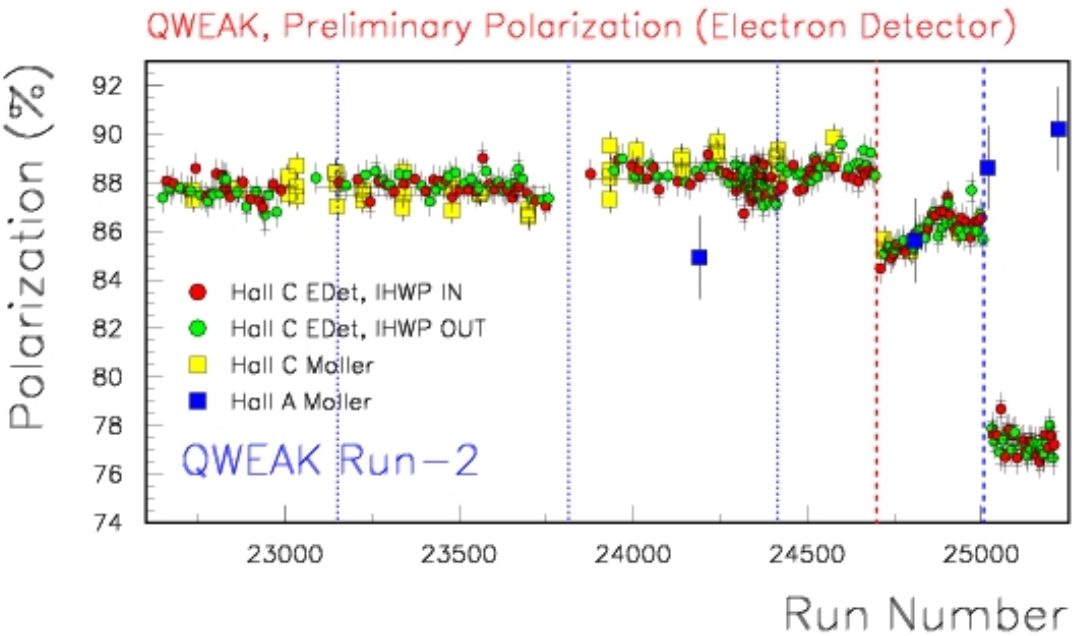

Figure 6.21: *Polarization for the final inelastic measurement.*

Table 6.5: Measured polarization for the final inelastic dataset

Compton	87.627 ± 0.064 stat. ± 2% syst.
Moller	87.799 ± 0.181 stat. ± 2% syst.

6.3.3 Backgrounds

Like the elastic measurement, there are three backgrounds that must be subtracted to extract the inelastic asymmetry. The total signal in the main detectors at the inelastic kinematics is 10% of the total signal at elastic kinematics. However, the beamline background signal is the same at both kinematics so the fraction of the signal at inelastic kinematics due to beamline events is larger by an order of magnitude. At the inelastic kinematics the lower energy elastically scattered electrons dominate the signal. The background contributions

will now be discussed in more detail.

6.3.3.1 Aluminum Background

There is an aluminum contribution because the liquid hydrogen cell is made of aluminum and the upstream and downstream aluminum windows produce ∼4% of the total events in the main detectors. Aluminum dummy targets, created using the same alloy as the target cell, were used to separate the contribution of aluminum from the elastic electron-proton events.

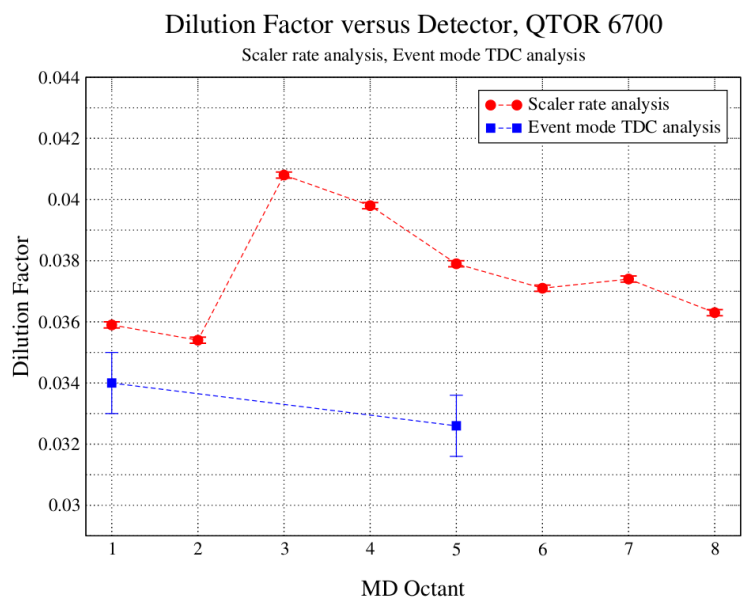

Figure 6.22: *Inelastic aluminum dilution.*

Measurements of the aluminum event fraction at 6700 A are shown in Figure 6.22. The measured dilution factor was found to be $f_{Al} = 0.0376 \pm 0.0036$.

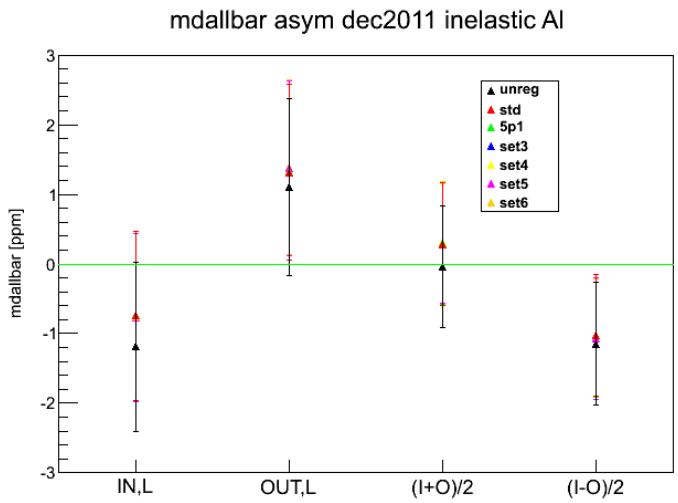

Figure 6.23: *Inelastic aluminum asymmetry.*

The aluminum asymmetry was measured at 6700 A on an aluminum dummy target. The measured value is -1.1 $\pm$ 1 ppm (stat.) and after correcting for the beam polarization $A_{Al} = 1.254 \pm 1.14$ ppm (stat.). More details on the analysis of the aluminum asymmetry and event fraction can be found in Myers's thesis [27].

6.3.3.2 Beamline Background

The beamline background dilution factor for inelastic running is an order of magnitude larger than in the elastic kinematics. This is because the total rate at the inelastic peak drops to 10% of the total rate of the elastic peak, but the number of events originating in the beamline remains constant. More detail about the beamline background is given in Section 5.3.5.

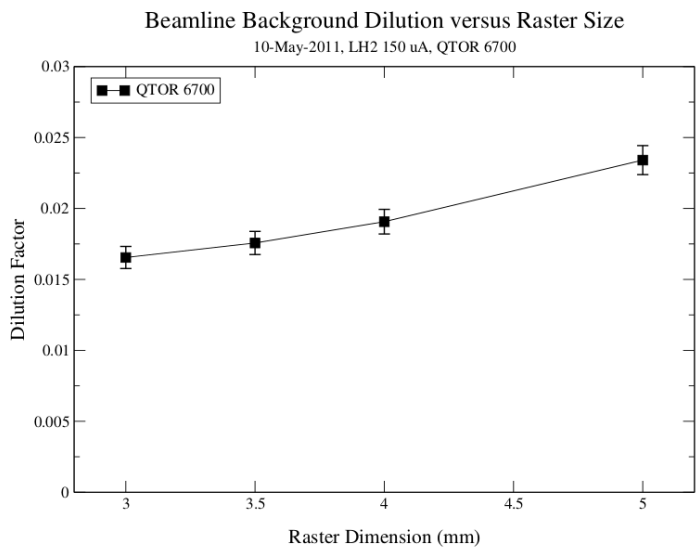

Figure 6.24: *Inelastic beamline dilution.*

Figure 6.24 shows a slight increase in the beamline dilution factor as the raster size increases. A larger raster spreads the incident beam across more of the target and causes more beam to be scattered into the beamline. The raster size used for the inelastic running was 4x4 mm^2 and the final figure used for the beamline dilution is $f_{bl} = 0.0179 \pm 0.0008$.

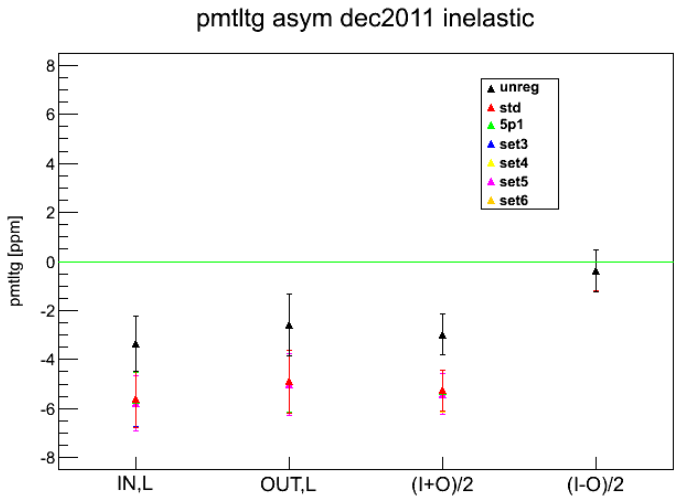

Figure 6.25: *Inelastic beamline asymmetry.*

The asymmetry of the beamline background is shown in Figure 6.25. The *pmtltg* background detector was used for this measurement because it most closely resembles the fully constructed main detector and is in the superelastic scattering region.

Both the IN and OUT states recorded negative asymmetries. This type of false asymmetry cancels in the final asymmetry extraction (IN-OUT)/2, the error weighted average. The beamline asymmetry is not well-known but should be zero. By assigning a large error bar, and a zero asymmetry $A_{bl} = 0 \pm 2$ ppm, any small contributions to the measured asymmetry are accounted for in the uncertainty.

6.3.3.3 Elastic Background

Figure 5.8 shows the fraction of inelastic events at 6700 A is 0.2757 ± 0.0036 (stat. only). The elastic radiative tail background must be what is left after accounting for the other event fractions. This gives the dilution factor value of $f_{ep} = 0.6688 \pm 0.02$ (stat. only). The final uncertainty on the dilution due to the elastic tail background dominates other systematics. More detail is given in Section 6.6.

According to the Standard Model, the elastic asymmetry at QTOR = 8921 A is -230 ppb. However, the inelastic data was taken at a different value of Q^2 so the elastic asymmetry must be corrected. A_{ep} is approximately linear in Q^2 so a simple correction can be applied. The final value of the elastic asymmetry is $Q^2(6700)/Q^2(8921) \cdot A_{ep}(8921) = 0.02078/0.0252 = -190$ ppb.

6.4 Inelastic Electron-Proton Asymmetry

The inelastic measurement includes several components whose contribution must be separated out. Similar to Equation 5.5 for the elastic measurement, Equation 6.8 shows the contributions to the measured asymmetry but for the inelastic measurement at QTOR = 6700 A.

$$A_m = P \cdot \left[\left(1 - \sum f_{bkgd} \right) A_{inel} + f_{Al} A_{Al} + f_{ep} A_{ep} + f_{bl} A_{bl} \right] + A_{false} \ , \tag{6.8}$$

where A_m is the experimentally measured asymmetry, P is the beam polarization, $1 - f_{tot}$ is the fraction of the total rate seen by the main detectors that is inelastically scattered electrons off of protons, A_{inel} is the asymmetry of the inelastically scattered electrons, f_{Al} is the fraction of the total rate seen by the main detectors that is from the target's aluminum windows, A_{Al} is the asymmetry of the electrons that are scattered by the target's aluminum windows, f_{ep} is the fraction of the total rate seen by the main detectors that is from elastic scattering of electrons off of protons, A_{ep} is the asymmetry of the electrons that are elastically scattered from protons, f_{bl} is the fraction of the total rate seen by the main detectors that is from the beamline, A_{bl} is the asymmetry of the electrons originating from the beamline, and A_{false} is the contribution to the measured asymmetry caused by beam parameter correlations with the measured asymmetry.

Table 6.6: Measured asymmetry at QTOR 6700 A

	IN	OUT	(I+O)/2	Av(I,-O)
raw	0.475	-1.061	-0.293	0.733 ± 0.156
std	0.598	-1.052	-0.227	0.798 ± 0.156
5+1	0.603	-1.054	-0.226	0.801 ± 0.156
set3	0.600	-1.054	-0.227	0.800 ± 0.156
set4	0.609	-1.053	-0.222	0.804 ± 0.156
set5	0.575	-1.046	-0.235	0.782 ± 0.155
set6	0.582	-1.048	-0.233	0.787 ± 0.155

Table 6.6 gives the results of the various regression schemes available for the inelastic dataset. For regression scheme definitions see Section 5.3.1.

The sign corrected, error weighted value for the measured asymmetry for 5+1 regression is $A_m = -0.801 \pm 0.156$ ppm (stat. only). This number will be used for this analysis. However, there is an 11 ppb disagreement between regression schemes. This is small compared to the 156 ppb statistical uncertainty but will be accounted for when determining the final uncertainty.

6.4.1 Cut Dependence

The measured asymmetry was sensitive to cuts on beam parameters. The expected shift of the mean of a gaussian distribution by reducing the number of events in the determination of the mean is given in Equation 6.9.

$$\Delta^{pt2pt}_{i\to j} = \sigma_i \left(\frac{1}{\sqrt{N_j}} - \frac{1}{\sqrt{N_i}} \right) , \tag{6.9}$$

where N_i is the number of events before the cut, N_j is the number of events after cuts are made, and σ_i is the width of the distribution of the data before cuts.

In Figures 6.26 and 6.27 cuts were made on the charge asymmetry beam parameter. The mean of the asymmetry moved 10% after a 3 sigma cut was applied to the charge asymmetry distribution for HWP IN. Other beam parameters were also studied but none showed as dramatic of a cut dependence as charge asymmetry. The green lines show the allowed mean shift caused by a loss of events for 5+1 regression governed by Equation 6.9. The black lines show the same for the raw asymmetry. The ∼0.22 ppm statistical error bars of these data points have been omitted for clarity. The shift in asymmetry due to the cuts is acceptable given the statistical uncertainty of this dataset.

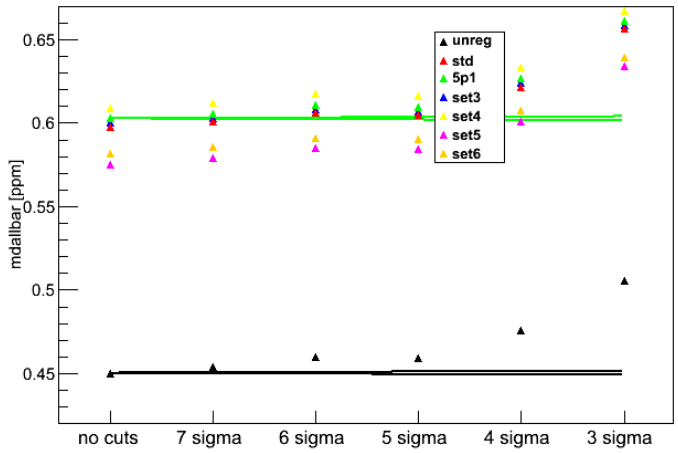

Figure 6.26: *Cut dependence of inelastic dataset HWP IN.*

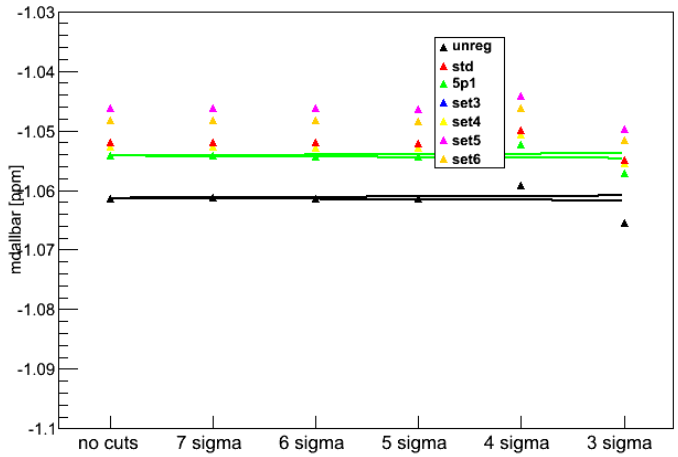

Figure 6.27: *Cut dependence of inelastic dataset HWP OUT.*

One thing to note is the HWP IN data was corrected by regression more than the HWP OUT data. The shift due to cuts on the charge asymmetry are also larger in the HWP IN state.

6.5 Corrections

Using the asymmetry value from 5+1 regression, $A_m = -0.801 \pm 0.156$ ppm (stat. only), one must correct for the contributions defined in Equation 6.8 to extract the inelastic asymmetry. Solving Equation 6.8 for A_{inel} one gets,

$$A_{inel} = \frac{A_m/P - f_{ep}A_{ep} - f_{Al}A_{Al} - f_{bl}A_{bl}}{1 - \sum f_{bkgd}} \ . \tag{6.10}$$

Table 6.7: Contributions to the measured asymmetry.

Background	Dilution Factor	Asymmetry [ppm]	Correction [ppb] ($f_{bkgd}A_{bkgd}$)
Elastic	0.669 ± 0.067	-0.190 ± 0.019	-127
Al	0.0376 ± 0.0036	1.25 ± 1.14	47
Beamline	0.0179 ± 0.0008	0.0 ± 2.0	0.0
TOTAL	0.7243		-80

Table 6.7 contains the background corrections for the inelastic dataset. The total correction due to backgrounds is $\sum f_{bkgd}A_{bkgd} = -80$ ppb. The false asymmetry, $A_{false} = -68$ ppb, was removed during regression. Combining the two correction contributions gives a total correction of -148 ppb.

6.6 Uncertainties

A list of the uncertainties for extracting the inelastic asymmetry is given in Table 6.8. How these uncertainties were calculated is given below.

Table 6.8: Uncertainties of the extracted inelastic asymmetry.

Source	Uncertainty [ppm]
Elastic dilution	0.6876
Statistics	0.6456
Al asymmetry	0.1555
Beamline asymmetry	0.1299
Polarization	0.0794
Blinding	0.068
Al dilution	0.0559
Elastic asymmetry	0.0461
Transverse asymmetry	0.0175
Regression (A_{false})	0.014
Regression variation	0.011
Beamline dilution	0.0088
TOTAL	0.9734

6.6.0.1 Elastic Dilution Uncertainty

The largest uncertainty comes from the simulated elastic dilution factor. Keep in mind there is no way to directly measure this dilution factor.

A simulation of the Qweak experiment was done using Geant3 over a range of QTOR values [41]. This simulation included the lead preradiators placed in front of the main detector bars, light-weighting of each particle that interacts with the main detector, elastic and inelastic $e-p$ events generated in the liquid hydrogen target, and elastic aluminum events generated in the upstream and downstream aluminum windows. The simulation neglects inelastic and

quasi-elastic aluminum events from the target windows, Møller events from $e-e$ scattering, and pion generation. The result of this simulation is given in Figure 6.28.

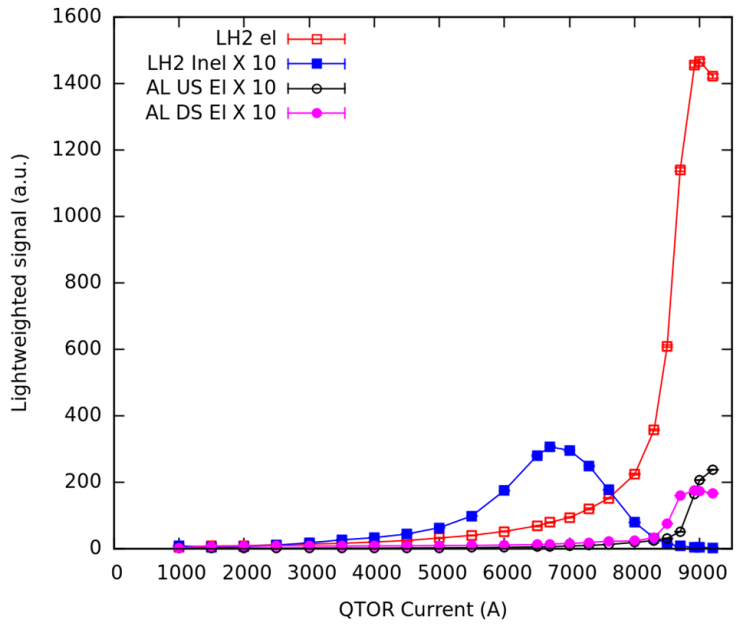

Figure 6.28: *Simulation of contributions from elastic and inelastic $e-p$ and elastic Al from upstream (US) and downstream (DS) target windows. All but elastic $e-p$ events have been multiplied by 10.*

An integration mode QTOR scan was carried out on 11 February 2011. The results were renormalized to agree with the simulation at 8921 A and a comparison is shown in Figures 6.29 and 6.30. The logarithmic scale plot highlights the disagreements.

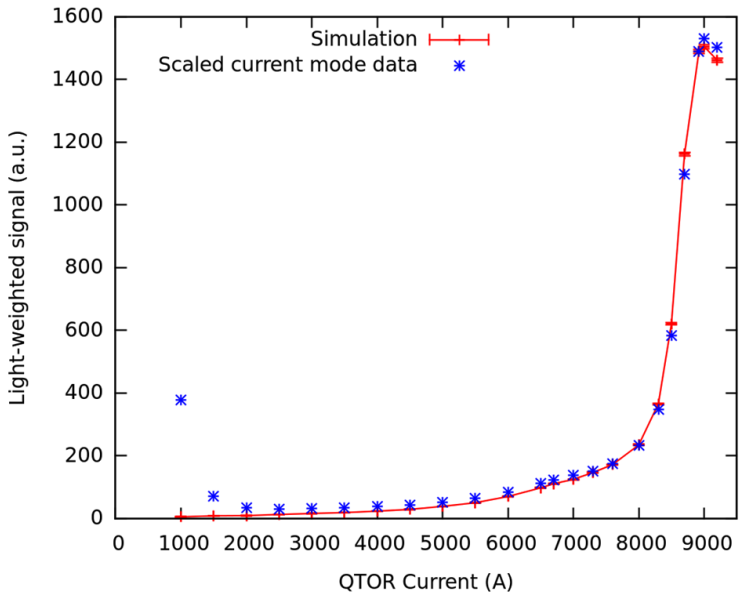

Figure 6.29: *Comparison of data and simulation rate shapes versus QTOR.*

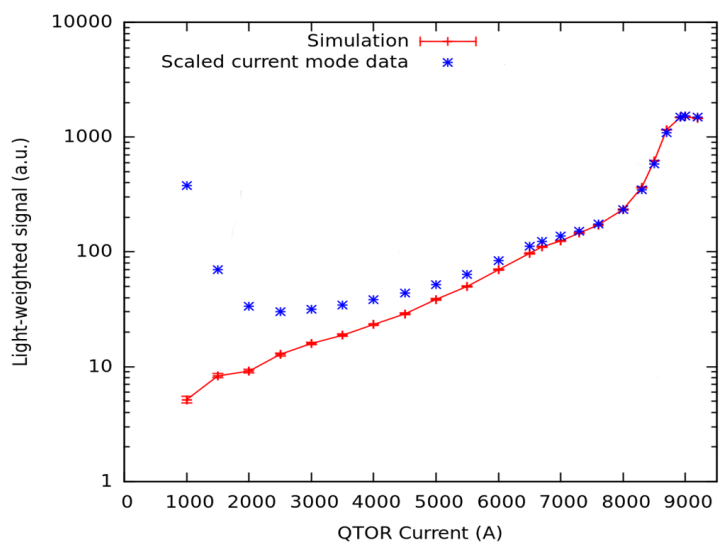

Figure 6.30: *Comparison of data and simulation rate shapes versus QTOR log scale.*

Around QTOR = 4500 A the disagreement between data and simulation is likely because aluminum inelastics and pions were neglected in the simulation. At the QTOR setting of

2000 A the agreement becomes particularly bad because Møller events begin to make it through the apparatus but are ignored in the simulation.

The large uncertainty of the elastic dilution is due to the disagreement between the simulation and data at 6700 A. This is the QTOR value where the inelastic data was taken and according to the residual plot shown in Figure 6.31 the disagreement is 10%.

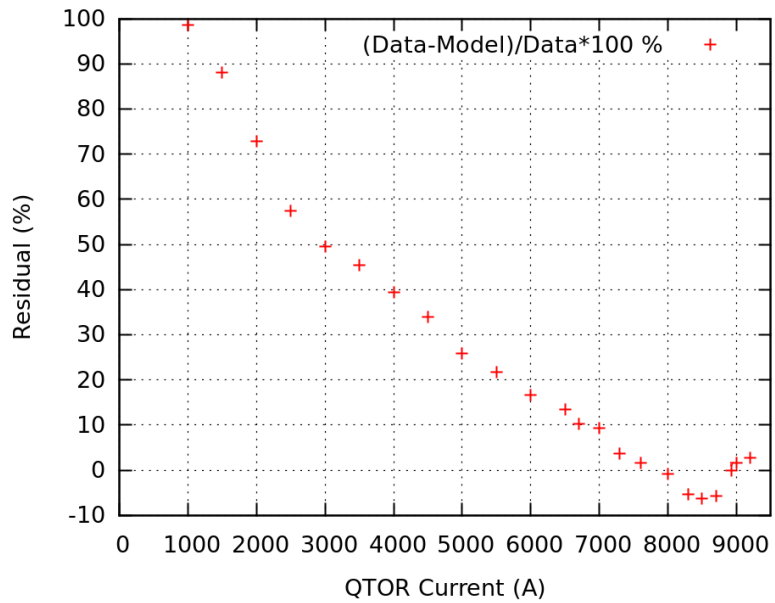

Figure 6.31: *Residuals from a comparison of data and simulation rates versus QTOR.*

The total uncertainty of the elastic dilution must account for that discrepancy. Including this uncertainty in the elastic tail dilution gives the final value, $f_{ep} = 0.668 \pm 0.067$. This uncertainty will likely be reduced as the simulations become more sophisticated.

6.6.0.2 Other Uncertainties

The aluminum and beamline asymmetry uncertainties were discussed earlier and mainly deal with the statistical precision of the measurement. The aluminum and beamline dilutions were

also discussed earlier along with where more detail can be found.

The polarization error is dominated by a 2% systematic uncertainty that will be reduced as more analysis and simulation take place. More detail is given in Section 5.2.

The blinding uncertainty was discussed in Section 5 and is essentially an added source of random noise. The uncertainty was taken to be twice the RMS of a flat distribution with a width of 120 ppb.

A conservative uncertainty for the elastic asymmetry value is presented above. This number was obtained by assigning a 10% uncertainty to the elastic asymmetry. For reference, the goal for the uncertainty on the elastic asymmetry at the end of Qweak data analysis is 2.1%.

The transverse asymmetry is discussed in Section 5.3.2. The inelastic dataset has a larger amplitude than the elastic dataset and the uncertainty is a product of the measured transverse asymmetry amplitude (7 ppm), a very conservative main detector symmetry breaking factor (1/20), and the worst case residual transverse polarization during the inelastic dataset (5%).

The regression uncertainty A_{false} is due to the uncertainties in determining the correlated slopes between the measured asymmetry and the beam parameters and determining the mean of the beam parameters. A conservative approach to determining the mean was used in this case and this uncertainty will likely be smaller for the final measurement.

The variation in the results from regression also contributes to the uncertainty. Table 6.6 shows an 11 ppb disgreement between regression schemes. Since no regression scheme is currently favored over the others this additional uncertainty was included in the final uncertainty of the inelastic asymmetry.

The final inelastic asymmetry is $A_{inel} = -3.03 \pm 0.65 \pm 0.73 \pm 0.07$ ppm (stat., sys., and

blinding).

Chapter 7

Results

7.1 Extraction of d_Δ

The final inelastic asymmetry after all corrections and uncertainties are accounted for is $A_{inel} = -3.03 \pm 0.65 \pm 0.73 \pm 0.07$ ppm (stat., sys., and blinding) at $Q^2 = 0.02078 \pm 0.0005$ GeV^2. Figure 7.1 shows the range of inelastic asymmetries allowed given a range of values for d_Δ as a function of Q^2.

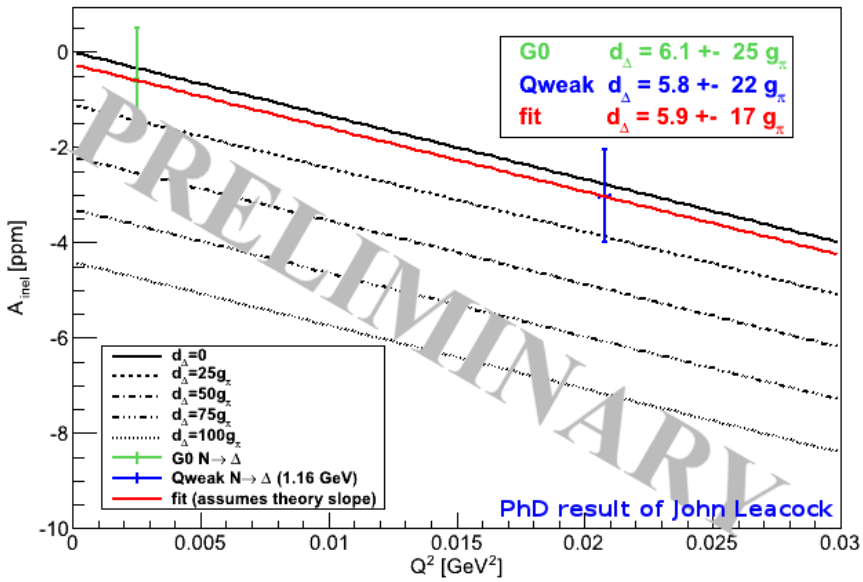

Figure 7.1: *Inelastic asymmetry for different d_Δ values as a function of Q^2 for this analysis and the G0 data point.*

The constraint due solely to this analysis is $d_\Delta = 5.8 \pm 15 \pm 16 \pm 1.5 g_\pi$(stat., sys., and blinding). G0 measured the value of $d_\Delta = 6.1 \pm 25 g_\pi$ at a lower Q^2 and combining the two measurements gives the greater constraint on $d_\Delta = 5.8 \pm 17 g_\pi$ assuming the inelastic asymmetry evolves with Q^2 according to the authors of [51]. This result is preliminary and blinded, and it has not yet gone through the results endorsement process of the Qweak collaboration.

This measurement rules out the largest values of the prediction of the authors of [51] assuming the unknown $\Delta S = 0$ amplitudes will be larger than the known $\Delta S = 1$ amplitudes by $V_{ud}/V_{us} \sim 4.5$. This measurement is still consistent with the prediction of the baryon resonance saturation model including the $1/2^-$ and $3/2^-$ states ($\sim 25 g_\pi$) with no enhancements of the $\Delta S = 0$ amplitudes over the $\Delta S = 1$ amplitudes.

Future work to better determine the value of d_Δ include improving the determination of the electron-proton elastic radiative tail dilution to reduce the systematic error on the extracted value in this thesis and a new measurement of d_Δ at a lower beam energy (877 MeV) also performed during Qweak. These improvements will likely tighten the constraint on d_Δ by a factor of two ($\pm 11 g_\pi$).

7.2 Extraction of Q_W^p

The final elastic asymmetry after all corrections and uncertainties are applied is $A_{ep} = -265 \pm 40 \pm 22 \pm 68$ ppb (stat., sys., and blinding) at $Q^2 = 0.0252 \pm 0.0007$ GeV^2. This number is consistent with Myers's analysis [27]. An updated plot of Figure 2.3 showing the world data for parity-violating electron scattering at low Q^2 and forward scattering angles including the 25% Qweak measurement of this thesis, extrapolated to $Q^2 = 0$ is shown in Figure 7.2.

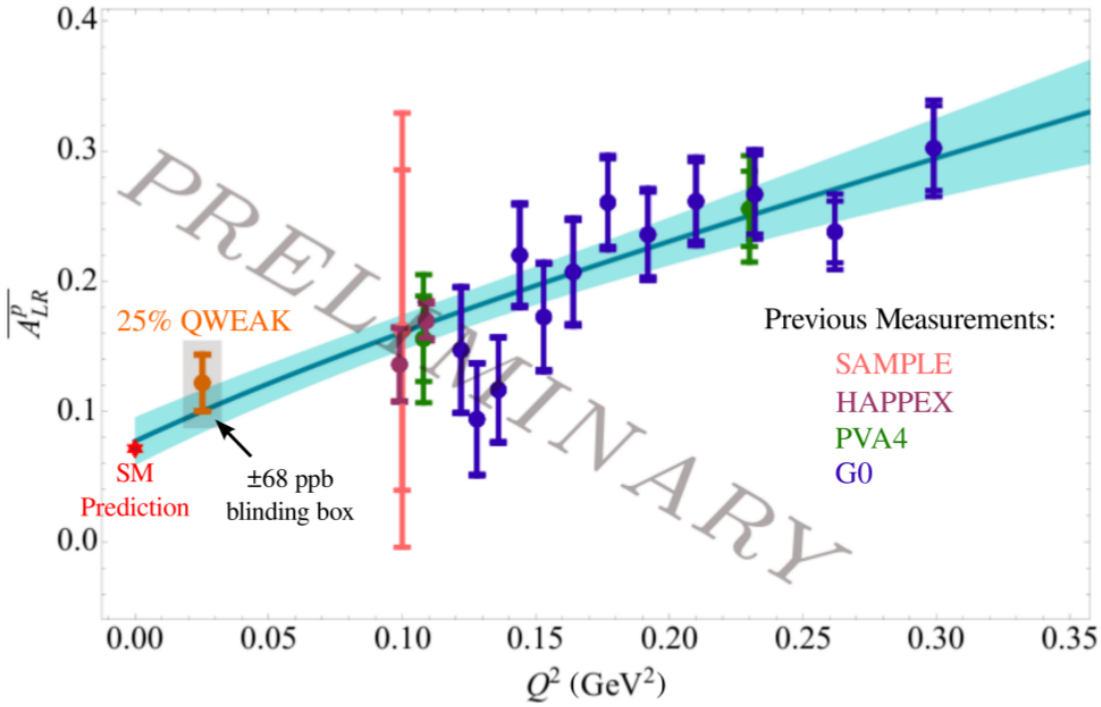

Figure 7.2: *World data on parity-violating electron scattering at low Q^2 and forward scattering angles including the 25% data point from this analysis. This is the same plot as Figure 2.3 but updated to show the results from this analysis.*

The value of the proton's weak charge extrapolated to $Q^2 = 0$ is $Q^p_W = 0.077 \pm 0.019$ (stat. and sys.)± 0.026 (blinding). This does not include the most recent radiative corrections such as the 8% γZ box correction and additional theoretical uncertainties. This value is within 1 σ of the Standard Model prediction of $Q^p_W = 0.0705 \pm 0.0008$ [7].

Because the Qweak measurement is sensitive to $2C_{1u} + C_{1d}$ weak vector quark couplings a better constraint on the isovector quark couplings can be made.

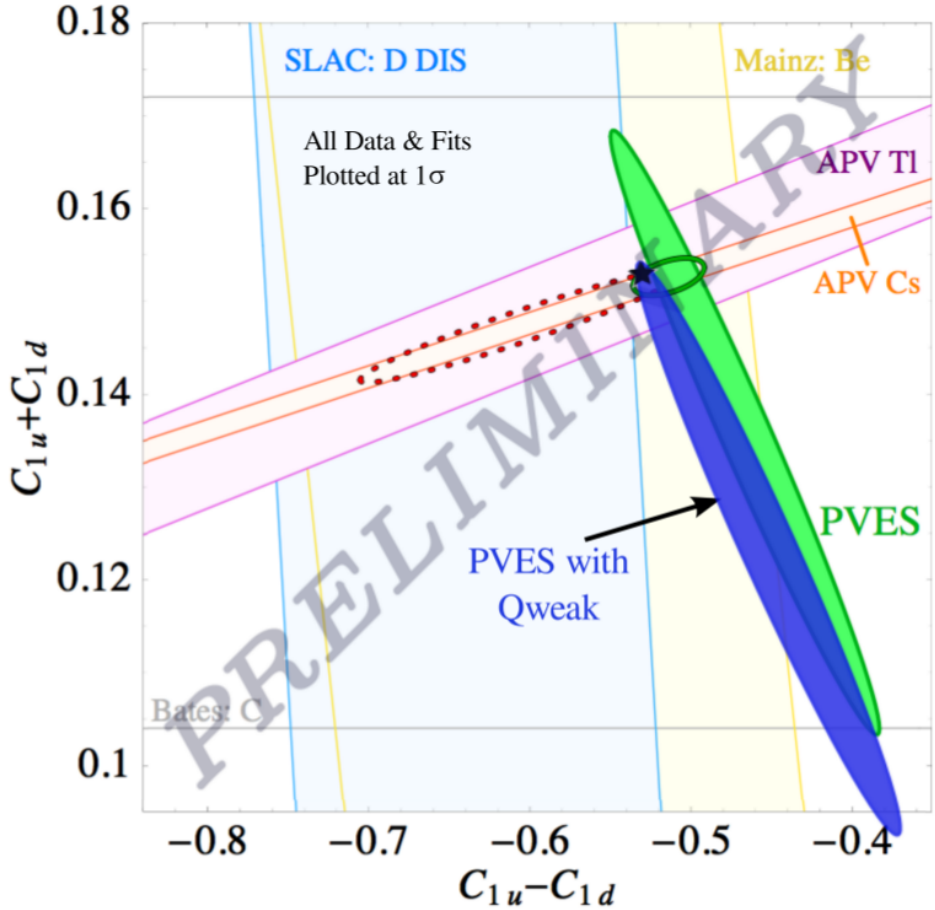

Figure 7.3: *Constraints on the weak vector couplings C_{1u} and C_{1d} including 25% Qweak measurement.*

An updated Figure 2.4 including the 25% Qweak measurement of this thesis is shown in Figure 7.3. Including the Qweak measurement brings the parity-violating electron scattering contribution to the isovector couplings into better agreement with the Standard Model prediction.

The polarization and the Q^2 values used in this analysis are still preliminary, the result is blinded, and the Qweak collaboration has not certified this result. A full statistics analysis and a refined analysis of systematic contributions is currently underway and will result in a

$\sim$4% measurement of the weak charge of the proton.

7.2.1 γZ Radiative Correction

In the notation of the authors of [12] the full Standard Model prediction for the weak charge of the proton is,

$$Q_W^p = [\rho_{NC} + \Delta_e][1 - 4\sin^2\hat{\theta}_W(0) + \Delta_e'] + \Box_{WW} + \Box_{ZZ} + \Box_{\gamma Z} \ , \tag{7.1}$$

where ρ_{NC} renormalizes the neutral to charged current interactions strengths at low energies, Δ_e and Δ_e' are small corrections to the axial vector Zee and γee couplings, respectively, $1 - 4\sin^2\hat{\theta}_W(0)$ is the weak charge of the proton at $Q^2 = 0$, $\Box_{WW}$ is the charged weak loop correction, $\Box_{ZZ}$ is the neutral weak loop correction, and $\Box_{\gamma Z}$ is the γZ box loop correction.

Recently, theorists [39][37][13] have recalculated the γZ box radiative correction and found it to be much larger than originally thought [12]. This value contributes directly to the calculation of Q_W^p and the 1% uncertainty adds in quadrature with the final 2% statistical uncertainty.

All three theoretical calculations agree on the size of the correction, but one group quotes an uncertainty of 2.8% which is a factor of two bigger than the other groups ($\sim$1.3%) and would dominate the 2% expected statistical precision.

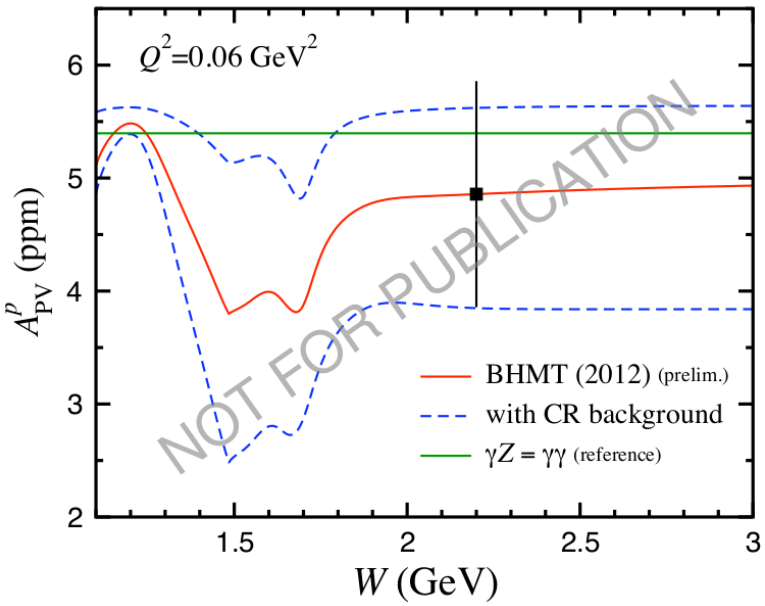

Figure 7.4: *Theoretical prediction of γZ box contribution to Qweak. The red line is the theory prediction and the blue lines are the uncertainties associated with the correction.*

To help constrain the uncertainty of this correction, data was taken with the Qweak apparatus during a higher energy running period. Figure 7.4 shows the anticipated uncertainty of the higher energy Qweak measurement centered on the 1.3% uncertainty theory curve.

QCD uncertainties in radiative corrections must be under control for a precise Standard Model test. Unlike the purely weak WW and ZZ loop corrections, the γZ correction must be treated non-pertubatively due to the γ being massless. This makes predictions of the γZ box contribution difficult.

7.3 Comments on Main Detector Weighting

Recent analysis efforts on the 25% dataset have uncovered a issue with how the main detector bars are weighted before the asymmetry is calculated. Correcting this error in the analysis

has improved the (IN+OUT)/2=0 check. Similar corrections need to be applied to the inelastic analysis.

Appendix A

Notes from Pedestal Difference Analysis

These are the notes from the helicity correlated pedestal differences study described in Section 6.2.2.

List of detectors included in this analysis: mdallbars, md1neg, md2neg, md3neg, md4neg, md5neg, md6neg, md7neg, md8neg, md1pos, md2pos, md3pos, md4pos, md5pos, md6pos, md7pos, md8pos, pmtonl, pmtltg, md9neg, md9pos, pmtled, isourc, preamp, cagesr, dslumi1, dslumi2, dslumi3, dslumi4, dslumi5, dslumi6, dslumi7, dslumi8, uslumi1neg, uslumi1pos, uslumi3neg, uslumi3pos, uslumi5neg, uslumi5pos, uslumi7neg, uslumi7pos, bcm1, bcm2, bcm5, bcm6, charge

List of runs included in this analysis: 11715, 11712, 11691, 11690, 11670, 11668, 11661, 11648, 11633, 11608, 11585, 11574, 11555, 11529, 11444, 11422, 11380, 11343, 11304, 11289, 11285, 11274, 11264, 11255, 11246, 11238, 11229, 11215, 11211, 11206, 11189, 11177, 11166, 11164, 11160, 11146, 11131, 11130, 11123, 11106, 11089, 11067, 11066, 11053, 11050, 11049,

11032

Command to run the analyzer in difference mode: qwparity -r9999 --rootfile-stem diff_nonorm_ --enable-differences 1 --disable-histos 1 --blinder.force-target-out 1 --QwLumi.normalize 0 --QwMainCerenkovDetector.normalize 0

Bibliography

[1] S. L. Adler. Photo-, electro-, and weak single-pion production in the (3,3) resonance region. *Annals of Physics*, 50(2):189 – 311, 1968.

[2] S. L. Adler. Application of current-algebra techniques to soft-pion production by the weak neutral current: V, A case. *Phys. Rev. D*, 12:2644–2665, Nov 1975.

[3] S. Agostinelli, J. Allison, K. Amako, J. Apostolakis, H. Araujo, P. Arce, M. Asai, D. Axen, S. Banerjee, G. Barrand, F. Behner, L. Bellagamba, J. Boudreau, L. Broglia, A. Brunengo, H. Burkhardt, S. Chauvie, J. Chuma, R. Chytracek, G. Cooperman, G. Cosmo, P. Degtyarenko, A. Dell'Acqua, G. Depaola, D. Dietrich, R. Enami, A. Feliciello, C. Ferguson, H. Fesefeldt, G. Folger, F. Foppiano, A. Forti, S. Garelli, S. Giani, R. Giannitrapani, D. Gibin, J. G. Cadenas, I. Gonzlez, G. G. Abril, G. Greeniaus, W. Greiner, V. Grichine, A. Grossheim, S. Guatelli, P. Gumplinger, R. Hamatsu, K. Hashimoto, H. Hasui, A. Heikkinen, A. Howard, V. Ivanchenko, A. Johnson, F. Jones, J. Kallenbach, N. Kanaya, M. Kawabata, Y. Kawabata, M. Kawaguti, S. Kelner, P. Kent, A. Kimura, T. Kodama, R. Kokoulin, M. Kossov, H. Kurashige, E. Lamanna, T. Lampn, V. Lara, V. Lefebure, F. Lei, M. Liendl, W. Lockman, F. Longo, S. Magni, M. Maire, E. Medernach, K. Minamimoto, P. M. de Freitas, Y. Morita, K. Murakami, M. Nagamatu, R. Nartallo, P. Nieminen, T. Nishimura, K. Ohtsubo, M. Okamura, S. O'Neale, Y. Oohata, K. Paech, J. Perl, A. Pfeiffer, M. Pia, F. Ranjard, A. Rybin,

S. Sadilov, E. D. Salvo, G. Santin, T. Sasaki, N. Savvas, Y. Sawada, S. Scherer, S. Sei, V. Sirotenko, D. Smith, N. Starkov, H. Stoecker, J. Sulkimo, M. Takahata, S. Tanaka, E. Tcherniaev, E. S. Tehrani, M. Tropeano, P. Truscott, H. Uno, L. Urban, P. Urban, M. Verderi, A. Walkden, W. Wander, H. Weber, J. Wellisch, T. Wenaus, D. Williams, D. Wright, T. Yamada, H. Yoshida, and D. Zschiesche. Geant4-a simulation toolkit. *Nuclear Instruments and Methods in Physics Research Section A: Accelerators, Spectrometers, Detectors and Associated Equipment*, 506(3):250 – 303, 2003.

[4] Z. Ahmed et al. New precision limit on the strange vector form factors of the proton. *Phys. Rev. Lett.*, 108:102001, 2012.

[5] D. Androic et al. Measurement of the parity-violating asymmetry in inclusive electroproduction of π^- near the Δ^0 resonance. *Phys. Rev. Lett.*, 108:122002, 2012.

[6] J. Beringer, J. F. Arguin, R. M. Barnett, K. Copic, O. Dahl, D. E. Groom, C. J. Lin, J. Lys, H. Murayama, C. G. Wohl, W. M. Yao, P. A. Zyla, C. Amsler, M. Antonelli, D. M. Asner, H. Baer, H. R. Band, T. Basaglia, C. W. Bauer, J. J. Beatty, V. I. Belousov, E. Bergren, G. Bernardi, W. Bertl, S. Bethke, H. Bichsel, O. Biebel, E. Blucher, S. Blusk, G. Brooijmans, O. Buchmueller, R. N. Cahn, M. Carena, A. Ceccucci, D. Chakraborty, M. C. Chen, R. S. Chivukula, G. Cowan, G. D'Ambrosio, T. Damour, D. de Florian, A. de Gouvêa, T. DeGrand, P. de Jong, G. Dissertori, B. Dobrescu, M. Doser, M. Drees, D. A. Edwards, S. Eidelman, J. Erler, V. V. Ezhela, W. Fetscher, B. D. Fields, B. Foster, T. K. Gaisser, L. Garren, H. J. Gerber, G. Gerbier, T. Gherghetta, S. Golwala, M. Goodman, C. Grab, A. V. Gritsan, J. F. Grivaz, M. Grünewald, A. Gurtu, T. Gutsche, H. E. Haber, K. Hagiwara, C. Hagmann, C. Hanhart, S. Hashimoto, K. G. Hayes, M. Heffner, B. Heltsley, J. J. Hernández-Rey, K. Hikasa, A. Höcker, J. Holder, A. Holtkamp, J. Huston, J. D. Jackson, K. F. Johnson, T. Junk, D. Karlen, D. Kirkby, S. R. Klein, E. Klempt, R. V. Kowalewski, F. Krauss, M. Kreps, B. Krusche, Y. V.

Kuyanov, Y. Kwon, O. Lahav, J. Laiho, P. Langacker, A. Liddle, Z. Ligeti, T. M. Liss, L. Littenberg, K. S. Lugovsky, S. B. Lugovsky, T. Mannel, A. V. Manohar, W. J. Marciano, A. D. Martin, A. Masoni, J. Matthews, D. Milstead, R. Miquel, K. Mönig, F. Moortgat, K. Nakamura, M. Narain, P. Nason, S. Navas, M. Neubert, P. Nevski, Y. Nir, K. A. Olive, L. Pape, J. Parsons, C. Patrignani, J. A. Peacock, S. T. Petcov, A. Piepke, A. Pomarol, G. Punzi, A. Quadt, S. Raby, G. Raffelt, B. N. Ratcliff, P. Richardson, S. Roesler, S. Rolli, A. Romaniouk, L. J. Rosenberg, J. L. Rosner, C. T. Sachrajda, Y. Sakai, G. P. Salam, S. Sarkar, F. Sauli, O. Schneider, K. Scholberg, D. Scott, W. G. Seligman, M. H. Shaevitz, S. R. Sharpe, M. Silari, T. Sjöstrand, P. Skands, J. G. Smith, G. F. Smoot, S. Spanier, H. Spieler, A. Stahl, T. Stanev, S. L. Stone, T. Sumiyoshi, M. J. Syphers, F. Takahashi, M. Tanabashi, J. Terning, M. Titov, N. P. Tkachenko, N. A. Törnqvist, D. Tovey, G. Valencia, K. van Bibber, G. Venanzoni, M. G. Vincter, P. Vogel, A. Vogt, W. Walkowiak, C. W. Walter, D. R. Ward, T. Watari, G. Weiglein, E. J. Weinberg, L. R. Wiencke, L. Wolfenstein, J. Womersley, C. L. Woody, R. L. Workman, A. Yamamoto, G. P. Zeller, O. V. Zenin, J. Zhang, R. Y. Zhu, G. Harper, V. S. Lugovsky, and P. Schaffner. Review of particle physics. *Phys. Rev. D*, 86:010001, Jul 2012.

[7] P. G. Blunden, W. Melnitchouk, and A. W. Thomas. New formulation of γz box corrections to the weak charge of the proton. *Phys. Rev. Lett.*, 107:081801, Aug 2011.

[8] B. Borasoy and B. R. Holstein. Role of resonances in nonleptonic hyperon decays. *Phys. Rev. D*, 59:094025, Apr 1999.

[9] C. Capuano. *Parity-violating Asymmetry in the Nucleon to Δ Transition: A Study of Inelastic Electron Scattering in the G^0 Experiment.* PhD thesis, The College of William and Mary, 2011.

[10] B. Desplanques, J. F. Donoghue, and B. R. Holstein. Unified treatment of the parity violating nuclear force. *Annals of Physics*, 124(2):449 – 495, 1980.

[11] S. Ecklund, C. Field, and G. Mazaheri. A fast luminosity monitor system for PEP II. *Nuclear Instruments and Methods in Physics Research Section A: Accelerators, Spectrometers, Detectors and Associated Equipment*, 463(12):68 – 76, 2001.

[12] J. Erler, A. Kurylov, and M. J. Ramsey-Musolf. Weak charge of the proton and new physics. *Phys. Rev. D*, 68:016006, Jul 2003.

[13] M. Gorchtein, C. J. Horowitz, and M. J. Ramsey-Musolf. Model dependence of the γz dispersion correction to the parity-violating asymmetry in elastic *ep* scattering. *Phys. Rev. C*, 84:015502, Jul 2011.

[14] J. Grames, P. Adderley, J. Benesch, J. Clark, J. Hansknecht, R. Kazimi, D. Machie, M. Poelker, M. Stutzman, R. Suleiman, and Y. Zhang. Two Wien filter spin flipper. *Particle Accelerator Conference Proceedings*, page 862, 2011.

[15] F. Halzen and A. D. Martin. *Quarks and Leptons: An Introductory Course in Modern Particle Physics*. John Wiley & Sons Inc., 1984.

[16] Hamamatsu Corporation. R375 photomultiplier tube data sheet.

[17] H. Hammer and D. Drechsel. Parity violating pion electroproduction off the nucleon. *Z. Phys.*, A353:321–331, 1995.

[18] R. Hicks, P. Decowski, C. Arroyo, M. Breuer, J. Celli, E. Chudakov, K. Kumar, M. Olson, G. Peterson, K. Pope, J. Ricci, J. Savage, and P. Souder. Flux profile scanners for scattered high-energy electrons. *Nuclear Instruments and Methods in Physics Research Section A: Accelerators, Spectrometers, Detectors and Associated Equipment*, 553(3):470 – 482, 2005.

[19] J. Jorda, M. Authier, M. Bavlac, E. Burtin, C. Cavata, J. Chen, N. Colombel, P. Deck, A. Delbart, and N. Falletto. A new type of Compton polarimeter for Jefferson Lab Hall A. Technical report, Thomas Jefferson National Accelerator Facility, 1998.

[20] L. Kaufman. *Precision measurement of the proton neutral weak form factors at $Q^2 \sim 0.1\ GeV^2$*. PhD thesis, University of Massachusetts, Amherst, 2007.

[21] J. Leckey. *The First Direct Measurement of the Weak Charge of the Proton*. PhD thesis, The College of William and Mary, 2011.

[22] T. D. Lee and C. N. Yang. Question of parity conservation in weak interactions. *Phys. Rev.*, 104:254–258, Oct 1956.

[23] C. W. Leeman, D. R. Douglas, and G. A. Krafft. The Continuous Electron Beam Accelerator Facility: CEBAF at the Jefferson Laboratory. *Annual Review of Nuclear and Particle Science*, 51:413–450, December 2001.

[24] J. Mammei. *Parity-Violating Elastic Electron Nucleon Scattering: Measurement of the Strange Quark Content of the Nucleon and Towards a Measurement of the Weak Charge of the Proton*. PhD thesis, Virginia Tech, 2010.

[25] A. Manohar and H. Georgi. Chiral quarks and the non-relativistic quark model. *Nuclear Physics B*, 234(1):189 – 212, 1984.

[26] N. C. Mukhopadhyay, M. Ramsey-Musolf, S. J. Pollock, J. Lu, and H.-W. Hammer. Parity-violating excitation of the $\Delta(1232)$: hadron structure and new physics. *Nuclear Physics A*, 633(3):481 – 518, 1998.

[27] K. A. Myers. *The First Determination of the Proton's Weak Charge Through Parity-Violating Asymmetry Measurements in Elastic e+p and e+Al Scattering*. PhD thesis, The George Washington University, 2012.

[28] L. M. Nath, K. Schilcher, and M. Kretzschmar. Parity-violating effects in electroproduction of the $\Delta(1232)$ by polarized electrons. *Phys. Rev. D*, 25:2300–2305, May 1982.

[29] T. Nishitani, T. Nakanishi, M. Yamamoto, S. Okumi, F. Furuta, M. Miyamoto, M. Kuwahara, N. Yamamoto, K. Naniwa, O. Watanabe, Y. Takeda, H. Kobayakawa, Y. Takashima, H. Horinaka, T. Matsuyama, K. Togawa, T. Saka, M. Tawada, T. Omori, Y. Kurihara, M. Yoshioka, K. Kato, and T. Baba. Highly polarized electrons from GaAs–GaAsP and InGaAs–AlGaAs strained-layer superlattice photocathodes. *Journal of Applied Physics*, 97(9):094907, 2005.

[30] J. Pan. Scanner collaboration meeting talk. Qweak-doc-638-v1, 2007.

[31] M. Poelker, P. Adderley, J. Clark, A. Day, J. Grames, J. Hansknecht, P. Hartmann, R. Kazimi, P. Rutt, C. Sinclair, and M. Steigerwald. Polarized source performance and developments at Jefferson Lab. *AIP Conference Proceedings*, 570(1):943–948, 2001.

[32] C. Prescott, W. Atwood, R. Cottrell, H. DeStaebler, E. L. Garwin, A. Gonidec, R. Miller, L. Rochester, T. Sato, D. Sherden, C. Sinclair, S. Stein, R. Taylor, J. Clendenin, V. Hughes, N. Sasao, K. Schler, M. Borghini, K. Lbelsmeyer, and W. Jentschke. Parity non-conservation in inelastic electron scattering. *Physics Letters B*, 77(3):347 – 352, 1978.

[33] C. Prescott, W. Atwood, R. Cottrell, H. DeStaebler, E. L. Garwin, A. Gonidec, R. Miller, L. Rochester, T. Sato, D. Sherden, C. Sinclair, S. Stein, R. Taylor, C. Young, J. Clendenin, V. Hugnes, N. Sasao, K. Schler, M. Borghini, K. Lbelsmeyer, and W. Jentschke. Further measurements of parity non-conservation in inelastic electron scattering. *Physics Letters B*, 84(4):524 – 528, 1979.

[34] Qweak Collaboration. The Qweak experiment: "A search for new physics at the TeV scale via a measurement of the proton's weak charge". Technical report, Thomas Jefferson National Accelerator Facility, 2001.

[35] Qweak Collaboration. The Qweak experiment: "A search for new physics at the TeV scale via a measurement of the proton's weak charge". Technical report, Thomas Jefferson National Accelerator Facility, 2004.

[36] Qweak Collaboration. The Qweak experiment: "A search for new physics at the TeV scale via a measurement of the proton's weak charge". Technical report, Thomas Jefferson National Accelerator Facility, 2007.

[37] B. C. Rislow and C. E. Carlson. Contributions from γz box diagrams to parity violating elastic *e*-*p* scattering. *Phys. Rev. D*, 83:113007, Jun 2011.

[38] P. A. Schreiner and F. V. Hippel. Neutrino production of the $\Delta(1236)$. *Nuclear Physics B*, 58(2):333 – 362, 1973.

[39] A. Sibirtsev, P. G. Blunden, W. Melnitchouk, and A. W. Thomas. γz corrections to forward-angle parity-violating *ep* scattering. *Phys. Rev. D*, 82:013011, Jul 2010.

[40] A. J. F. Siegert. Note on the interaction between nuclei and electromagnetic radiation. *Phys. Rev.*, 52:787–789, Oct 1937.

[41] A. Subedi. QWGEANT 3 simulations of rates & inelastic dilution factor. https://qweak.jlab.org/elog/Analysis+%26+Simulation/451, 2012.

[42] R. Suleiman. personal communication, 2010.

[43] B. Waidywansa. Preliminary beam normal single spin asymmetry results from Qweak. 2012.

[44] P. Wang. Magnetic field simulation and mapping for the Qweak experiment. Master's thesis, University of Manitoba, 2007.

[45] P. Wang. *A Measurement of the Proton's Weak Charge Using An Integration Cerenkov Detector System*. PhD thesis, University of Manitoba, 2011.

[46] S. Weinberg. A model of leptons. *Phys. Rev. Lett.*, 19:1264–1266, 1967.

[47] C. S. Wu, E. Ambler, R. W. Hayward, D. D. Hoppes, and R. P. Hudson. Experimental test of parity conservation in beta decay. *Physical Review*, 105:1413–1415, Feb. 1957.

[48] C. Yan, P. Adderley, D. Barker, J. Beaufait, K. Capek, R. Carlini, J. Dahlberg, E. Feldl, K. Jordan, B. Kross, W. Oren, R. Wojcik, and J. VanDyke. Superharp a wire scanner with absolute position readout for beam energy measurement at CEBAF. *Nuclear Instruments and Methods in Physics Research Section A: Accelerators, Spectrometers, Detectors and Associated Equipment*, 365(23):261 – 267, 1995.

[49] C. Yan, R. D. Carlini, and D. Neuffer. Beam energy measurement using the Hall C beam line. *Proc. Particle Accelerator Conference*, page 2136, 1993.

[50] R. D. Young, R. D. Carlini, A. W. Thomas, and J. Roche. Testing the Standard Model by precision measurement of the weak charges of quarks. *Phys. Rev. Lett.*, 99:122003, Sep 2007.

[51] S.-L. Zhu, C. M. Maekawa, G. Sacco, B. R. Holstein, and M. J. Ramsey-Musolf. Electroweak radiative corrections to parity-violating electroexcitation of the Δ. *Phys. Rev. D*, 65:033001, Dec 2001.

[52] S.-L. Zhu, S. Puglia, B. R. Holstein, and M. J. Ramsey-Musolf. Subleading corrections to parity-violating pion photoproduction. *Phys. Rev. C*, 64:035502, Aug 2001.

[53] S.-L. Zhu, S. J. Puglia, B. R. Holstein, and M. J. Ramsey-Musolf. Nucleon anapole moment and parity-violating ep scattering. *Phys. Rev. D*, 62:033008, Jul 2000.